New techniques and improvements in the MBE growth of Hg-containing narrow gap semiconductors

Dissertation zur Erlangung des naturwissenschaftlichen Doktorgrades der Julius-Maximilians-Universität Würzburg

vorgelegt von

Raimund Schlereth

aus Kitzingen

Würzburg, 2019

Eingereicht am: ____________________
bei der Fakultät für Physik und Astronmie

1. Gutachter: Prof. Dr. Hartmut Buhmann
2. Gutachter: Prof. Dr. Ronny Thomale
3. Gutachter: ____________________
der Dissertation

Vorsitzende(r): ____________________

1. Prüfer: Prof. Dr. Hartmut Buhmann
2. Prüfer: Prof. Dr. Ronny Thomale
3. Prüfer: Prof. Dr. Grzegorz Karczewski
im Promotionskolloquium

Tag des Promotionskolloquiums: ____________________

Doktorurkunde ausgehändigt am: ____________________

Table of contents

1 MBE Material Growth **11**
1.1 MBE laboratory setup . . . 11
1.2 Basic physical processes . . . 13
1.3 Temperature control . . . 15
1.4 Strain in cubic crystals . . . 22

2 Crystal analysis **25**
2.1 Nomarski microscopy . . . 25
2.2 Atomic force microscopy . . . 27
2.3 High resolution X-ray measurements . . . 28
2.4 Reflection high energy electron diffraction . . . 35

3 Electrical transport **39**
3.1 Device design and fabrication . . . 39
3.2 Charge carrier density and mobility . . . 43
3.3 Quantum Hall effect . . . 44
3.4 Chiral anomaly and negative magneto resistance . . . 48

4 The material system $Hg_{1-x}Cd_xTe$ **51**
4.1 Crystal structure . . . 51
4.2 Band structure . . . 52
4.3 Influence of the CdTe substrate . . . 57

5 CdTe virtual substrate **61**
5.1 CdTe on GaAs . . . 62
5.1.1 State-of-the-art . . . 62
5.1.2 GaAs buffer . . . 62
5.1.3 ZnSe buffer, ZnSe/ZnTe superlattice . . . 63
5.1.4 Annealing CdTe . . . 67
5.1.5 CdTe ALE finish . . . 68
5.1.6 Increased CdTe buffer thickness . . . 70
5.2 CdTe on InAs . . . 71
5.2.1 InAs substrate preparation . . . 71
5.2.2 ZnTe buffer on InAs . . . 73
5.2.3 CdTe buffer on InAs . . . 74
5.3 Virtual substrates: transport characterization . . . 76
5.4 Virtual substrates: back gates . . . 80

6 Zero gap $Hg_{1-x}Cd_xTe$ 83
6.1 Sample fabrication 83
6.2 Magneto electrical transport 87
6.2.1 Negative magneto resistance 87
6.2.2 Hall measurements 97

A Virtual substrate: charge carrier density and mobility 107

Bibliography 109

Publications 117

List of abbreviations

QHE	quantum hall effect
QW	quantum well
MBE	molecular beam epitaxy
AFM	atomic force microscopy
HRXRD	high resolution X-ray diffraction
XRR	X-ray reflection
RHEED	reflection High Energy Electron Diffraction
MR	magneto resistance
VS	virtual substrate
x	concentration of cadmium in $Hg_{1-x}Cd_xTe$
CMT-W	cadmium mercury telluride - Window vacuum chamber
XPS	X-ray photoelectron spectrometer
UHV	ultra high vacuum
BET	band edge thermometry
TC	thermocouple
PID	proportional-integral-derivative
a_s	substrate lattice constant
a_l	layer lattice constant
$a_l^{\parallel}$	layer lattice constant in the substrate plane
$a_l^{\perp}$	layer lattice constant out of the substrate plane
f	misfit
ν	Poisson ratio
RMS	root mean square
λ	wavelength
FWHM	full width at half maximum
ω	incident angle
2θ	diffracted angle
FET	field effect transistor

TI	topological insulator
ML	monolayer
n	charge carrier density
μ	charge carrier mobility
2DEG	two-dimensional electron gas
R_{xx}	longitudinal resistance
R_{xy}	transversal resistance
E_{F}	Fermi energy
V_{g}	gate voltage
TG	top gate
BG	back gate
$B, \vec{B}$	magnetic field
$E, \vec{E}$	electric field
SdH	Shubnikov-de Haas oscillations
MEE	migration enhanced epitaxy
ALE	atomic layer epitaxy

Introduction

Solid state physics is one of the major fields in today's physical research. Its contribution to our world ranges from the verification of fundamental physical phenomena, which exceed the field of solid state physics, like the discovery of Majorana fermions [1], to everyday applications. Most significant, the miniaturization of switching electronics due to the invention of solid state transistors has made computers available to everyone and thus changed our lives permanently. Another examples of solid state physics in our daily life is the charge coupled device [2], responsible for the imaging process in a digital camera. Under all materials, which can be assigned to the solid state of matter, crystalline solids are of particular importance as their translation symmetry drastically simplifies the physical treatment of many phenomena and therefore enabling both theoretical prediction as well as experimental observation. Prominent examples of physical discoveries, that started with the successful fabrication of a formerly unavailable material are the physics of the two dimensional material graphene, the discovery of the quantum hall effect (QHE) [3] in field effect transistors (FET) by Klitzing or a new state of matter, in which an insulator is combined with conducting surface states, the so called "topological insulators" (TI), first detected for the two dimensional case in HgTe QW [4] and later in the three dimensional case in BiSb [5].

From an experimental point of view one major challenge is to fabricate specimens of these materials in a high purity to ensure, that the desired physical phenomena are not overshadowed by trivial ones. There are several different commercial techniques available for crystal growth. Their preferred field of application depends on the material composition and the requirements for crystal size and quality. This work revolves around the growth technique of molecular beam epitaxy (MBE), which exhibits a relatively slow growth time but on the other hand excels in the fabrication of high quality crystals. Hereby the focus lies on the growth of mercury telluride (HgTe) and mercury cadmium telluride ($Hg_{1-x}Cd_xTe$) both composed of a 1:1 ratio of elements from the second (Hg,Cd) and sixth (Te) group of the

periodic table of elements (II-VI-materials). These materials exhibit a variety of research applications due to their unorthodox electronic band structure, with the most famous examples being the already mentioned topological insulator state and the quantum spin hall effect.

While for many years MBE is a well established tool for crystal growth of various materials, there are still technological improvements as well as new material combinations pending. This thesis focuses on the implementation of a new method for monitoring the substrate temperature during growth to increase both precision and controllability, which consequently increases the yield of high quality samples and enables new scientific projects, where the substrate temperature is an especially crucial parameter. Furthermore, the growth of virtual substrates (VS) is investigated, which provide a larger surface area resulting in more samples obtainable from one growth cycle and the possibility to use the initial substrate as a backgate. The influence on the band structure of $Hg_{1-x}Cd_xTe$ with changing compositions and the resulting changes in the electronic transport behaviour of this material is also investigated. Here electronic transport measurements are used to observe the characteristic signal of a formerly unavailable topological phase in $Hg_{1-x}Cd_xTe$ layers.

The first three chapters of the present thesis are covering the technologies used and the additions implemented for growth, fabrication and measurements. Chapter four to six show and discuss the main scientific results. Hence, in detail:

- The first chapter of this thesis gives a short overview about the concept of MBE and the setup of the MBE system. A special emphasis lies on the implementation of a band edge thermometry (BET) system for controlling the substrate temperature during growth.

- The second chapter covers the experimental techniques used to analyse the crystallographic properties of the materials grown via MBE. This includes optical microscopy, atomic force microscopy (AFM), high resolution X-ray diffraction (HRXRD) and reflection (XRR) as well as reflection high energy electron diffraction (RHEED).

- In chapter three the setup used for magneto electrical transport measurements is described. Additionally, the theory for the (integer) quantum hall effect and the negative value of the magneto resistance (MR) caused by the

chiral anomaly is discussed, which are important subjects for the interpretation of the data in the following chapters.

- Chapter four takes a detailed look at the material system $Hg_{1-x}Cd_xTe$. A special emphasis lies on the band structure at the critical concentration x_c, which marks the transition point from topological insulator phase to trivial semiconductor phase, where a new topological phase, a Dirac semimetal, arises. Here it is shown that $Hg_{1-x}Cd_xTe$ stands out of the family of Weyl and Dirac semimetals by exhibiting the minimal value of Dirac points with one at the center of the Brillouin zone, without competing effects of surface states in magneto electrical transport.

- The fifth chapter is about Cadmium Telluride virtual substrates (VS). A VS is a layer of material thick enough that all relevant crystal parameters for the overgrowth with a different material come from the VS. Here, different VS layer stacks on top of GaAs:Si and InAs:S substrates are investigated regarding their crystallographic properties.

- Chapter six describes the fabrication of $Hg_{1-x}Cd_xTe$-layers for different compositions around the Dirac semimetallic phase. The negative MR signal in magneto electrical transport measurements and its dependence of the angle between driving current and magnetic field is used as a characterization tool for identifying the Dirac semimetallic phase in these layers. Additionally, the impact of surface states due to the remaining band inversion is discussed.

As main results, the implementation of a BET system improves the reliability of growing high quality $Hg_{1-x}Cd_xTe$ layers significantly. It especially allows a precise control of the composition and thickness of $Hg_{1-x}Cd_xTe$ layers. This made a controlled tuning of the band structure of $Hg_{1-x}Cd_xTe$ around its three different topological phases possible. As a result electronic transport measurements of $Hg_{1-x}Cd_xTe$ dependent on the strength and orientation of an external magnetic field are suggesting a Dirac semimetallic state in this material and in addition show that transport measurements are possible without interference of surface dominated transport, a unique feature of $Hg_{1-x}Cd_xTe$ amongst the family of Dirac semimetals. Finally the investigation of VS structures offers new possibilities in the fabrication of $Hg_{1-x}Cd_xTe$-based devices.

1 MBE Material Growth

Combining different elements in the form of a crystalline structure offers a huge variety of materials with new physical properties in solid states. A well suited technique for the fabrication of such compounds is molecular beam epitaxy (MBE), which is used in the framework of this thesis to grow a variety of II-VI crystalline systems.

Today MBE is a well-established technique that is widely used both in research and industry. As a lot of research on the MBE growth of II-VI crystal systems has already been done, the research focus is leaning more towards the physical properties of the materials. Even though MBE is widely seen as a manufacturing tool for semiconductor devices, there are still a lot of technical enhancements possible to improve MBE growth in terms of quality and reproducibility. An additional method incorporated during this work is a temperature control via a band edge thermometry (BET) system. With this measurement technique the precision of controlling the substrate temperature T increases significantly. Therefore, an overview of the specific MBE setup is followed by a comparison between the established temperature measurement with a thermocouple (TC) and the added BET system, with the focus on consistently producing high quality $Hg_{1-x}Cd_xTe$ layers. The last section of this chapter provides a short overview of the concept of strain and relaxation in cubic crystals, which is important to be considered in the case of combining multiple epilayers with different element compositions.

1.1 MBE laboratory setup

The chair of EPIII is in possession of a large MBE cluster (Figure 1.1), where six single MBE chambers as well as a X-ray photoelectron spectrometer (XPS), a metallization and a sputter deposition chamber are all connected by a transfer system (Modutrack) with a base pressure of approximately 10^{-10} mbar (Ultra High

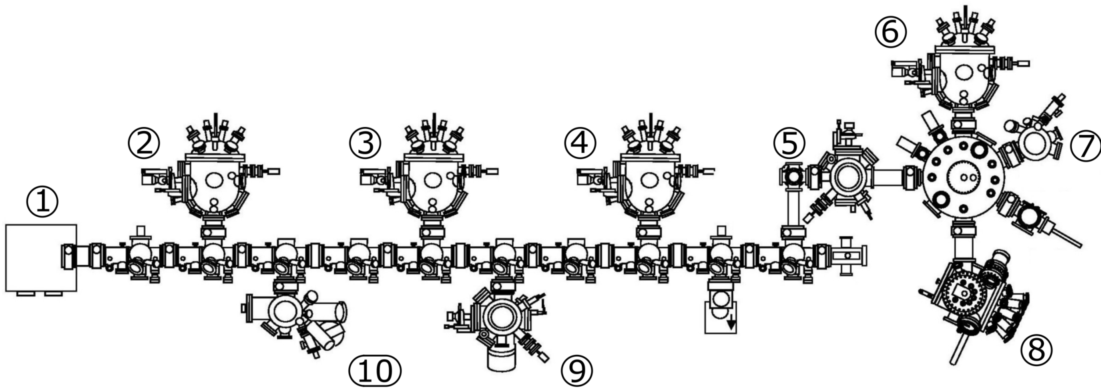

Figure 1.1: MBE cluster at EPIII. 1: Nitrogen glove box with access to the Modutrack. 2: Hg-containing II-VI MBE chamber (CMT-W). 3: Hg free II-VI MBE chamber. 4: III-V MBE chamber (GaAs). 5: Thermal metallization chamber. 6: Second Hg-containing II-VI MBE chamber (CMT-C). 7: Sputter deposition chamber. 8: Pb-containing MBE chamber. 9: Heusler MBE chamber. 10: X-ray photoelectron spectrometer. *Reprinted with permission from Christopher Ames, Molecular Beam Epitaxy of 2D and 3D HgTe, a Topological Insulator. PhD thesis, Julius Maximilians Universität, Würzburg, 2015.* [6]

Vacuum - UHV). This allows in situ transfer of the samples without risking any contamination by air, and combining different materials on one sample, that are not suited for being mounted into one UHV chamber. A more detailed description about all chambers connected to the cluster can be found in [6].

The layout of a Hg-containing MBE chamber and the general technical procedure is described by the example of the CMT-W (for Cadmium Mercury Telluride - Window) chamber (No. 2 in Figure 1.1). Figure 1.2a shows a sectional drawing parallel to the ground and Figure 1.2b a drawing of the backside of the CMT-W chamber. The relevant parts are colorized. Most MBE systems are built in such a way that the cells are mounted at the bottom of the chamber while the substrate is hanging from the top. This is called a vertical design. For the setup of a Hg-containing system however one has to consider that Hg is liquid at room temperature even in UHV and the residual Hg tends to flow to the bottom of the chamber, which can cause Hg contamination of the other materials. Because of that, a horizontal layout was chosen, where the effusion cells are mounted in two horizontal rows at the backside. There are seven hot lip effusion cells and a specially designed Hg cell (cf. Figure 1.2), all pointing towards the central manipulator. The manipulator (number 2 in 1.2a) can be rotated either towards the Modutrack to pick up a substrate holder or towards the growth position facing

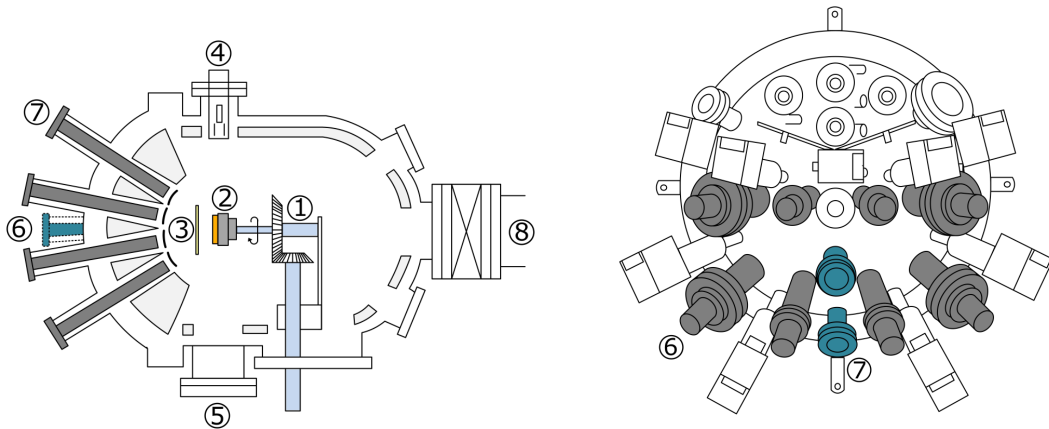

(a) Top view of the CMT-W chamber. (b) Backside view of the CMT-W chamber.

Figure 1.2: a) Top and b) backside view of the CMT-W chamber. 1: Central manipulator with the gear for the sample rotation in blue. 2: Molybdenum sample holder in orange. 3: Cell and substrate shutters. 4: RHEED gun. 5: RHEED screen. 6: Effusion cells. 7: Heated viewports for BET lamp and spectrometer. 8: Main valve for accessing the Modutrack. *Reprinted with permission from Lena Fürst, Konzentrationsabhängiges Wachstum und Charakterisierung von HgCdTe. Master's thesis, Julius Maximilians Universität, Würzburg, 2018.* [7]

the cells. Additionally it allows for a constant rotation of the sample around its surface normal to ensure a homogeneous result over the whole area. A flux gauge mounted on the manipulator allows to measure the particle flux at the growth position. Reflection high energy electron diffraction (RHEED) enables an in situ real time monitoring of the the crystal surface during growth. The substrate is mounted with glue on a molybdenum sample holder that fits to all transfer systems in the MBE cluster. Depending on the maximum temperature during a full growth process either gallium or indium is used as glue (Ga < 400 °C, In > 400 °C).

1.2 Basic physical processes

The basic concept of MBE is to evaporate materials from the effusion cells, which condensates on the substrate to form the layer. Therefore, the physical processes defining MBE growth are occurring on the surface of the substrate from the interaction with the evaporated material, incident on the substrate surface. The following list displays the most important surface processes which strengths depend on the flux ratios of the used materials and the substrate temperature [8]:

- adsorption of the constituent atoms or molecules impinging on the substrate surface.
- surface migration and dissociation of the adsorbed molecules.
- incorporation of the constituent atoms into the crystal lattice of the substrate or the epilayer.
- thermal desorption of the atoms not incorporated into the crystal lattice.

A visualization of these processes is shown in Figure 1.3. For impinging atoms two types of adsorption can be identified. First, if there is no electron transfer between the adsorbate and the adsorbent, so that all attractive forces are van der Waals type, it is called physisorption (physical adsorption). Second, when a chemical reaction takes place between the adsorbate and the adsorbent, the forces are of the type corresponding to the chemical bond. The small adsorption energies for physisorption allow the atoms to move around laterally on the substrate surface before chemisorption adds them to the crystal. Depending on material as well as growth parameters, atoms or molecules either switch sites with atoms which are already incorporated in the crystal (interdiffusion) or accumulate on the substrate surface (nucleation). Depending on how the nucleation occurs three different growth modes are possible, shown in Figure 1.4. If the atoms are more strongly bound to the substrate, it is preferable to attach incoming atoms to crystal sites already present at the surface. This favours the completion of a layer before the growth of the next layer starts, leading to a layer-by-layer growth, also known as Frank-van der Merwe mode (cf. Figure 1.4a). If it is energetically preferable for

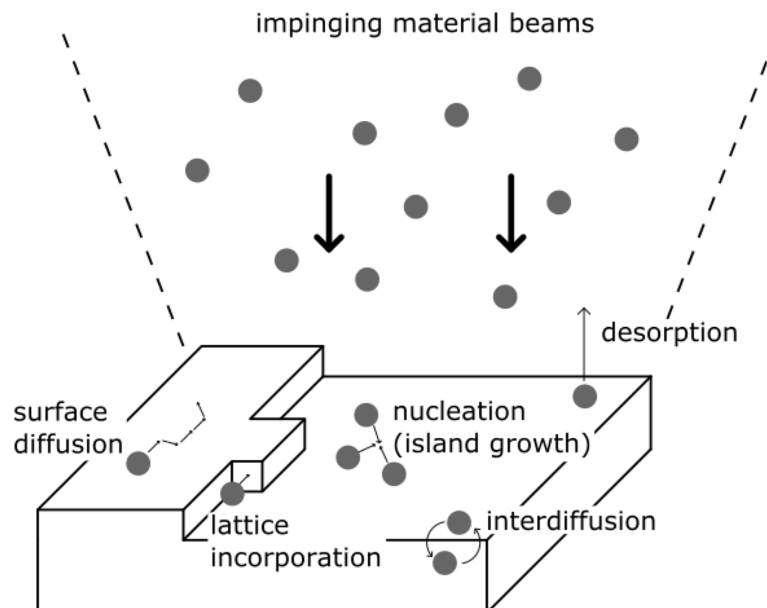

Figure 1.3: Schematic illustration of the surface processes during MBE growth.

the arriving molecules or atoms to be bound to each other rather than to the substrate, islands will get formed (cf. Figure 1.4c), generally referred to as island, or Volmer-Weber mode. A third growth mode results from the mixture of the two upper ones. After forming the first monolayer (ML), or a few ML, subsequent layer growth can get unfavourable and islands are formed on top of this intermediate layer, resulting in the layer plus island, or Stranski-Krastanov, growth mode (cf. Figure 1.4b). Here, chemical and physical properties of the lower crystal, such as surface energies or lattice parameter, play a major role.

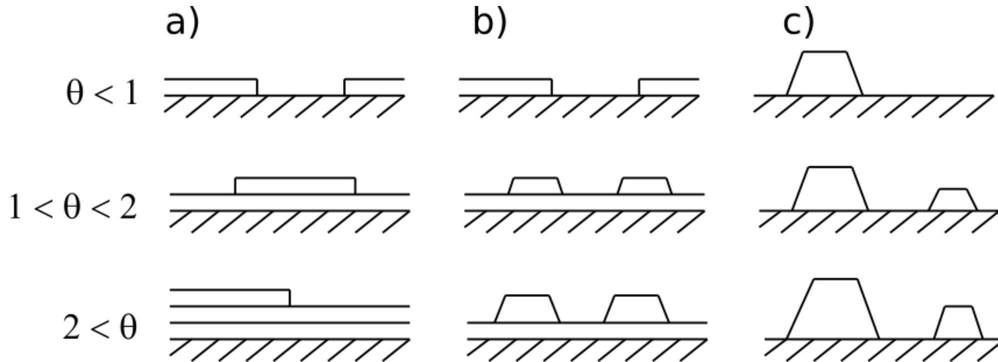

Figure 1.4: Schematic representation of the three crystal growth modes: a) layer or Frank-van der Merwe mode, b) layer plus island or Stranski-Krastanov mode, c) island or Volmer-Weber mode. θ represents the coverage in monolayers, taken from [9]. (*Reprinted from Reports on Progress in Physics **47** 1984, J.A. Venables, Nucleation and Growth of thin films; permission conveyed through Copyright Clearance Center, Inc.*)

1.3 Temperature control

One major part of this work was the implementation and the testing of suitability of a BET system ("BandiT"-system from kspace) for controlling the substrate temperature for HgTe-based MBE growth in the CMT-W chamber (cf. Figure 1.2). To properly discuss the acquired results it is necessary to give an overview of a usual growth cycle before the BET systems was introduced, hence all temperatures mentioned are measured by TC. The growth process can be divided in six steps schematically shown in Figure 1.5. After entering the MBE growth chamber the substrate is heated up (I) and kept under constant Te flux for $T > 250$ °C to avoid thermal defects. Any remaining residuals are removed by thermal treatment at 315 °C (II). At the same temperature there is an approximately 60 nm thick

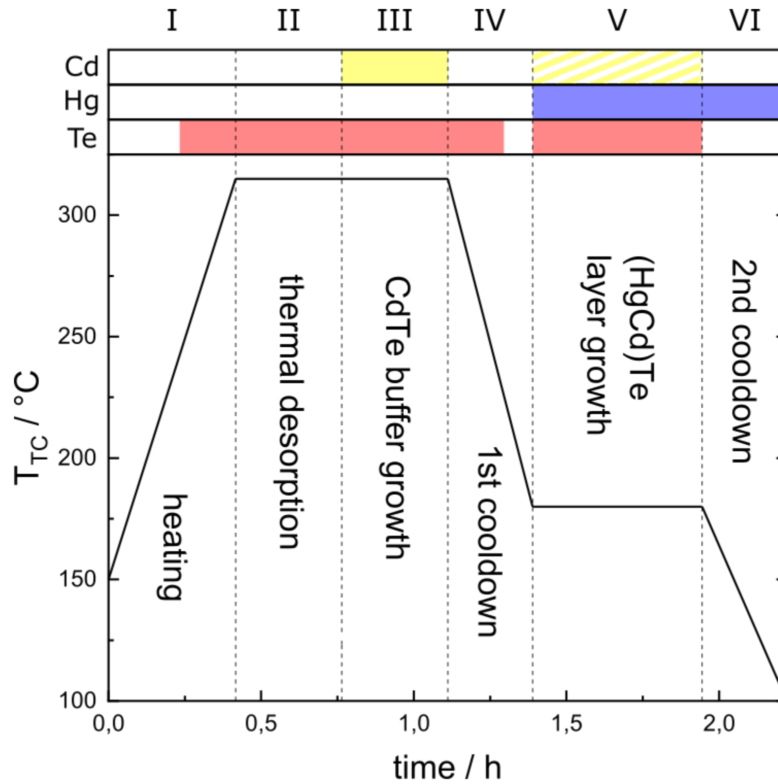

Figure 1.5: Overview of an usual growth cycle for $Hg_{1-x}Cd_xTe$ layers on a CdTe substrate.

CdTe buffer grown from the CdTe compound cell, to provide a clean in situ surface for the Hg-based layer growth (III). Afterwards, the substrate is cooled down (IV) to the growth temperature for the Hg-containing layers. In the following phase (V) the Hg cell stays always open, providing a constant flux of $3.0 \cdot 10^{-4}$ Torr. This does not cause any contamination of the substrate, as almost all Hg is reevaporated at these temperatures. It is furthermore required after the first Hg-containing layer to provide a sufficiently high Hg background pressure to prevent Hg pin holes in the crystal. At the end the sample is cooled down even further until it can be safely taken out from the MBE chamber without risking any thermal desorption of Hg (VI). All cell temperatures and therefore all material fluxes are kept constant during growth. Hence, multiple layer structures are only achieved by opening or closing certain cell shutters.

Finding a suitable technique for measuring the substrate temperature in a Hg-containing MBE process is mainly restricted by the relatively low growth temperature (roughly 180 °C cf. Figure 1.5). This eliminates some common techniques like black body radiation or pyrometry [10]. A well-established technique that has been used for several decades at the MBE cluster at EPIII is to measure the

temperature of a thermocouple T_{TC} pressing against the back of the molybdenum sample holder. However, it appears that this temperature value is not sufficient to represent the actual temperature at the surface of the substrate where layer growth takes place. In fact, there are three inconsistencies in the growth of Hg-containing layers, despite the fact that all growth relevant parameters, namely provided material flux and substrate temperature, are supposed to be constant.

First of all, variations in the quality of the surface morphology were observed. As research on this had already been done, the formation of oval defects due to a incorrect substrate temperature comes to mind [11]. Second, the growth rate of the Hg-containing layers is addressed. When growing $Hg_{0.3}Cd_{0.7}Te$ - HgTe - $Hg_{0.3}Cd_{0.7}Te$ heterostructures, despite identical settings, X-ray diffraction (HRXRD) measurements show, that the layer thickness of the lower $Hg_{0.3}Cd_{0.7}Te$ layer is smaller compared to the upper one. It is widely known that this effect can be decreased by introducing an additional waiting step after the potential growth temperature has been reached and before the start of the Hg-containing layer growth. With this in mind the increase of the growth rate could be explained by a decrease of the substrate temperature over time, although the temperature measured at the backside of the molybdenum block remains constant. Thirdly the composition of $Hg_{1-x}Cd_xTe$ ternary compounds showed significant deviations from sample to sample. This could also be related to an inconsistent substrate temperature, as the sticking coefficients for Cd and Hg react differently to temperature changes.

Because these issues were unsolvable in the current setup a BET system was installed. Applications of a BET system to MBE growth have already been reported for various materials such as GaN on SiC [12] and for the low temperature growth of GaAs [13] and CdTe [14] thin films.

Before the two measurement methods are compared, the basic function of BET is described. The temperature dependence of the band gap value of common semiconductors is well known, for CdTe e.g. refer to [12]. BET uses this temperature dependence by addressing the fact that photons with a energy higher than the band gap value are absorbed, which leads to a sharp edge in the absorption spectrum. Therefore BET requires a substrate with sufficient band gap size (here more than 500 meV) to have the absorption edge in the observable range of the spectrometer. While TC measures the temperature at a reference point close to the sample holder via a mechanical contact, BET measures the mean temperature of the substrate, which is significantly closer to the growth front compared to the

reference point of the TC at the backside of the sample holder. This is the main advantage of BET over TC.

The technical realization of the BET system is sketched in Figure 1.6. A halogen lamp is the light source to illuminate the substrate. For a spectrum suitable for BET the light has to pass at least once through the substrate to interact with the semiconductor band gap. Here, the system is used in a reflective mode (also referred to as front-facing geometry), where the light is diffusively reflected at the unpolished backside of the wafer. This causes the BET spectrum to be influenced by the layers that are grown on top of the substrate. Therefore, dependent on the thickness of the layer in conjunction with its band gap value, a layer with a band gap below the required 500 meV can absorb all incoming light, screening the substrate and making a temperature measurement impossible. Figure 1.7 shows the decrease in spectra intensity with increasing HgTe layer thickness, which has a band gap of 17 meV when grown fully strained on a CdTe substrate [15]. The decrease of spectral intensity of the absorption indicates an upper limit of about 160 nm of HgTe, which is exceeding the typical thickness of HgTe layers used for transport. However growth of HgTe layers exceeding this thickness has shown that it is sufficient to choose the power of the heating filament accordingly to hold the desired constant substrate temperature within the first 160 nm to achieve high quality growth, even when BET cannot measure the temperature over the whole growth cycle.

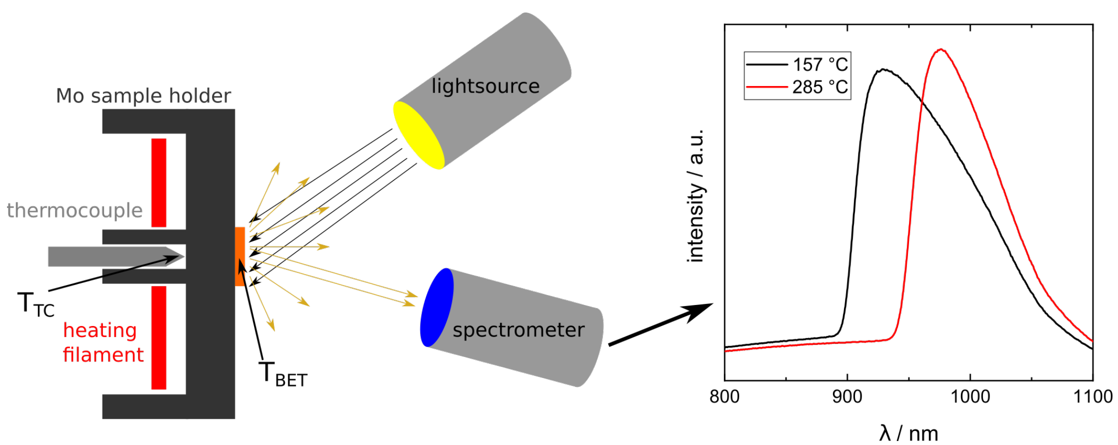

Figure 1.6: Sketch of the BET setup, T_{BET} and T_{TC} indicate the reference point of band edge and thermocouple temperature measurement, respectively. The graph of the absorption spectra on the right shows the change of the band edge position for different temperatures.

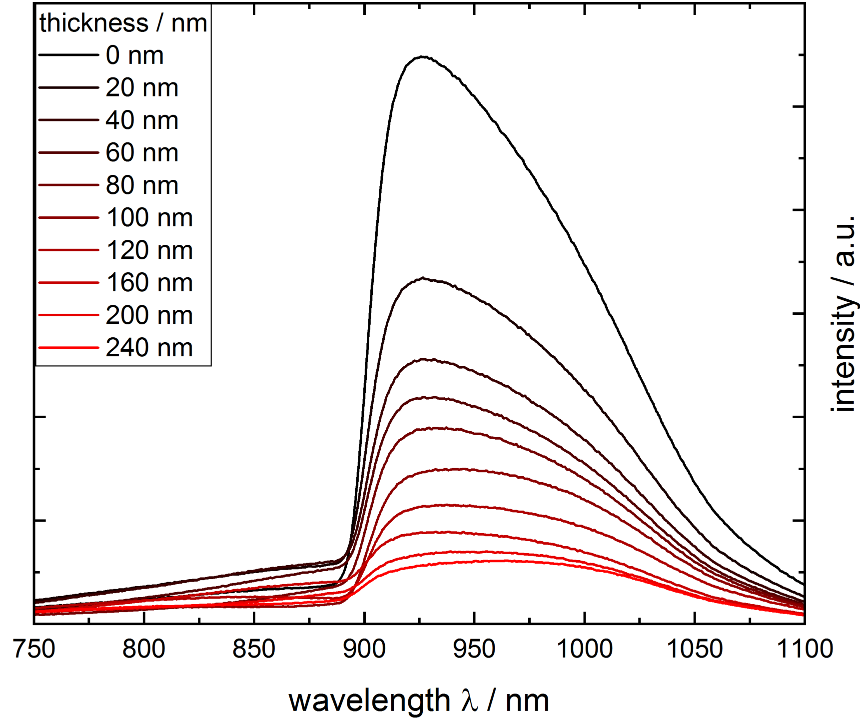

Figure 1.7: BET spectra for different layer thicknesses of HgTe.

To elaborate the differences in measuring the temperature with TC (T_{TC}) and BET (T_{BET}), the temperature during a growth cycle (cf. Figure 1.5) was controlled by the TC while BET is just monitoring and vice versa. As there is no necessity for improving the thermal desorption step or the CdTe buffer, the growth steps I and II are neglected with the focus lying on the differences during the layer growth (V) and the cooldown towards it (IV) (referring to the same steps as in Figure 1.5), as this is the most temperature sensitive procedure. A comparison of the measured temperature values is shown in Figure 1.8, where a) shows a TC-controlled growth cycle, which was the standard procedure so far. In Figure 1.8 b) the substrate temperature is controlled by TC till the end of step III, while the growth of the Hg-containing layer and the cooldown towards it is now controlled by BET.

After the growth of the CdTe buffer (III) the substrate temperature is lowered to $T_{\mathrm{TC}} = 180$ °C (IV) for the subsequent growth of Hg-containing layers (V). By comparing the temperature curves during the cooldown one can see that T_{BET} still decreases significantly while T_{TC} is already stable. This indicates that the temperature at the growth front is still decreasing while it is already stable at the backside of the sample holder. This was already suspected based on the observa-

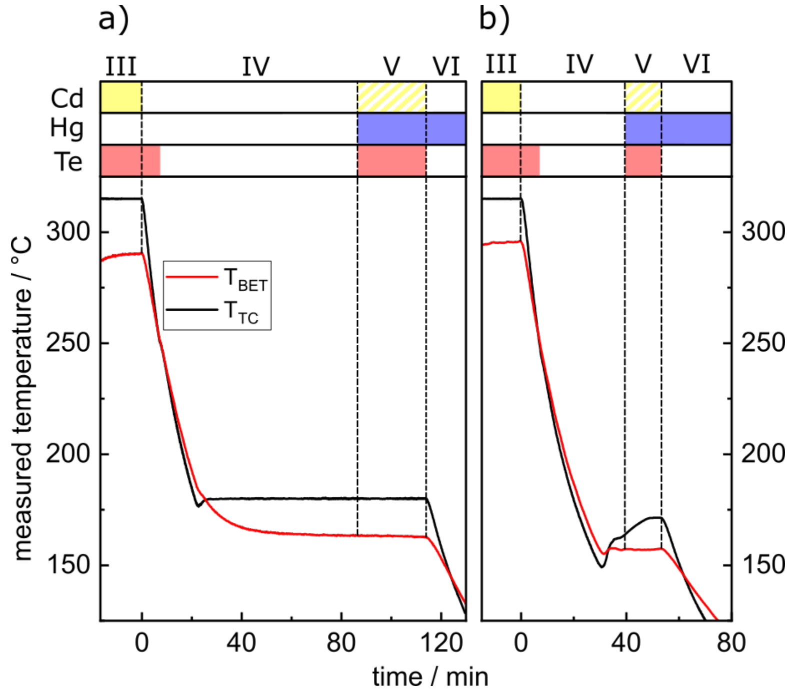

Figure 1.8: Comparison of T_{BET} and T_{TC} during the growth of a $Hg_{1-x}Cd_xTe$ thin film, where the temperature is controlled by a) the TC and b) the BET system.

tion that the growth rate tends to increase over time in multilayer structures as mentioned earlier. Because of that, a waiting time of roughly 30 min between the TC reaching growth temperature and the actual growth is very common to at least lower this effect. However, BET allows to observe that even with a stabilization time of 60 min during step (V) the substrate temperature measured by BET still decreases by about 1 °C throughout the usual growth time for the Hg-containing epilayers.

When BET is used for temperature control as shown in Figure 1.8 (b), a stable T_{BET} for the layer growth can be reached within a much shorter period of time. Having a sample in the chamber at these low temperatures, without a defined growth process taking place, always carries the risk of potential surface contamination. Thus, decreasing this period is always desirable. Additionally, the overall occupation time of the MBE chamber is lowered, reducing also cell material usage. A stable T_{BET} during the layer growth results – as opposed to TC controlled samples – in constant growth rates for multilayer structures. This strengthens the argument that a decreasing temperature during growth caused the increasing growth rate observed in multilayer heterostructures controlled by TC and eliminates this problem.

Furthermore, by comparing growth cycles from multiple samples, variations in the temperature offset between T_{TC} and T_{BET} of ± 5 °C are observed after the temperature stabilized. Apparently the thermal connection between heater and sample holder differs too much over multiple samples to ensure a stable substrate temperature, despite keeping T_{TC} at the same value. This is a possible explanation for the irreproducibility of the desired specifications of $\mathrm{Hg}_{1-x}\mathrm{Cd}_x\mathrm{Te}$ heterostructures, namely thickness, material composition and surface morphology. If the temperature is controlled by BET, however, fluctuations of the layer thickness of HgTe quantum wells are kept at ± 0.1 nm. The material composition of $\mathrm{Hg}_{1-x}\mathrm{Cd}_x\mathrm{Te}$ bulk layers can be controlled with a precision of $x = 0.5$ % (thickness and material composition obtained from HRXRD measurements).

With this in mind a series of samples has been grown, where only T_{BET} was taken into account to control the substrate temperature during the $\mathrm{Hg}_{1-x}\mathrm{Cd}_x\mathrm{Te}$ layer growth. This allows us to measure the size of the growth window for avoiding microvoid defects on the surface of $\mathrm{Hg}_{1-x}\mathrm{Cd}_x\mathrm{Te}$ heterostructure, which are caused by non-optimal substrate temperatures [11]. At $T_{\mathrm{BET}} = 157$ °C pictures taken in the Nomarski mode (for technical details see chapter 2.1) showed the least amount of growth defects (cf. Figure 1.9). By changing the temperature by only 1 °C in either direction, an increase of growth defects could be observed. This depicts a similar growth window for $\mathrm{Hg}_{1-x}\mathrm{Cd}_x\mathrm{Te}$ as reported for another crystal direction in [11], which requires a temperature precision that cannot be provided by a thermocouple in our current growth process.

For further improvements it needs to be mentioned that currently the temperature has to be changed manually by controlling the heater's power supply output.

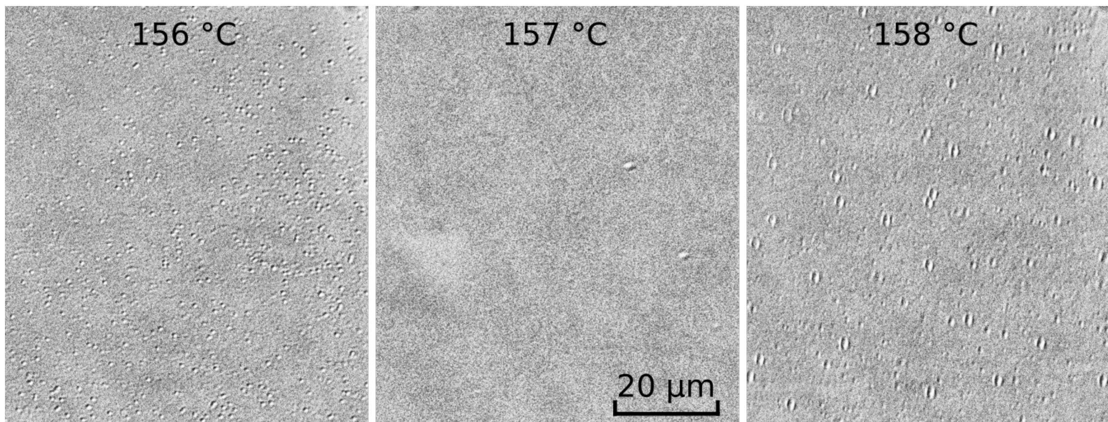

Figure 1.9: Comparison of Nomarski pictures of $\mathrm{Hg}_{1-x}\mathrm{Cd}_x\mathrm{Te}$ layers at different temperature values measured with BET (same scale for all images).

This unfortunately leaves the temperature control open for "human errors". It was possible to control the temperature within ±1 °C around the desired value. An automatic temperature control via a proportional-integral-derivative (PID) controller is currently implemented and expected to improve this even further.

1.4 Strain in cubic crystals

The concept of strain describes the distortion of a crystal's spatial dimensions as a consequence of a pressure-like force applied towards the crystal lattice. Such a force can have various origins, and a detailed analysis can be found in [16]. Here, the discussion will be limited to cubic unit cells and strains perpendicular or parallel to the basis vectors, since this covers all fabricated samples. It is also assumed that the substrate is very thick compared to the overgrown layer, and thus undergoing no change in its parameters due to strain effects.

Following Van der Merwe [17] the misfit f can be obtained from the lattice constants of the substrate a_s and the layer a_l

$$f = \frac{a_l - a_s}{a_l} \tag{1.1}$$

which is isotropic for cubic systems. If the misfit between substrate and layer is sufficiently small, the layer grown on top of the substrate will fully adopt the substrates lattice constant in the surface plane for a finite layer thickness depending on the absolute value of f. For $a_l > a_s \rightarrow f > 0$ the strain is called compressive and for the opposite case ($a_l < a_s \rightarrow f < 0$) its called tensile strain [18]. Such a growth regime, where the in-plane lattice constant of the layer $a_l^{\parallel}$ is always the substrates lattice constant, is referred to as pseudomorphic. According to the Poisson effect compressive strain in the surface plane will lead to a tensile strain out-of-plane and vice versa. The out-of-plane and in-plane lattice constants are connected by the Poisson ratio ν.

$$a_l^{\perp} = a_l + \nu \cdot (a_l - a_s) \tag{1.2}$$

with ν being obtainable from the shear moduli $\nu = 2c_{12}/c_{11}$ of the specific material. With increasing layer thickness it will become energetically favorable for misfit dislocations to be introduced, causing a relaxation of the overgrown layer. Therefore the value of $a_l^{\parallel}$ changes from $a_l^{\parallel} = a_s$ towards $a_l^{\parallel} = a_l^{\perp} = a_l$.

A lot of effort has been put in understanding relaxation mechanisms and quantifying the critical thickness d_c at which relaxation starts for various material systems. Above the critical thickness and for sufficiently low misfit the layer will begin to relax due to the formation of misfit dislocations. This causes a decreasing crystal quality, evidenced by the increasing full width at half maximum in the ω scan of the HRXRD measurements of the epilayer (for HRXRD cf. chapter 2.3). In the case of HgCdTe grown on CdZnTe this is investigated in [19]. For HgTe layers on CdTe substrates experiments have shown a d_c of around 130 nm [20] to 155 nm [6]. For misfits $f > 5\%$ relaxation takes place within the first few nm of the layer, where the above mentioned relaxation characteristics do no longer apply. Instead, relaxation takes place by the formation of pits and islands (Stranski-Krastanov growth mode see sec. 1.2). Table 1.1 shows the lattice constants a of the materials used in the course of this work.

material	a/Å	source
GaAs	5.65325	[21]
InAs	6.0583	[21]
ZnSe	5.6692	[22]
ZnTe	6.009	[12]
CdTe	6.4815	[23]
HgTe	6.4603	[12]

Table 1.1: Cubic lattice constants at room temperature of the used materials.

The lattice constant of any possible mixture of materials a_m like for example the ternary compounds can be calculated depending on the concentration x by using Vegards law [24]

$$a_m = x \cdot a_A + (1 - x) \cdot a_B, \tag{1.3}$$

with a_A and a_B being the lattice constants of the binary materials. By changing the geometrical parameters of a crystal, strain can entail a lot of other changes of the physical properties of solid state materials. In the case of $Hg_{1-x}Cd_xTe$ the most significant aspect is the influence of strain on the electronic band structure, which is discussed in chapter 4.3.

2 Crystal analysis

This chapter deals with the different methods of analysing the MBE-grown layers from a crystallographic point of view. These methods mostly serve as tools for controlling the quality of the grown structures. Nomarski microscopy and atomic force microscopy (AFM) are used for analysing the surface morphology. Layer thickness, crystal quality and material composition can be obtained from high resolution X-ray diffraction (HRXRD) and reflection (XRR). Finally, reflection high energy electron diffraction (RHEED) allows in-situ monitoring of the crystal surface reconstruction.

2.1 Nomarski microscopy

Optical Nomarski microscopy (also known as Differential Interference Contrast) is used to ensure a good surface morphology. Roughness and growth defects become much easier visible by using this illumination technique, compared with a normal optical microscope (cf. Figure 2.1). This makes it a simple to use but powerful tool for ex-situ characterization of the surface morphology of MBE-grown structures. The Nomarski microscope available at EPIII is using a reflective setup. Here the light beam passes a polarizer which provides a defined polarized beam. A Wollaston prism splits the beam into two laterally spaced parts polarized perpendicularly to each other. As these two beams are reflected by the specimen, they experience a possible phase shift caused by differences in height and reflection index of the specimen. The second passing of the Wollaston prism cancels the lateral spacing. A beam splitter guides the beam to the analyzer, which recombines their polarization plane. The interference yields information about the height differences. A commercial digital camera takes a digital picture of the resulting image. The left part of Figure 2.1 shows the difference in visibility of the surface morphology in the Nomarski mode (upper picture) compared with a normal optical microscope

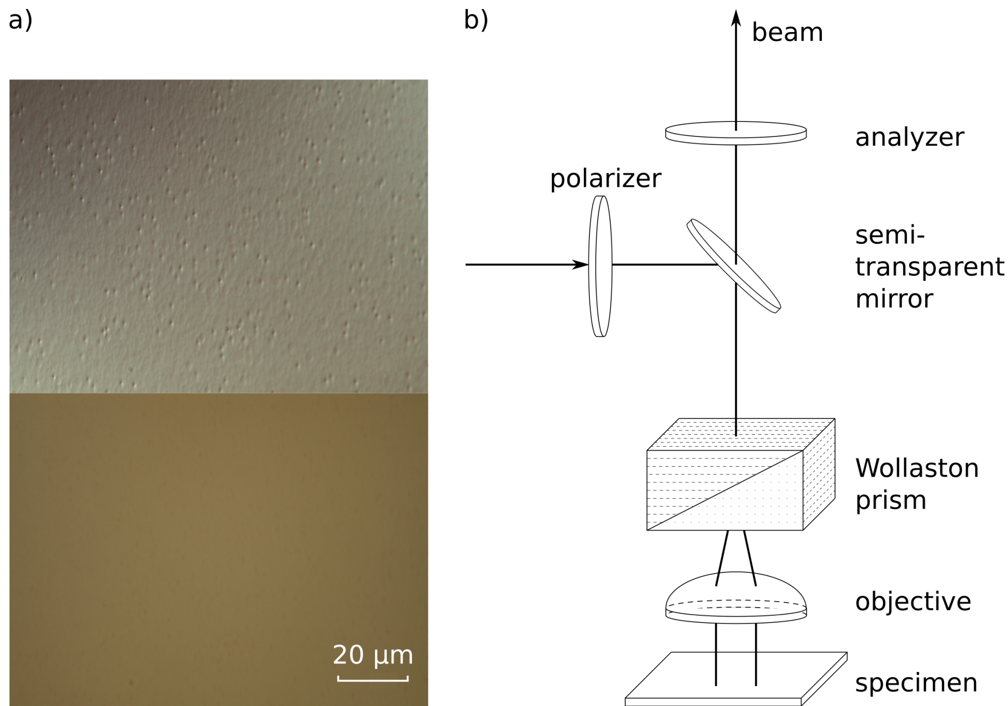

Figure 2.1: a) Comparison of the surface morphology of a specimen with the use of the Nomarski optic (upper picture) and by using an optical microscope (lower picture). For better comparison a sample with many growth defects was chosen. b) Sketch of the layout of a Nomarski microscope, based on [25]. (*Reprinted from Zeiss Information, 70:114-120, 1968, W. Lang, Nomarski differential interference-contrast microscopy; permission conveyed through Zeiss Archive.*)

(lower picture). While the optical microscope suggests a smooth and homogeneous surface, growth defects are only visible in the Nomarski mode.

2.2 Atomic force microscopy

Atomic force microscopy (AFM) is a powerful surface analytical technique, able to generate very high-resolution topographic images of a surface down to atomic resolution in the out-of-plane direction. In the 1980s Binning et al. [26, 27] invented the AFM by combining the principles of the scanning tunneling microscope and the stylus profilometer. A schematic setup of AFM is presented in Figure 2.2. The heart of the AFM is a cantilever with a very sharp tip that is deflected when interacting with the sample surface [28]. In the earlier designs this deflections were measured by observing the tunnel current between a metallic tip and the side of the cantilever that does not face the sample. Today this is done by observing the reflections of a laser beam from the backside of the cantilever, which is easier to implement and requires less maintenance than using a tunnel contact. The detected reflection is further processed by a computer to generate a height profile of the sample. Piezoelectric elements move the cantilever in x-y-direction across the surface. Together with the height profile a three dimensional picture of the sample surface is generated, usually with the z-direction being color coded. The AFM's resolution is limited by the effective curvature of the tip and the step size accuracy of the piezoelectric elements. The setup used in the framework of this thesis has a spatial resolution of around 50 nm. The non-contact mode (AC mode) was chosen as scanning mode, in which the cantilever is oscillating at its resonating frequency. The height profile can be calculated from the change in frequency due to the van der Waals interaction with the sample surface. As this method is mainly used for the characterization of samples surface roughness, the root mean square (RMS) value of a sufficient large area is used for comparing different samples,

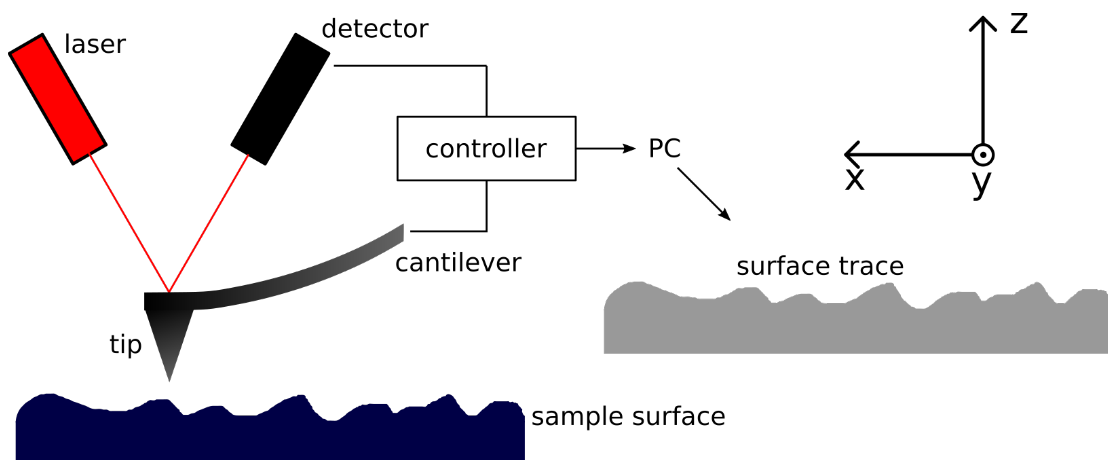

Figure 2.2: Sketch of the AFM setup.

calculated by the following definition:

$$\mathrm{RMS} = \sqrt{\sum_{n=1}^{N} \frac{(Z_n - \bar{Z})^2}{N}} \tag{2.1}$$

n is the number of a specific data point with Z_n being its z-value. $\bar{Z}$ is the average of all z-values. By this definition RMS contains no information on the surroundings of each data point. So this value serves only for comparing, when the samples have similar morphology. In addition, AFM is very susceptible to image artefacts, caused by improper scan parameters which can have a big influence on the value of RMS as well. A proper discussion of AFM image artefacts can be found in [29]. So RMS has to be used very carefully for comparing different samples. All measurements in the framework of this thesis were done with a DME DualScopeTM DS 95-50/200 in combination with the associated software (Dualscope TM / Rasterscope TM SPM Version 2.3.0.6).

2.3 High resolution X-ray measurements

This section provides a short overview of the basic principles of the high resolution X-ray measurement techniques used in the framework of this thesis to examine the MBE-grown layers. A "Bruker D8 Discover" diffractometer was used to perform high resolution X-ray diffraction (HRXRD) and X-ray reflectivity (XRR) for ex-situ characterization of epitaxial layers. Combining these techniques provides detailed information on many crystal properties, such as layer thickness, surface roughness, crystallographic structure, strain, and chemical composition. The two methods rely on different physical principles, hence addressing different properties of the sample but can be used in the same setup shown in Figure 2.3.

The Cu kα_1 line from a Cu-anode X-ray source with a photon wavelength of $\lambda = 1.54056$ Å is used for all experiments. Before the X-ray beam hits the sample the beam is guided through a goebel mirror and a 2-bounce Ge022a monochromator for decreasing the full width at half maximum (FWHM) of the incident beam with a 0.2 mm slit in between for better focus. The sample is mounted on an Eulerian cradle. It can be moved in all three spatial directions (x,y,z) and rotated around these axes (x $\rightarrow \psi$, y $\rightarrow \omega$, z $\rightarrow \phi$). The incident angle, ω, is defined between the X-ray source and the sample. The diffracted angle, 2θ, is defined between the incident beam and detector angle. The reflected respectively

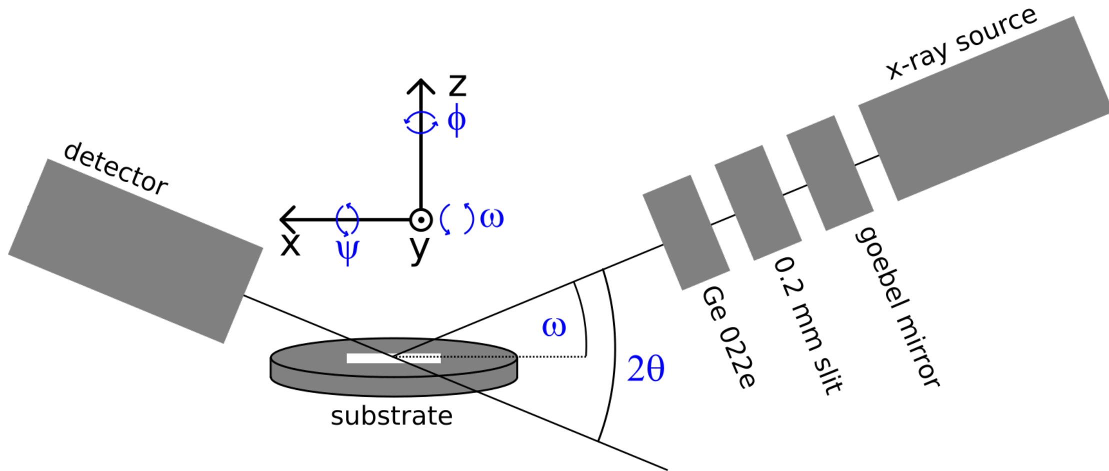

Figure 2.3: Sketch of the measurement setup used in the Bruker D8 diffractometer. The angles ψ, ω and ϕ resemble a rotation around their respective axes.

the diffracted beam can be collected with a scintillation counter or a 1D solid state detector. The second one was especially useful for the recording of reciprocal space maps (RSM), because the measurement time is reduced drastically.

The reflective method (XRR) is only reliant on the reflection at interfaces in the sample and is therefore not sensitive to crystalline properties. Here, the incident X-ray beam hits the sample at a small angle. It is partially reflected from the surface and partially refracted into the material. This process is repeated for every layer interface within the substrate as depicted in Figure 2.4. The multiple reflected waves interfere leading to oscillations in a 2θ - ω scan at small angles, the so called Kiessig fringes [30]. This scan mode moves θ at double the speed of ω, to

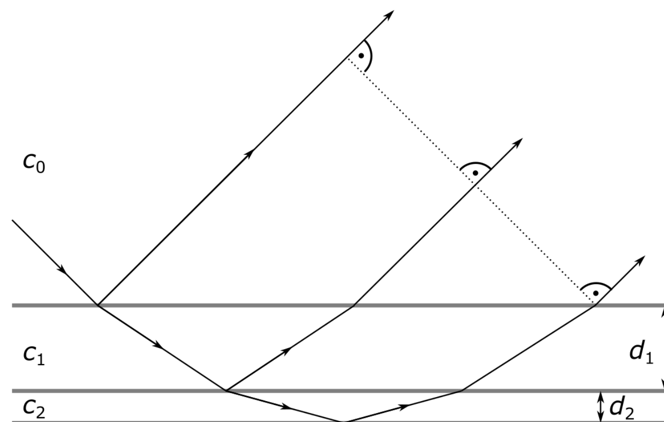

Figure 2.4: Visualization of the X-ray beam path in a two layer structure with layer thicknesses d_1 and d_2 and refractive indices $c_2 > c_1 > c_0$ for X-ray interference in thin films.

keep the value of the incident beam and the detector angle identical. An example is shown in Figure 2.5. The Kiessig fringes allow the determination of the layer thicknesses from this graph, as the thickness of a layer is inversely proportional to the distance between the interference fringes. In multilayer structures the intensity of these fringes decreases drastically the deeper a layer lies underneath the sample surface [31], usually allowing thickness determination only of the first two to three layers. Because the reflectivity curve can get very complex if multiple layers are involved, the values are not extracted from the curve directly, but are obtained by comparing the measured curve with a simulated reflectivity curve from the "Leptos 7.6" software. Intensity offsets between simulation and measurement occur at small angles, because the simulation assumes, that the area of incident of the X-ray beam is entirely on the sample surface. However, because of the small incident angle the area of incident is elongated in the sample plain and therefore exceeds the lateral sample size. XRR also allows an estimation of the roughness of the sample. A rougher surface produces more diffuse scatter, increasing the decay with 2θ of the reflected beam intensity. For most applications, however, AFM is better suited for measuring the surface roughness of a sample, as the resolution is significantly better.

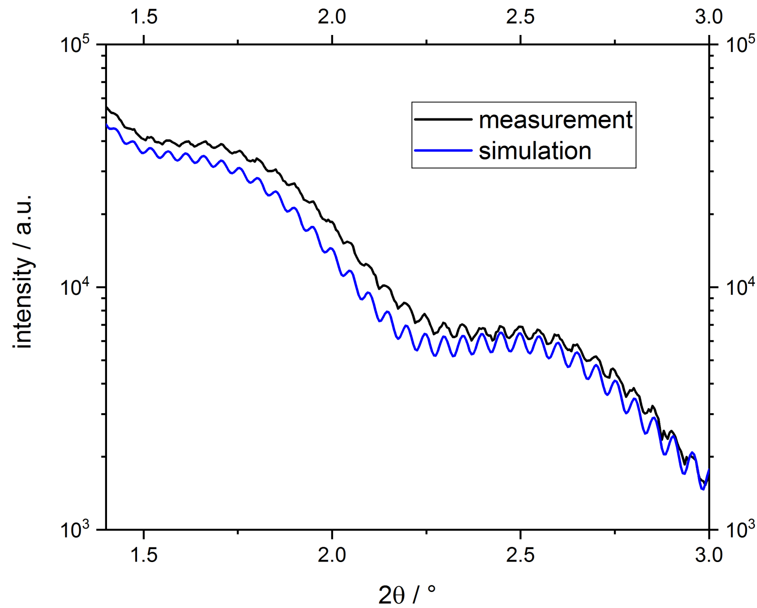

Figure 2.5: 2θ - ω scan for small angles of incidence of a $Hg_{1-x}Cd_xTe$ multilayer showing the total reflectivity with Kiessig fringes on top. The two frequencies represent two layers with different thicknesses and compositions.

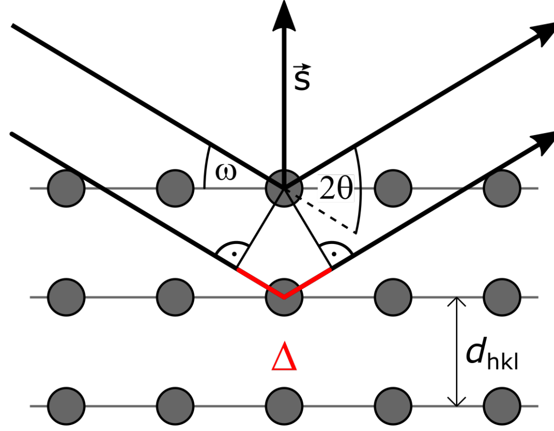

Figure 2.6: Sketch of the Bragg condition in a cubic crystal.

The following discusses the basic principle of HRXRD. A detailed description can be found in [32]. Diffraction occurs when each object in a periodic array scatters radiation coherently. For a wavelength λ similar to the distance between the atoms, they act as the scattering object, fixed in the periodic array of the crystal lattice. The interference of all these diffracted beams is constructive, when the plane normal for any parallel planes of atoms is parallel to the diffraction vector $\vec{s}$ [8] (the vector between incident and diffracted beam; cf. Figure 2.6). This then fulfils Bragg's law [33]

$$\Delta = \mathrm{n} \cdot \lambda = 2 d_{hkl} \sin(\theta) \tag{2.2}$$

for having constructive interference if the path difference Δ for waves redirected by adjacent lattice planes is an integer multiple of the wavelength. d_{hkl} is defined as the vector drawn from the origin of the crystal unit cell intersecting the first equivalent plane at a 90° angle. It can be resolved into the components $\vec{d}_{hkl} = h\vec{a} + k\vec{b} + l\vec{c}$, with $\vec{a}, \vec{b}, \vec{c}$ being any set of base vectors. A simple way to illustrate Bragg's law is the construction of an Ewald sphere, which is shown in Figure 2.7. From this we get an overview of the accessible reflective planes in HRXRD. This makes it necessary to switch from real space to reciprocal space. The reciprocal lattice vector is defined by

$$|d^*_{hkl}| = 1/|d_{hkl}| \tag{2.3}$$

and can be resolved into the following components:

$$\begin{aligned} \vec{d}^*_{hkl} &= h\vec{a}^* + k\vec{b}^* + l\vec{c}^* \\ \vec{a}^* &= 2\pi \tfrac{\vec{b}\times\vec{c}}{\vec{a}\cdot(\vec{b}\times\vec{c})} \\ \vec{b}^* &= 2\pi \tfrac{\vec{c}\times\vec{a}}{\vec{b}\cdot(\vec{c}\times\vec{a})} \\ \vec{c}^* &= 2\pi \tfrac{\vec{a}\times\vec{b}}{\vec{c}\cdot(\vec{a}\times\vec{b})} \end{aligned} \tag{2.4}$$

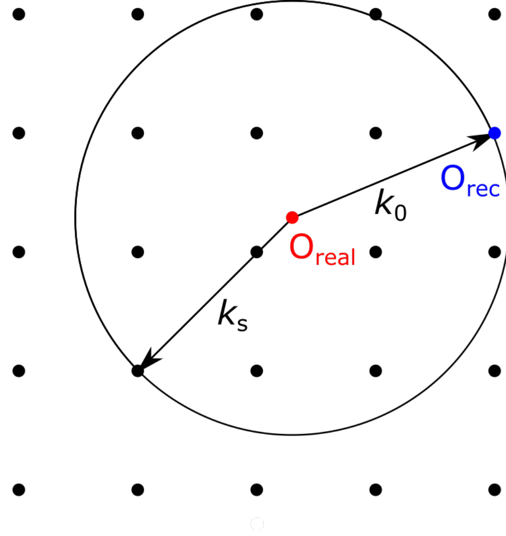

Figure 2.7: Exemplary construction of an Ewald sphere in reciprocal space.

The center of the Ewald sphere is the origin in real space (O_{real}). If $\vec{k}_0$ is the wave vector of the incident electron beam, which is always pointing to the origin in reciprocal space (O_{rec}), the radius of the Ewald sphere is $|k_0| = \frac{2\pi}{\lambda}$. By neglecting inelastic scattering, the diffracted beams wave vectors $\vec{k}_s$ have the same amplitude. ($|k_s| = |k_0|$). Therefore, all scattered beams lie on the surface of the Ewald sphere. If another reciprocal lattice point despite O_{rec} also lies on the surface of the Ewald sphere, the Laue condition

$$\Delta\vec{k} = \vec{k}_s - \vec{k}_0 = \vec{d}^*_{hkl} \tag{2.5}$$

is fulfilled. In this case elastic scattering takes place in the direction of $\vec{k}_n$. A short calculation shows that equation 2.5 is just another representation of Bragg's Law [34]. If the direction of the incident beam is changed, which in practice is done by rotating the sample, the Ewald sphere rotates around O_{rec}. Hence all accessible reflexes for a XRD scan lie within a sphere of radius $2|k_0| = \frac{4\pi}{\lambda}$. Additionally one has to consider the transmission shadow caused by the technical setup, which restricts the angle of incident and diffracted beam to values between 0° and 180°. An example for all the reflexes accessible in a zincblende crystal is shown in Figure 2.8. The black circle shows the maximum length of the scattering vector in reciprocal space ($k_{\mathrm{max}} = 4\pi/\lambda$), while the blue circles indicate the transmission shadow. Therefore, all accessible reflexes are in the white part. Because of the structure factor F_{hkl} in a zincblende lattice is only different from zero if hkl are all either odd or all even, only reflexes with these sets of indices are observable [32].

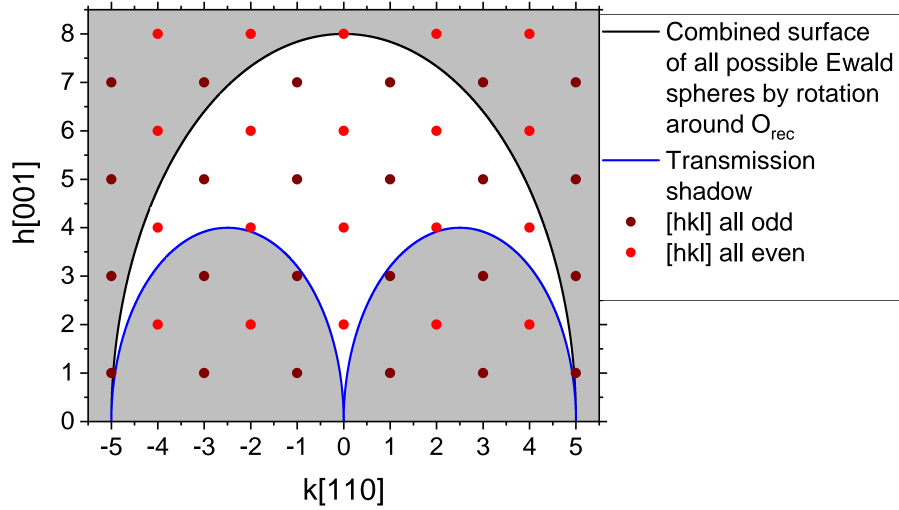

Figure 2.8: Schematic view of the accessible reflections in the reciprocal space, cut in the [001]-[110]-plane. In red there are all reflections were the indices are all even, all odd indices are shown in dark red. The white space indicates the accessible region according to the Ewald construction.

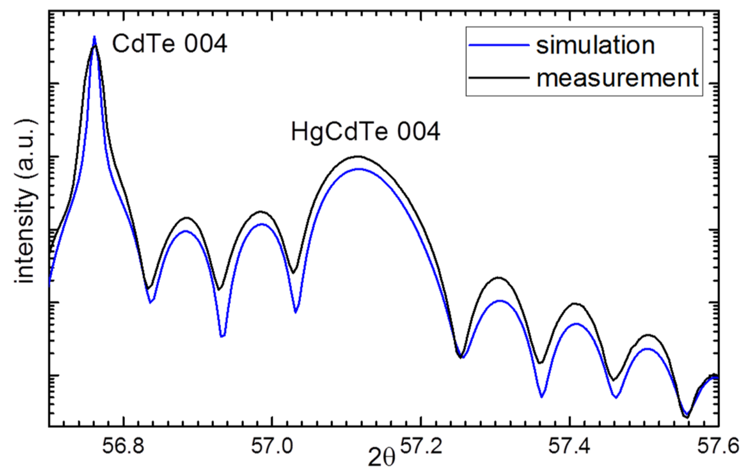

Figure 2.9: Exemplary 2θ - ω scan of the 004 reflex of a CdTe substrate with a $Hg_{1-x}Cd_xTe$ layer on top for the determination of layer thickness and material composition.

The different scan types are describing different traces in reciprocal space.

- An ω scan is an arc centered on the origin.
- A 2θ scan (detector scan) is an arc along the Ewald sphere circumference.
- A coupled $2\theta - \omega$ scan is a straight line pointing away from the origin.

There are several parameters of the sample that can be extracted from these different scans. ω scans are used to compare the crystal quality of different samples. Interference fringes in the $2\theta - \omega$ scan determine the layer thickness. Figure 2.9 shows an example of a $2\theta - \omega$ scan of a $Hg_{1-x}Cd_xTe$ layer on a CdTe substrate at the 004 reflex, which is chosen because it offers the highest intensity. For more complex layer stacks the measurement curves are again compared with a simulation provided by the "Leptos 7.6" software. The 2θ value of a peak for a specific material is dependent on the strain and, for ternary or higher order compounds, on their composition. Therefore, an additional measurement is necessary to acquire either strain or composition. The strain can be extracted independently from a reciprocal space map (RSM). For recording a RSM the 1D LynxEye detector is used, which allows to scan ω with an 1.15° broad window in 2θ, resulting in a three-dimensional data set of ω, 2θ and intensity. As the axis of ω and 2θ can be transformed into h and k, this scan covers a small area in the reciprocal space in Figure 2.8. An exemplary sketch of this process is shown in Figure 2.10. The position of the layer peak in this scan related to the substrate peak indicates the amount of strain present in the layer. If both peaks are showing the same value for the in-plane vector, hence having the same in-plane lattice constant, the layer is completely pseudomorphic. In a fully relaxed case layer and substrate peak lie on a line through the origin, therefore having the same lattice constant in and out-of-plane. The respective reflexes of partially strained/relaxed layers lie on a line in between the reflexes of pseudomorphic and fully relaxed reflex allowing to calculate the amount of strain present in a layer depending on the position in the RSM.

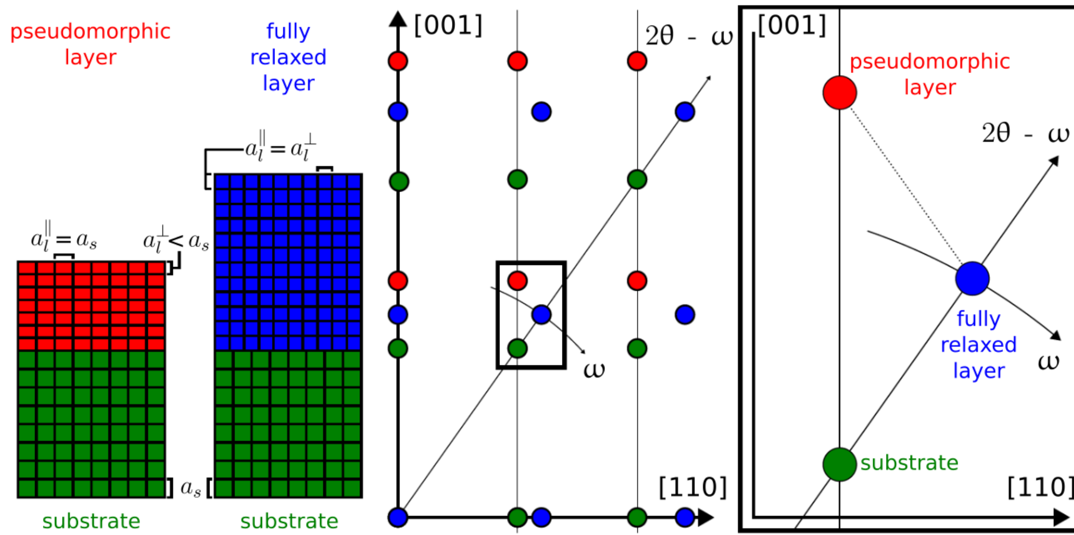

Figure 2.10: Left sketch shows a pseudomorphic layer in red and a fully relaxed layer in blue. Right sketch shows the position of their respective reflexes in the RSM. For partial relaxation the reflex lies on the dashed line connecting pseudomoprhic and relaxed layer reflex. Picture taken and translated from [35]. *Reprinted and translated with permission from Lukas Lunczer, Bandlückenmaximierung in hochverspannten, invertierten HgTe-Quantentrögen. Master's thesis, Julius Maximilians Universität, Würzburg, 2016.*

2.4 Reflection high energy electron diffraction

A very common technique used in the framework of MBE growth is reflection high energy electron diffraction (RHEED). This technique enables the analysis of the crystals surface structure at an atomic level and also to in situ monitor growth processes of thin films. It uses a collimated electron beam with energy of 12 keV. UHV is required for this technique, as the mean free path of the electrons has to be long enough for neglecting any other possible scattering events of the electrons beside the sample. The beam is hitting the sample surface under a small angle of incidence irradiating a $1 - 3$ mm^2 elongated area along the beam. Therefore, the information provided by RHEED is averaged over this macroscopic area. Additionally, due to the glancing incidence angle geometry combined with the low penetration depth of an electron beam into a crystal and the de Broglie wavelength of these electrons being in the order of ≈ 1.1 $\AA$, the majority of the electrons interacts only with the first few atomic layers of the crystal, making RHEED a very surface sensitive technique [36]. Multiple scattering however can cause electrons to penetrate deeper into the crystal, where the physical interpreta-

tion can become very complex. In the framework of this thesis RHEED was used only as a quantitative analysis of the scattered electrons based on the observation of the diffraction pattern on a fluorescent screen, therefore the discussion is limited accordingly.

The basic concept is shown schematically in Figure 2.11. Again an Ewald construction is used to illustrate the appearance of the diffraction pattern. So all wave vectors are on the surface of the Ewald sphere depicted in Figure 2.11. The diffraction pattern is constructed from the intersection of the Ewald sphere and the reciprocal lattice. This constructing process makes sure that both of the elastic scattering and diffraction conditions are fulfilled simultaneously [37]. In the simplest case of only considering atoms arranged equidistantly on a line along the incident beam, the crystal is a series of equidistant planes in reciprocal space perpendicular to the atom row [38]. A square lattice crystal then can simply be imagined as two atom rows, with one rotated by 90°. In reciprocal space this translates to a set of rods arranged in square equidistantly and perpendicular to the sample surface. The intersection of the Ewald sphere with the reciprocal lattice

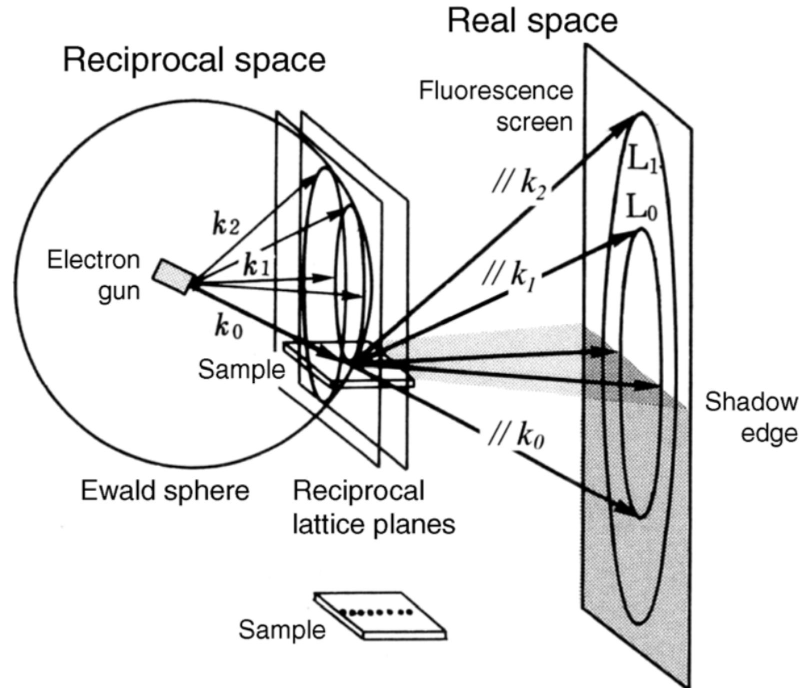

Figure 2.11: Sketch of the basic physical principle of RHEED. Image taken from [37]. (*Reprinted from Characterization of Materials , REFLECTION HIGH-ENERGY ELECTRON DIFFRACTION, S. Hasegawa, 2012, edited by E. N. Kaufmann; permission conveyed by John Wiley & Sons, Inc. through Copyright Clearance Center, Inc.*)

then leads to points in the diffraction pattern. In reality, however, this kind of lattice often translates into a diffraction pattern made out of lines perpendicular to the sample surface. These lines can be considered as elongated points, because duo to the spread in energy of the electrons the Ewald sphere has a finite extension and the reciprocal lattice rods are broadened by thermal vibration and stepped surfaces, so the intersection of Ewald sphere and reciprocal lattice has a finite size as well. In addition due to the large electron energy the Ewald sphere is much larger than the reciprocal lattice unit of the materials discussed here. Therefore, the Ewald sphere is cutting almost planarly through the reciprocal lattice, which stretches the diffraction pattern along the samples surface normal. This is visualized in the exemplary RHEED patterns for different sample surfaces observable on the fluorescent screen during MBE growth. Figure 2.12 displays the typical RHEED patterns of a flat [1], rough[2] and polycrystalline surface. A flat surface results in a streaky pattern with a sharp specular spot, island growth results in a spotty pattern and a polycrystalline surface results in a ring shaped pattern.

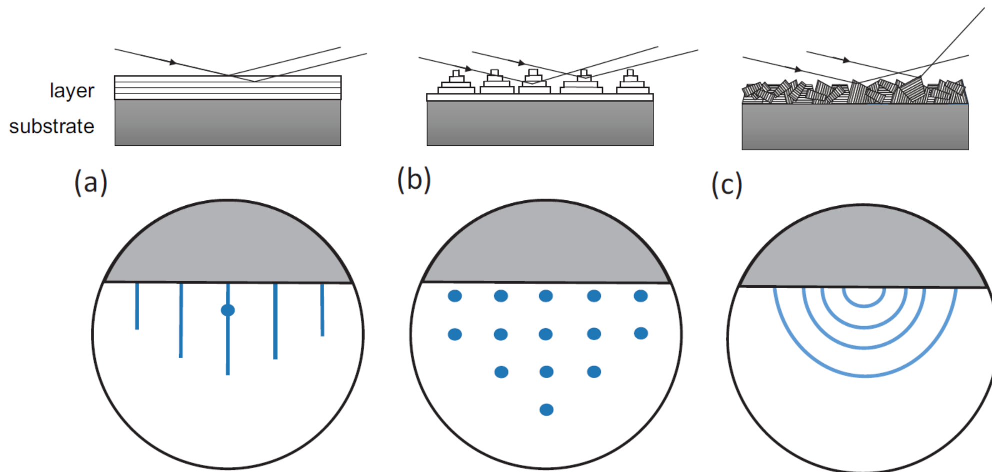

Figure 2.12: Observable RHEED patterns for different surfaces. a) streaks, b) spots, and c) rings, arise from the diffraction of a flat (2D), rough (3D) or polycrystalline surface respectively. Image taken from [39]). *Reprinted with permission from S. Schreyeck, Molecular Beam Epitaxy and Characterization of Bi-Based V_2VI_3 Topological Insulators. PhD thesis, Julius Maximilians Universität, Würzburg, 2016.*

[1] also referred to as two-dimensional surface
[2] also referred to as three-dimensional surface

3 Electrical transport

From an experimental perspective the main focus of research in $Hg_{1-x}Cd_xTe$ structures lies in electrical transport measurements at very low temperatures in high magnetic fields. These measurements are both used as a characterization tool for ensuring the layer quality as well as to investigate new physical phenomena in the materials. The first section discusses the design of the device and shows the lithographic processes used for fabricating devices from the MBE-grown samples. The second section of this chapter discusses the equations for calculating charge carrier density n and mobility μ from the measurable values. The third section gives an overview of the quantum Hall effect and the fourth section discusses the occurrence of a negative magneto resistance (MR) caused by the chiral anomaly. Both effects will be a relevant part for discussing the transport behaviour of Hg-containing layers in the following chapters.

3.1 Device design and fabrication

The device design of choice is a so called Hallbar structure. A sketch is shown in Figure 3.1. This design features a four-point measurement geometry, allowing currentless voltage measurements. By applying a driving current via the excitation voltage V_{exc} from contact 1 to 6 and measuring the voltage drop between pairs of contacts 2 to 5, the resistance of the leads has no influence. By comparing the measured voltage drop (longitudinal V_{xx} and horizontal V_{xy}) to the one at a reference resistance (R_{ref}), the longitudinal sheet resistance R_{xx} and the horizontal or Hall resistance R_{xy} of the layer material can be obtained. The Fermi energy E_{F} in the structure can be controlled by applying a voltage V_{g} to the gate electrode on top of the structure, enabling measurements at different charge carrier densities of the structure.

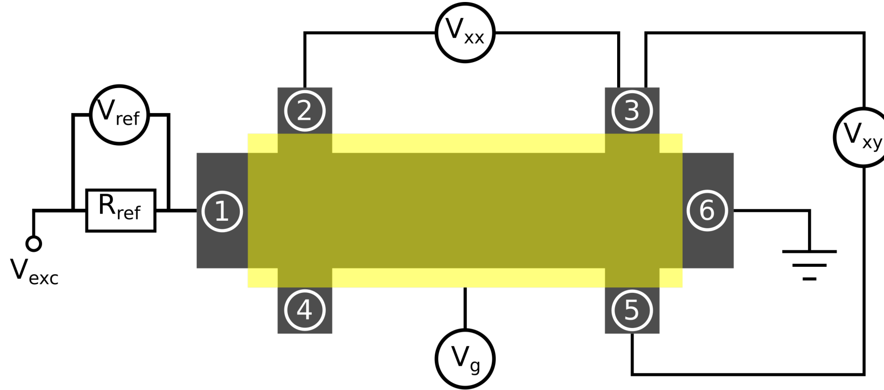

Figure 3.1: Schematic measurement circuit for a Hallbar sample design with a gate electrode (yellow area) on top. The ohmic contacts are labelled 1 through 6.

For the fabrication of the Hallbar structure optical lithography is used. There are some tasks which are repeated in every lithography step, hence a general description is given at first. Usually, fabrication steps start with covering the sample with resist by applying a drop of resist on the sample and rotate it in the spin-coater to achieve a homogeneous distribution across the sample surface. One has to distinguish between two types of resist, positive and negative. The basic differences are:

- Positive resist consists of long molecules, which decay under illumination and can then be resolved by a proper chemical, usually based on TMAH (Tetramethylammoniumhydroxid).
- Negative resist consists of short molecules, which cross link under illumination and by applying heat. Therefore, only non-illuminated parts are getting resolved.

After spin-coating for 20 s at 6000 rpm, the resist is baked at 80 °C for 2 min, to evaporate the solvent. All lithography processes for the device fabrication in the framework of this thesis were using the negative resist "Allresist ARN 4340". Afterwards, the sample is put in the mask-aligner. Here, the structures which are supposed to be transferred onto the sample are on a glass plate as a thin layer of chromium, which is put in between the sample and a mercury vapor lamp ($\lambda = (310 - 440)$ nm). Only the glass part is transparent, keeping the resist directly below the chromium unaffected. A baking at 80 °C for 6 min finalizes the cross link process and rinsing in a development chemical (Allresist AR300-47), then resolves only the illuminated part. Now the resist is a negative image (or positive for a different resist) of the structure on the mask. Assuming the resist is mechanically

and chemically stable, anything that is now done to the sample surface only affects the non-covered part. After dissolving the remaining resist chemically (in this case with acetone) the formerly covered part is unaffected. This is the basic principle of all lithography steps and is repeated for every fabrication step.

Some exemplary pictures of the different fabrication steps are shown in Figure 3.2. The most important characteristic of $Hg_{1-x}Cd_xTe$, that has to be considered during lithography is its susceptibility to temperature. Hg tends to evaporate out of $Hg_{1-x}Cd_xTe$ for temperatures above 80°C, which is lower than many common manufacturer's instructions for baking procedures during lithography. Therefore all fabrication steps involving temperature have been redesigned to keep the maximum temperature at 80°C. In the first fabrication step of the Hallbar structure, the MBE-grown layer is etched into the desired shape called mesa, which in this case are two Hallbar structures with a size of 600 µm by 200 µm for the bigger Hallbar (bHb) and 30 µm by 10 µm for the smaller Hallbar (sHb) respectively. This is done by putting a Barium fluoride (BaF_2) etch mask on top of the sample in the shape of the desired structure. Ion beam etching is used to remove the uncovered

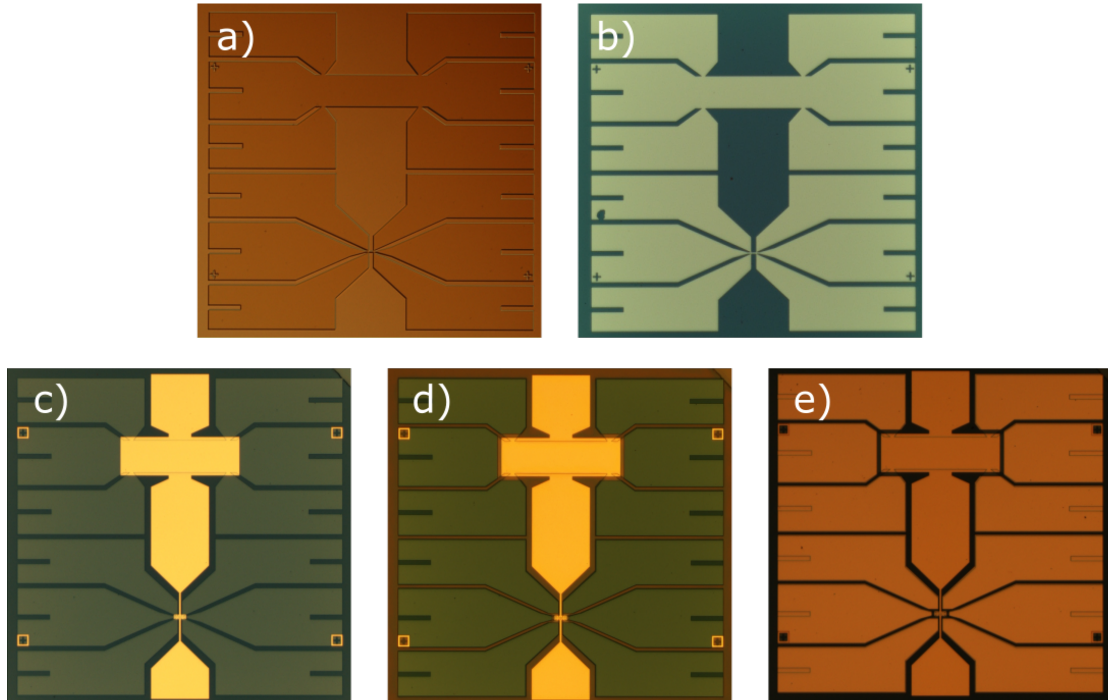

Figure 3.2: Micro photographs of the major fabrication steps for producing a Hallbar sample from MBE-grown Hg(Cd)Te. a) Hallbar shaped Mesa. b) Insulator covering. c) Gate electrode metallized. d) Insulator removed under the ohmic contact pads. e) Final sample with metallized ohmic contact pads.

parts resulting in a free standing Hallbar structure (cf. Figure 3.2 a)). Afterwards, the sample is covered with a 110 nm silicon dioxide (SiO_2), silicon nitride (SiN) superlattice (cf. Figure 3.2 b)), which functions as a insulator to keep the Hg-containing layer electrically separated from the gate electrode (cf. Figure 3.2 c)). For the ohmic contacts the insulator is removed from the respective positions (cf. Figure 3.2 d)) and the metallic contact material is applied (cf. Figure 3.2 e)). The final sample is glued into a chipcarrier (cf. Figure 3.3) to make a later mounting into the measurement setup possible. Gold wires connect the contact pads of the device with the chipcarrier contacts. Finally the sample is put into a cryostat for achieving low temperatures at high magnetic fields. The cryostat available at the institute of EPIII can achieve magnetic fields up to $B = 14$ T. Measurements at higher magnetic fields (up to $B = 33$ T) were done at the high magnetic field laboratory (HMFL) at the Radboud University in Nijmegen. All samples were cooled in a liquid He bath. By reducing the pressure with a rotary vane pump, the boiling point of the operating He can be reduced due to the partial vacuum, resulting in a measurement temperature of 1.4 K in both cryostats.

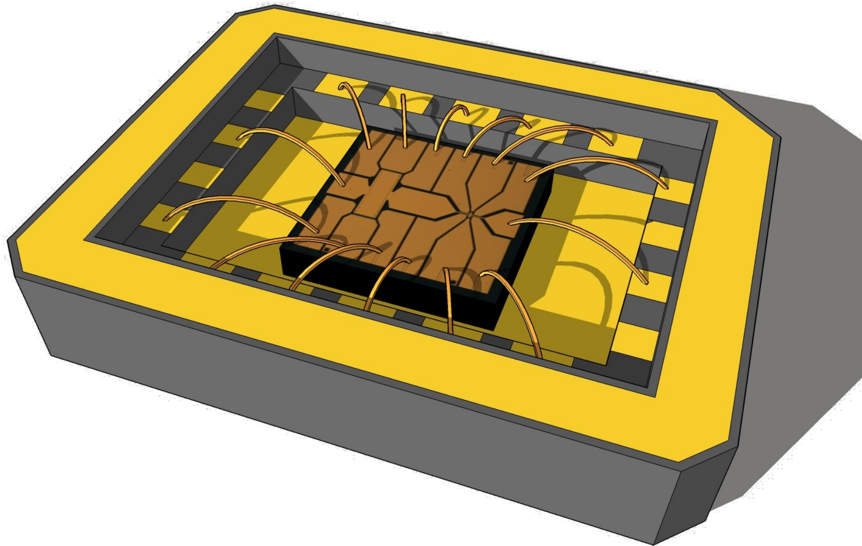

Figure 3.3: Sketch of the final sample glued inside a chipcarrier. Sample and chipcarrier contacts are connected with gold wires.

3.2 Charge carrier density and mobility

The charge carrier density n and mobility μ can be calculated from the magnetic field (B) dependence of R_{xx} and R_{xy}. In the context of this thesis, these values are used as a characterization tool for 2DEG structures, therefore n in this case is the two-dimensional charge carrier density. Assuming a driving current in x-direction and a magnetic field in z-direction, the density n can then be obtained from the slope of the resistance curve by

$$\frac{R_{\mathrm{xy}}}{B} = \frac{\rho_{xy}}{B} = \frac{E_y}{j_x}\frac{1}{B} = \frac{1}{ne}, \tag{3.1}$$

because for a 2D channel geometry there is no difference between Hall resistance and resistivity ($R_{\mathrm{xy}} = \rho_{xy}$) according to [40]. The charge carrier mobility is dependent on n and the conductivity σ for $B = 0$ via

$$\sigma = ne\mu. \tag{3.2}$$

With the current density $j = -nev = \frac{ne^2\tau}{m}E = \sigma E$ follows

$$\mu = \frac{1}{\rho_{xx}(B=0)ne}. \tag{3.3}$$

The sheet resistivity is connected with the measured sheet resistance by

$$\rho_{xx} = R_{\mathrm{xx}} \cdot w/l. \tag{3.4}$$

where w and l are the width and length of the Hallbar. To summarize, with equation 3.1 and 3.3 charge carrier density n and mobility μ can be calculated from the slope of the Hall resistance and the sheet resistance at zero magnetic field.

3.3 Quantum Hall effect

The Quantum Hall effect (QHE) [1] was one of the major discoveries in solid state physics and was rewarded with the nobel price for Klaus von Klitzing in 1985 [3]. It occurs when an electron system is restricted in one of its spatial dimensions (here z) strong enough for the electron energy

$$E_j(\vec{k}) = \frac{\hbar^2}{2m_x^\star}k_x^2 + \frac{\hbar^2}{2m_y^\star}k_y^2 + \epsilon_j \tag{3.5}$$

to become quantized in that direction. Here, all bands are assumed to be parabolic, with $m^\star$ being the effective mass of the electron in the directions, where free movement is allowed. ϵ_j with $j = 1, 2, 3, ...$ is resembling discrete energy levels in z-direction. Such a system is called a two-dimensional electron gas (2DEG). The single energy levels forming the energy spectrum described by $E_j(\vec{k})$ are often referred to as subbands. A magnetic field B perpendicular to the x,y-plane bends the movement of the electrons to become circles with the cyclotron frequency

$$\omega_c = -\frac{eB}{m_\parallel^\star} \tag{3.6}$$

where $m_\parallel^\star$ is the effective mass parallel to the circular movement. This causes an additional quantization of the subbands leading to a single particle energy of

$$E_{j,n,s} = \epsilon_j + (\nu + \frac{1}{2})\hbar\omega_c + sg\mu_B B, \tag{3.7}$$

the so called Landau levels. $\nu = 0, 1, 2, ...$ is the Landau level index, $s = \pm 1/2$ is the spin quantum number, μ_B the Bohr magneton and g the Landé-factor of the electrons. These Landau levels are spaced in energy by $\hbar\omega_c$.

The upcoming discussion assumes a Hallbar device design as shown in Figure 3.1, with the current passing a 2DEG in the plane, while an external magnetic field is applied perpendicular to the plane. An increasing magnetic field increases ω_c as well, pushing the Landau levels one after the other above E_F. In between the

[1] For the purpose of discussing the results of this thesis it is sufficient to stick to the QHE found by Klitzing in 1980, which today is better known as Integer Quantum Hall Effect (IQHE) as the Landau level index ν in this case only takes integer values. This term distinguishes the QHE discussed above from the so called Fractional Quantum Hall Effect (FQHE), where R_xy can take values of $h/(\nu e^2)$ with $\nu = 1/3$ and $\nu = 2/3$, found in 1982 and rewarded with the nobel price in 1998 for Dan C. Tsui, Horst L. Störmer and Robert B. Laughlin. For further information on this the reader is referred to the literature.

crossing of the ν and $\nu+1$ Landau level with the Fermi energy, R_{xy} stays constant at specific values of $h/(\nu e^2)$ with $\nu = 1, 2, 3, ...$, sequentially changing these values whenever a Landau level crosses E_{F}.

This can be explained by looking at the motion of electrons at the edge of the 2DEG, visualized in Figure 3.4. These electrons are not able to perform a full circle, because the area of motion is restricted by the electrons hitting the 2DEG edge. In the case of only considering elastic scattering, this results in electrons moving in pitch circles (so called skipping orbits) along the edges. The electrochemical potential at the sample edge is increasing towards the vacuum potential. As a result the Landau levels, usually lying below E_{F}, cross it close to the sample edge, which allows charge transport through these one-dimensional edge channels, even when there are no accessible energy states inside the sample. All electrons moving in one direction are propagating at one side of the sample, while all electrons moving in the other direction are at the opposite side, because of the direction of the rotation implied on the electrons by the Lorentz force. When a voltage is applied from the left side of the sample to the right side the chemical potential of the left moving electrons μ_L is raised, while the chemical potential of the right moving electrons μ_R is lowered. Hence, when measuring R_{xy}, one measures the resistance

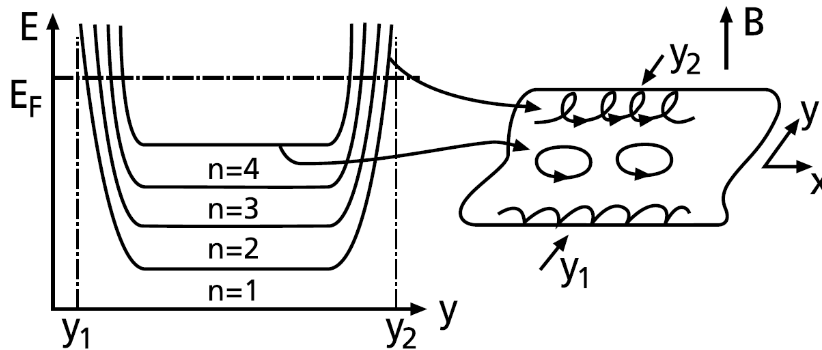

Figure 3.4: Formation of edge channels in a 2DEG in the presence of an out-of-plane magnetic field. The electron states are quantized in Landau levels, which corresponds to closed cyclotron orbits inside the sample. At the sample edges, y_1 and y_2, the electron trajectories become highly curved, which leads to an increase in energy of the Landau states and finally a crossing of the Fermi energy E_{F}. Image taken from [41] (*Reprinted from Festkörperphysik: Einführung in die Grundlagen, H. Ibach and H. Lüth, Springer-Lehrbuch, 7. edition, 2009; permission conveyed by Springer Nature through Copyright Clearance Center, Inc.*)

between the left moving and right moving edge channels. Whenever a Landau level is pushed above E_F, an edge channel is removed, leading to a stepwise increase of R_{xy}.

The existence of edge channels gives rise to another interesting transport effect. Because any scattered electron in a specific edge channel is forced back in its original direction by the Lorentz force, and scattering into an edge channel pointing in the opposite direction is not possible due to the lack of states inside the sample, the resistance of these edge channels is zero. However, when a Landau level is crossing E_F scattering between the channels is allowed, resulting in a resistance peak. These magnetic field drive resistance oscillations are called Shubnikov - de Haas (SdH) oscillations. Figure 3.5 shows an exemplary measurement of the QHE in R_{xy} and the SdH oscillations in R_{xx} measured in a HgTe QW at a temperature of 4.2 K. Material defects can cause deviations from the magnetic field dependent behaviour expected from the theory, which is covered for example in [40]. Hence

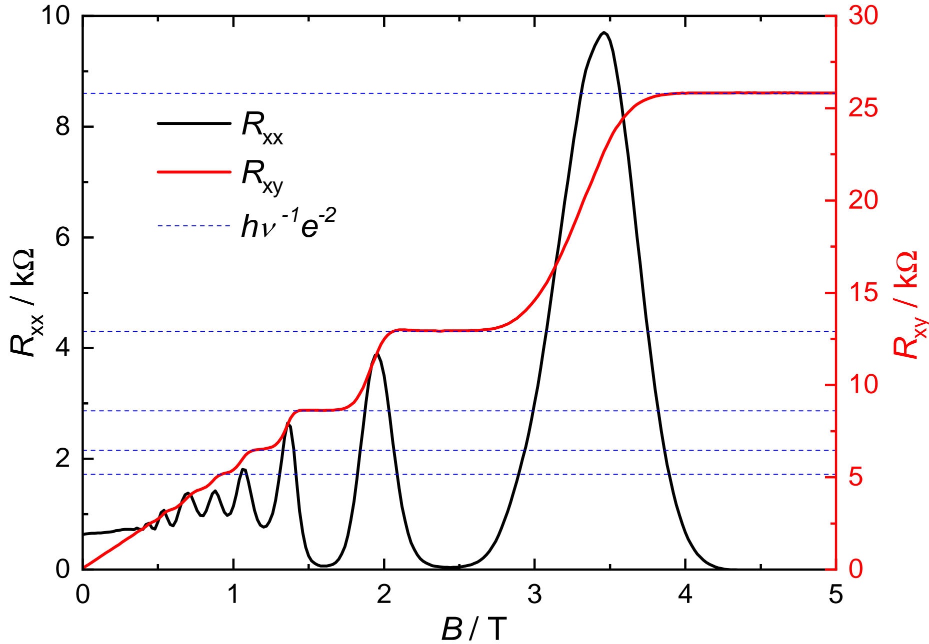

Figure 3.5: Exemplary measurement of the integer QHE in a HgTe QW at a temperature of 4.2 K (sample dimensions: 9 nm - 200 µm - 600 µm). The black curve shows SdH oscillations in R_{xx}, while the red curve shows the the stepwise increase of R_{xy} with increasing magnetic field associated with the QHE. Dashed blue lines indicate the resistance values $h/(\nu e^2)$ with $\nu = 1, 2, 3, ...$ of the n-th Landau level in R_{xy}.

in the framework of this thesis the QHE effect is used for quality control of HgTe quantum wells, specifically if the resistance plateaus match the expected value, if the B-field value of the SdH peak match the change from one resistance plateau to the other and if R_{xx} is going to zero for higher fields in between two SdH oscillations.

The occurrence of the QHE is a signature feature of a 2DEG. However, there are several ways to create a 2DEG in solid state heterostructures, which needs to be considered for drawing a conclusion from the observance of a QHE signal about the electrical transport properties of a material.
The most straight forward way is to fabricate a conducting material layer thin enough, that the spatial confinement restricts the movement of the charge carriers in one direction. This is the reason of the observation of the QHE in HgTe layers below a thickness of roughly 20 nm.
Other common structures, which can exhibit a 2DEG are field effect transistors (FET) and semiconductor heterostructures. In a FET a gate electrode parallel to a semiconductor layer applies an external electric field. At a certain strength the electric field bends the conduction band below E_{F} (or the valence band above E_{F}, depending on the polarity of the electric field) at the surface of the semiconductor. The charge carriers accumulated at the surface can move freely in two directions, but are restricted in z, the direction parallel to the surface normal. The most prominent example for 2DEGs in semiconductor heterostructures is the interface between GaAs and AlGaAs layers, where the continuity condition bends the conduction and valence band in such a way, that a 2DEG arises at the interface [42]. 2DEGs can also occur on the surface of topological insulators due to their specific electron band structure, which is shown in chapter 4.2.

3.4 Chiral anomaly and negative magneto resistance

Negative MR caused by chiral anomaly is usually associated with Weyl semimetals [43]. However Gorbar *et al.* have shown, that any Dirac semimetal is transformed into a Weyl semimetal in the presence of an external magnetic field $\vec{B}$ [44]. They calculated the chiral shift

$$\vec{b} = -\frac{ge\vec{B}\mu_0}{8\pi^2\nu_F^2 c}, \tag{3.8}$$

which gives a value for the splitting of the Dirac point in k-space into a pair of Weyl points with opposite chirality resulting in an equal number of right-handed (RH) and left-handed (LH) species of Weyl fermions. Here, ν_F is the Fermi velocity, μ_0 the chemical potential, c the speed of light, e the elemental charge and g a dimensional coupling constant.

An external magnetic field however will also introduce Landau levels with a continuous dispersion parallel to the field direction. The zero order Landau level ($n = 0$) shows a linear dispersion for the Weyl points, with velocities either parallel or antiparallel to the magnetic field dependent on the chirality. For any other order ($n \neq 0$) the Landau levels exhibit a normal dispersion (cf. Fig. 3.6). Therefore this can be treated as a one dimensional problem, as any electron propagation caused by this takes place only along the magnetic field lines, for a electric field parallel to it. In the present case of linear dispersion the acceleration of the electrons is

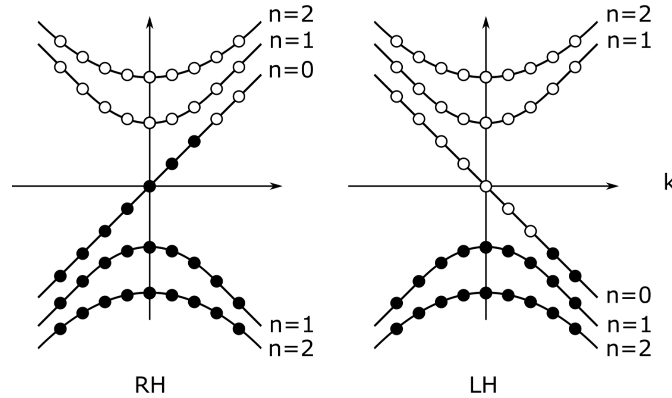

Figure 3.6: Dispersion law for the RH and LH Weyl point in 3 + 1 dimensions in the presence of a magnetic field in x-direction. Image based on [43]. (*Reprinted from The Adler Bell-Jackiw anomaly and Weyl fermions in a crystal, H.B. Nielsen and M. Ninomiya, Physics Letters B, 130(6):389-396, November 1983; permission conveyed through Copyright Clearance Center, Inc.*)

$\dot{k} = eE/\hbar$ according to the semiclassical equation of motion. For a quantization length L, the density of the state per L is $L\pi$ [43]. The rate of change of the number of electrons of the RH/LH Weyl node is

$$\frac{d(N_{R/L}^{1D})}{dt} = \pm L^{-1} \frac{L}{2\pi} \dot{k} = \pm \frac{e}{h} E. \tag{3.9}$$

So there is a creation of electrons at the Weyl node, therefore the charge Q is not conserved ($\dot{Q}_{R/L} = \dot{N}_{R/L}^{1D}$). In condensed matter however left and right handed Weyl nodes are connected through other bands, which leads to a charge pumping effect, as every electron that is created at one Weyl node is annihilated at the associated other. By combining the creation rate of the right handed particles with the annihilation rate of the left handed particles , the total number of charged particles changes with

$$\dot{Q}_{total} = N_R^{1D} + \bar{N}_L^{1D} = 2 \cdot \frac{e}{h} E. \tag{3.10}$$

Because a magnetic flux quantum occupies a cross sectional area of the one dimensional channels, equation 3.9 can be transformed into a three dimensional density change by setting $N^{3D} = B/\phi_0 \cdot N^{1D}$, and therefore

$$\frac{d(N_{R/L}^{3D})}{dt} = \pm \frac{e^2}{h^2} \vec{E} \cdot \vec{B}. \tag{3.11}$$

One can see from equation 3.11 that in a material with a pair of Weyl nodes of opposite chirality, a charge pumping effect from one Weyl node to the other occurs, leading to an additional current. This is observable in an decrease of the magnetic field dependent longitudinal resistance for $\vec{E} \parallel \vec{B}$, with a strong angle dependence due to the $\vec{E} \cdot \vec{B}$-term in equation 3.11. Measurements of this effect in $Hg_{1-x}Cd_xTe$ for different compositions can be found in chapter 6.2.1.

4 The material system $Hg_{1-x}Cd_xTe$

$Hg_{1-x}Cd_xTe$ is best known for its applications in infrared spectroscopy, as the accessible size of its band gap is easily adjustable by changing the composition x and can therefore range from 1.602 eV for CdTe down to -0.283 eV for HgTe. For understanding the properties of the ternary alloy $Hg_{1-x}Cd_xTe$, with x representing the concentration of Cd and $(1-x)$ representing the concentration of Hg respectively, it is favourably to emanate from the binary compounds for $x = 1$ (CdTe) and accordingly $x = 0$ (HgTe) and treat $Hg_{1-x}Cd_xTe$ as a mixture of these materials. With this approach the following chapter covers the crystal structure as well as the electronic band structure of $Hg_{1-x}Cd_xTe$ for different values of x.

4.1 Crystal structure

Both CdTe and HgTe crystals share a 1:1 ratio of elements from the second and sixth group of atoms on the periodic table and therefore belong to the group of II-VI semiconductors. Both materials share a zincblende crystal structure which consists of two face-centered cubic (fcc) sublattices with an offset of one fourth of a lattice constant a_0 in all spatial directions, with one sublattice assigned to either the group II element (Hg or Cd) or the group VI element (Te) [45]. A typical zincblende (based on the example of $Hg_{1-x}Cd_xTe$) is depicted in Figure 4.1 for a) a binary compound and b) a ternary compound. The pink spheres represent Te, the grey spheres Hg and the green spheres Cd. The space group of $Hg_{1-x}Cd_xTe$ is $F\bar{4}3m$, resulting in a sp^3- hybridization of the atom orbitals. The lattice constant of the binary compounds are 6.4815 Å for CdTe [23] and 6.46152 Å for HgTe [46]. The lattice constant of $Hg_{1-x}Cd_xTe$ depending on x is slightly different from a linear behaviour expected from Vegard's law and was found to be [23]

$$6.4614 + 0.00084x + 0.0168x^2 - 0.0057x^3, \tag{4.1}$$

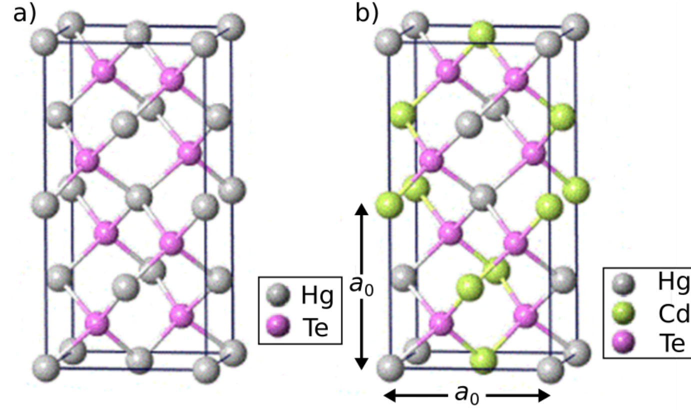

Figure 4.1: Zincblende crystal structure of a) HgTe and b) $Hg_{1-x}Cd_xTe$.

which shows only slight deviations for the extreme cases of ±0.001 Å for $x = 0$ and ±0.01 Å for $x = 1$ compared to the values mentioned above. Because of the similar lattice constants $Hg_{1-x}Cd_xTe$ can be grown in any composition desired. Clustering of CdTe or HgTe is not expected, as the substitution of Hg and Cd in the crystal structure is almost randomly with a tendency of preferring equal distribution of Hg and Cd in a unit cell [45]. However, when growing layers one has to consider, that in a zincblende unit cell there is one Te atom surrounded by four Hg (or Cd) atoms, allowing only compositions with multiples of $x = 0.25$. Hence, all other concentrations have to be mixtures of unit cells with $x = 0, 0.25, 0.5, 0.75, 1$. If the total composition differs from these values, microscopic concentration fluctuations in the layer are inevitable.

4.2 Band structure

The band structure of $Hg_{1-x}Cd_xTe$ can be separated into three different topological regimes, dependent on the Cd concentration x: a semiconductor state for compositions closer to CdTe ($x > x_c$), a topological insulator state for compositions closer to HgTe ($x < x_c$), and in between these two a Dirac semimetal state at $x = x_c$. It is therefore natural to start the discussion with the band structures of the binary compounds. CdTe in this case shows a very typical band structure for semiconductors with a zincblende crystal structure, similar to GaAs (cf. Figure 4.3). The part of the band structure that defines the different regimes in $Hg_{1-x}Cd_xTe$ is the band gap region in the vicinity of the Γ-point ($k = 0$). Because of the high mass of elements like Cd and Hg a number of relativistic corrections have to be taken into account in addition to the non-relativistic Hamiltonian

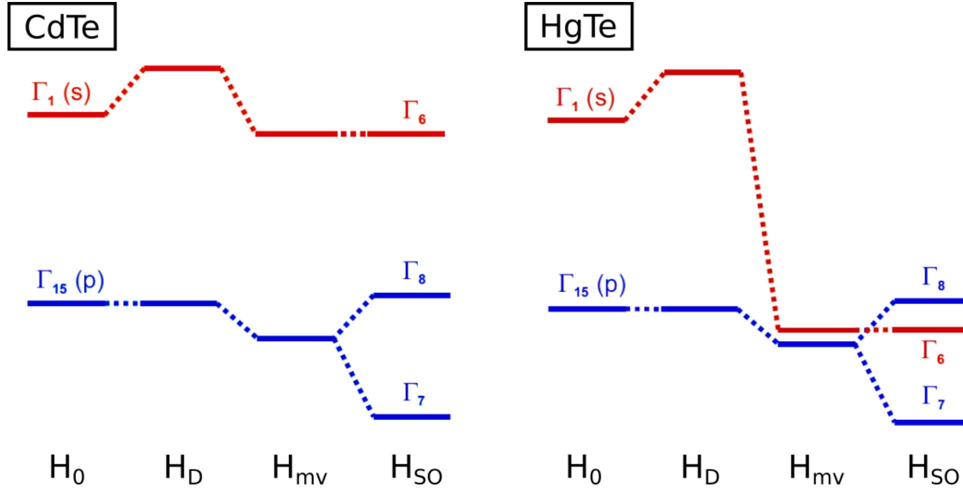

Figure 4.2: Influence of relativistic corrections onto the band structure of CdTe and HgTe. The strong mass velocity correction for the Hg s-states leads to a band inversion in HgTe.

H_1. Their influence on the energy values of the gap defining bands is visualized in Figure 4.2. As the band gap is defined by the distance between Γ_6 and Γ_8-band, the band gap value changes its sign by ranging from +1.602 eV in CdTe to −0.283 eV in HgTe. The energetically lowest conduction band is of Γ_6-type, showing s-type symmetry with a total angular momentum of $j = 1/2$. The Darwin term H_D takes care of the change in potential energy of the electron due to its interaction with the nucleus. It affects only the s-orbitals and has almost the same value for HgTe and CdTe. The mass-velocity H_mv corrects the kinetic energy operator by considering the relativistic increase of mass. It induces a very different correction in the two materials due to the large difference between the atomic masses of Cd and Hg ($M_\mathrm{Cd} = 112.4$ u , $M_\mathrm{Hg} = 200.6$ u), which brings valence and conduction band in HgTe closer together. The spin-orbit correction (H_SO) considers the interaction of the electron's spin and its orbital motion in the electrostatic field of the positively charged nucleus. Because its strength is dominated by the Te, there is no significant difference of the spin orbit interaction between CdTe and HgTe. In addition to energetic corrections, the spin orbit interaction (SO) now has a significant influence on the shape of the valence band structure, because it also causes a splitting of degenerate states. In a tight-binding picture without spin, the electron states at the valence band edge are p-like (orbital angular momentum l=1). With SO taken into account, the highest valence band shows electronic states with $j = 3/2$ and $j = 1/2$. These states split into Γ_8 and Γ_7, while the Γ_7-band is shifted downwards in energy. Therefore, all relativistic corrections considered, the Γ_6-states switch position with the Γ_8-states on the energy scale in HgTe. A negative band gap

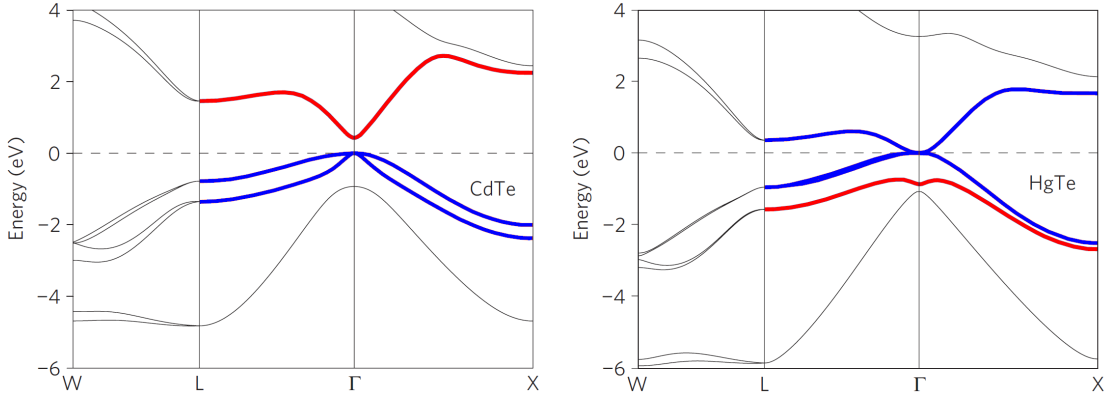

Figure 4.3: Band structure of CdTe and HgTe. In red is the Γ_6-band and in blue the two Γ_8-bands. Image taken from [47]. *Reprinted from Tunable multifunctional topological insulators in ternary Heusler compounds, S. Chadov, Nature Materials, 9(7):541–545, July 2010; permission conveyed through Copyright Clearance Center, Inc.*)

value is therefore referred to as an inverted band structure. The band structures of both CdTe and HgTe are visualized in Figure 4.3. The Γ_8 splits into $\Gamma_8^{1/2}$ and $\Gamma_8^{3/2}$, also referred to as light hole (LH) and heavy hole (HH) Γ_8, which form the conduction and valence band, respectively. These are degenerate at $k = 0$ due to the cubic symmetry in a strain free zincblende crystal. Hence, HgTe is actually a semimetal.

There are several interesting physical phenomena caused by the inversion of the band structure in HgTe. The most famous one is the topological insulator. With regard to the interpretation of the measured data in the chapters 5 and 6, only a shortened description is presented here. A more detailed description can be found in [48]. At the interface of materials with different band order the continuity condition forces a crossing of the inverted bands to regain a non-inverted band structure. Hence, the band inversion is lifted at the interface of HgTe to any other material with normal band order (e.g. CdTe or vacuum). As a consequence conducting states are formed at the surface of HgTe. Additionally, the degeneracy of the Γ_8-states at $k = 0$ can be lifted by applying uniaxial strain[1] to HgTe [49]. Combining these two effects results in a finite band gap in the bulk with conducting states at the surface as depicted in Figure 4.4.

[1]The effect of strain on the band structure of $Hg_{1-x}Cd_xTe$ is discussed in detail in the following section with respect to the strain applied by a CdTe substrate (cf. Figure 4.7).

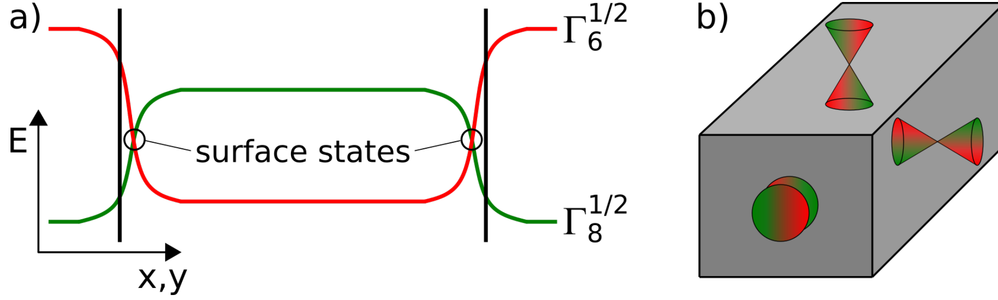

Figure 4.4: a) Band dispersion at the interface of materials with normal (left and right) and inverted band structure (middle). The continuity condition forces a band crossing at the the material edge. b) Thereby a 2DEG arises on every surface of a 3D material slab.

A similar idea lies behind the creation of a Dirac semimetal state in $Hg_{1-x}Cd_xTe$. With the band gap value being positive in CdTe and negative in HgTe, it is obvious that by adjusting the composition in $Hg_{1-x}Cd_xTe$, one can achieve a semimetal state (band gap = 0), where the Γ_6- and Γ_8-bands are touching each other at $k = 0$. This is visualized by three band structures around the critical concentration x_c in Figure 4.5 for k values close to zero. The left picture shows a band structure similar to CdTe. The $\Gamma_6^{1/2}$ is the conduction band while the Γ_8 bands having valence band character, representing a normal band ordering

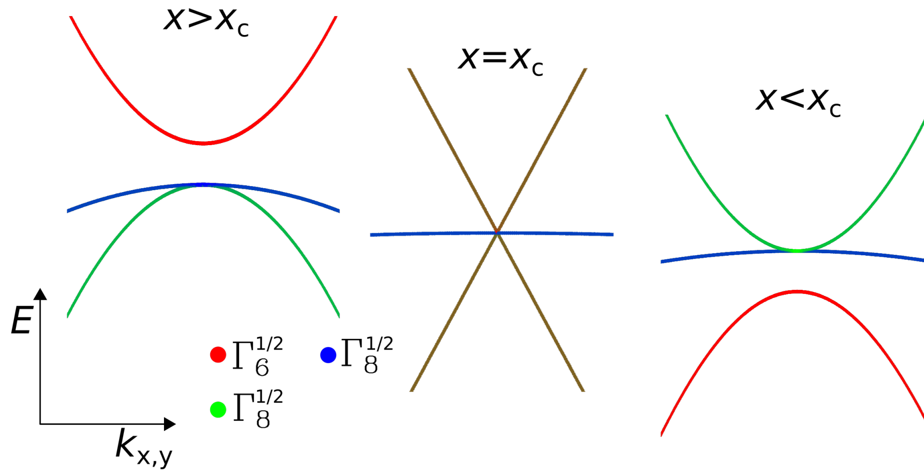

Figure 4.5: Sketch of the band structure of $Hg_{1-x}Cd_xTe$ for three different topological phases depending on the Cd concentration x. A trivial insulator for $x > x_c$, a Dirac semimetal for $x = x_c$ and a topological insulator for $x < x_c$. The character of the different bands is indicated by colour. Olive shows the combination of $\Gamma_6^{1/2}$ and $\Gamma_8^{1/2}$.

for $x > x_c$. For HgTe the energetic ordering of the bands is inverted (cf. right picture in Figure 4.5). The Γ_8 bands are energetically above the $\Gamma_6^{1/2}$ band. The $\Gamma_6^{1/2}$ and $\Gamma_8^{1/2}$ can be brought into proximity by adjusting the composition until they form a Dirac state for $x = x_c$, as shown in the center of Figure 4.5. The linear dispersion for this composition gives rise to the chiral anomaly in magneto transport, first predicted by Nielsen et.al [43]. In magneto transport it manifests itself in a decrease in R_{xx} with increasing B-field, if driving current and B-field are parallel. So the magneto resistance ($MR = R_{\mathrm{xx}}(B) - R_{\mathrm{xx}}(B = 0)$) becomes negative. An introduction to the theoretical concepts of a negative MR caused by the chiral anomaly can be found in chapter 3.4.

Additionally, due to the hybridization of $\Gamma_6^{1/2}$- and $\Gamma_8^{1/2}$-band, there is no distinct character of these bands any more when $x = x_c$, while the $\Gamma_8^{3/2}$ state remains unaffected, as indicated by the colouring. Therefore, in $Hg_{1-x_c}Cd_{x_c}Te$ some $\Gamma_6^{1/2}$-states are still energetically lower compared to their respective $\Gamma_8^{1/2}$-states. Hence, the inversion of $\Gamma_6^{1/2}$- and $\Gamma_8^{1/2}$-bands, already discussed for HgTe, is still partially present. The following discusses the question if this partial inversion still leads to conducting surface states and how this is supposed to influence the electronic transport behaviour. As surface states only appear in finite-sized layers, in Figure 4.6 the band structure of a 500 nm thick layer (red) is added to the bulk band structure (black) of $Hg_{1-x}Cd_xTe$ for its three topological phases, all calculated by $k \cdot p$ theory [2]. For $x < x_c$, when the band structure is similar to HgTe strongly localized surface states appear deeply in the valence band and close to the conduction band edge (cf. Figure 4.6 a)). In Figure 4.6 b) one can see that the partial inversion at $x = x_c$ creates surface states between the Dirac cone and the weakly dispersing $\Gamma_8^{3/2}$ band. This also extends to compositions above and below x_c. For $x > x_c$, when the band structure is similar to CdTe, the surface states do not disappear, because the bottom band still contains some $\Gamma_6^{1/2}$ character at large k, as a consequence of the hybridization between the Γ_6 and Γ_8 orbitals. As the gap size increases with further increasing of x, the $\Gamma_6^{1/2}$-$\Gamma_8^{1/2}$-hybridization decreases and consequently the surface state becomes weaker as the share of Γ_6 in the lower band decreases.

[2] All $k \cdot p$ calculations shown (cf. Figure 4.6, 4.8, 4.9) are carried out by the simulation program written by Wouter Beugeling at the chair of EPIII at the Julius Maximilians Universität Würzburg. All interpretations are based on personal communications.

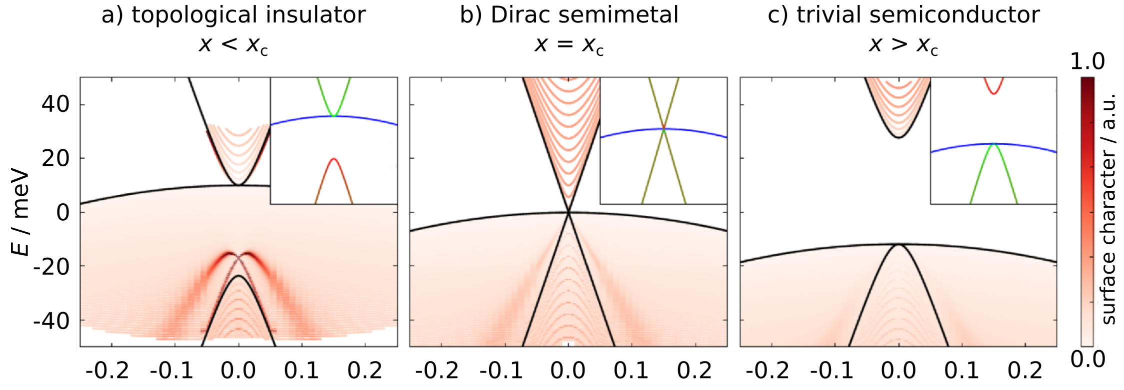

Figure 4.6: Comparison of the band structure calculated by $k \cdot p$ theory for a 500 nm thick layer (red) and the bulk (black) with: a) $x < x_c$, a topological semimetal; b) $x = x_c$; the Dirac semimetal; and c) $x > x_c$ a semiconductor. The energy is scaled with respect to the Dirac point at $x = x_c$ The red colourscale indicates the surface character. The insets show the bulk dispersions with colours indicating the orbital character as discussed in Figure 4.5.

However, the localization length of the surface states is inversely proportional to the local difference in band energy at a specific momentum. Hence, the localization length diverges near the Dirac point. Furthermore, the heavy hole band contributes a high density of states near the energy of the Dirac point, which makes a tuning of the chemical potential deeply into the valence band impossible. Thus, in a finite-sized sample around $x = x_c$ the impact of these surface is very small and it is therefore not expected to see an influence on the transport signal.

4.3 Influence of the CdTe substrate

The examined $Hg_{1-x}Cd_xTe$ layers are all grown on CdTe substrates. This choice, however, influences both the band structure and the crystal properties of $Hg_{1-x}Cd_xTe$ (the general aspect of strain has been discussed in chapter 1.4). Substrate and $Hg_{1-x}Cd_xTe$ are not lattice matched, thus putting tensile strain onto the layer, which is depending in strength on the composition. The strain in turn limits the total layer thickness, in order not to risk the incorporation of relaxation-induced defects into the material. Both thickness and strain cause differences in the band structure of a $Hg_{1-x}Cd_xTe$ layer, compared to the infinite, unstrained crystal discussed in the previous sections.

Strain in these materials has been a popular topic for a long time, especially in the context of the three dimensional topological insulator state in HgTe (cf. [50]. The two Γ_8-bands, normally degenerated at $k = 0$, became separated due to the symmetry reduction in the crystal as a result of the applied strain. A detailed theoretical discussion on the dispersion of these bands under the effect of uniaxial stress can be found in [51], which came up with an analytical description of the valence and conduction band dispersion in HgTe

$$E_{C,V} = Ak^2 \pm \sqrt{B^2k^4 - C^2\{k_\parallel^2 k_\perp^2 + 1/8ks^4[1 - \cos(4\phi)]\} + \Delta^2 - B\Delta(2k_\parallel^2 - k_\perp^2)}. \tag{4.2}$$

A visualization of equation 4.2 can be seen in Figure 4.7 for an unstrained system $\Delta = 0$ and tensile strain in the sample plain. The plus and minus sign addresses the conduction and the valence band, respectively. A, B and C are material parameters, with $A = 18.3$, $B = 22.3$ and $C^2 = 294$ all in atomic units [51]. Δ is half the size of the band gap value at $k = 0$. For HgTe strained on CdTe this is approximately $\Delta = -11$ meV [50]. $k_\parallel$ is aligned in the sample plain, with ϕ representing the angle between $k_\parallel$ and one high symmetry direction in the plane. Biaxial and uniaxial strain can be interchanged by simply switching their sign, as any biaxial tension is equivalent to uniaxial compression and vice versa [52].

With the changes of the band structure of pure HgTe from unstrained to tensile-strained, it becomes obvious that this is something that needs to be considered for discussing the band structure of $Hg_{1-x}Cd_xTe$ at $x = x_c$. Especially the fact

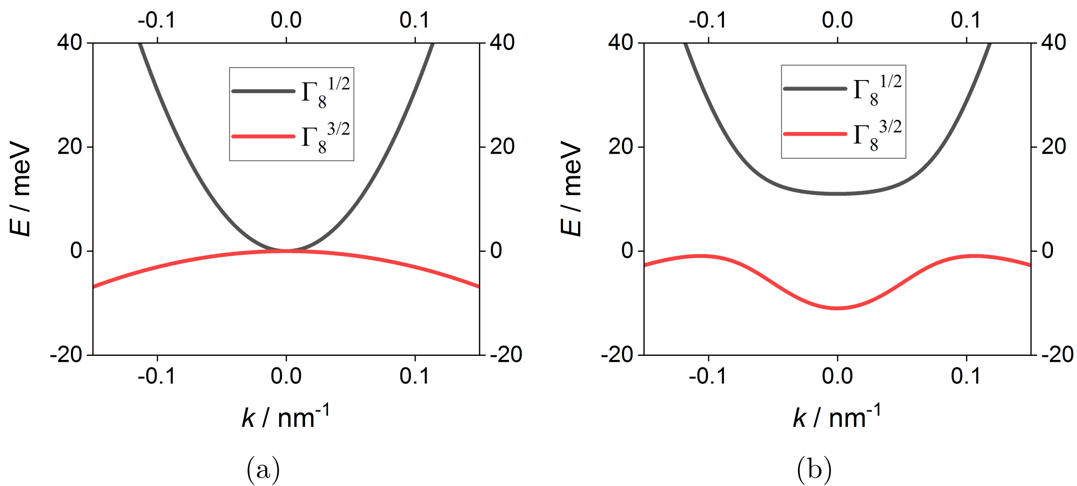

Figure 4.7: Energy dispersion of HgTe around $k = 0$ according to equation 4.2 at the band gap position for (a) the unstrained case ($\Delta = 0$ meV) and for (b) strain equal to the growth on a CdTe substrate ($\Delta = -11$ meV)

that the highest point in energy of the valence $\Gamma_8^{3/2}$ band is no longer at $k = 0$. As already mentioned, the difference in lattice constant of the CdTe substrate and the $Hg_{1-x}Cd_xTe$ layer causes an upper limit in layer thickness to avoid relaxation. There also exists a lower limit for the layer thickness to avoid significant changes in the band structure duo to size quantisation induced subband splitting in z-direction, hence creating a 2DEG. This is a very well studied topic of transport in semiconductors for more than 50 years (cf. [53]). In Hg-containing structures this is covered in [15]. So the size of the band gap is not only depending on strain and composition but also on the thickness of the conducting layer. To consider these three parameters $k \cdot p$ calculations were used to investigate the necessary values for creating a zero gap state in a $Hg_{1-x}Cd_xTe$. Figure 4.8 shows the Cd concentration x required to achieve a band gap value of zero depending on the thickness t of the $Hg_{1-x}Cd_xTe$ layer. As a change in the composition also affects the strain, the band gap value was calculated with respect to a CdTe substrate, therefore the influence of the strain and its change in this graph is taken into account in the change of x. For comparison Figure 4.8 also shows the same curve without considering any strain (black curve).

While the tensile strain in $Hg_{1-x}Cd_xTe$ caused by the CdTe substrate does alter the shape of the band structure and is changing the value of x_c, it does not prevent the appearance of a linear crossing at the Γ-point. This is visualized in Figure 4.9.

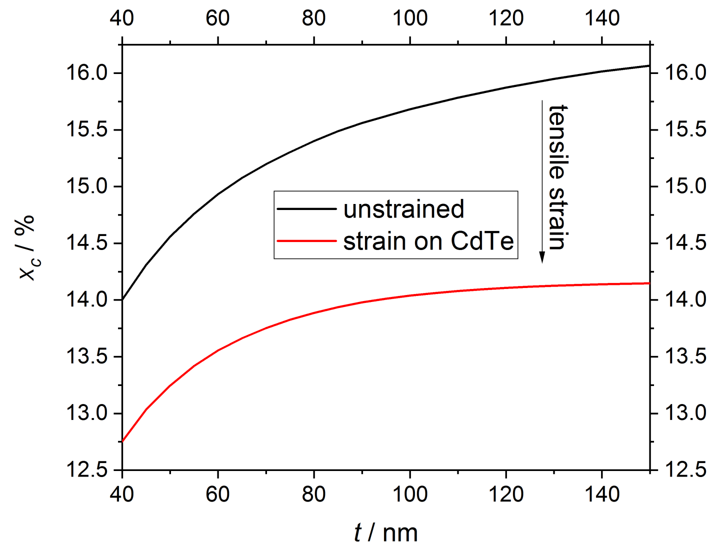

Figure 4.8: Critical concentration of Cd required for achieving a zero gap state in $Hg_{1-x}Cd_xTe$ depending on the layer thicknesses for an unstrained system (black curve) and for strain on a CdTe substrate (red curve).

Despite the fact that the $\Gamma_8^{3/2}$-band shows the expected camel back behaviour the relevant feature for a Dirac semimetal, namely the linear crossing in the bulk band structure, is still present at the Γ-point, even when tensile strain is applied to the layer by the CdTe substrate. However, it is still crucial to account for the change of the value of x_c when applying tensile strain. As already mentioned above, when the $\Gamma_6^{1/2}$-band is approaching the two $\Gamma_8^{1/2}$-band, the two bands are mixing each other. This effect is addressed in Figure 4.9 by applying the RGB colour model to the band characters $\Gamma_6^{1/2}$,$\Gamma_8^{1/2}$ and $\Gamma_8^{3/2}$. A pure $\Gamma_6^{1/2}$ character is shown in red, $\Gamma_8^{1/2}$ in green and $\Gamma_8^{3/2}$ in blue. Any mixture of bands is represented by a colour according to the RGB-value of the different bands present at this point.

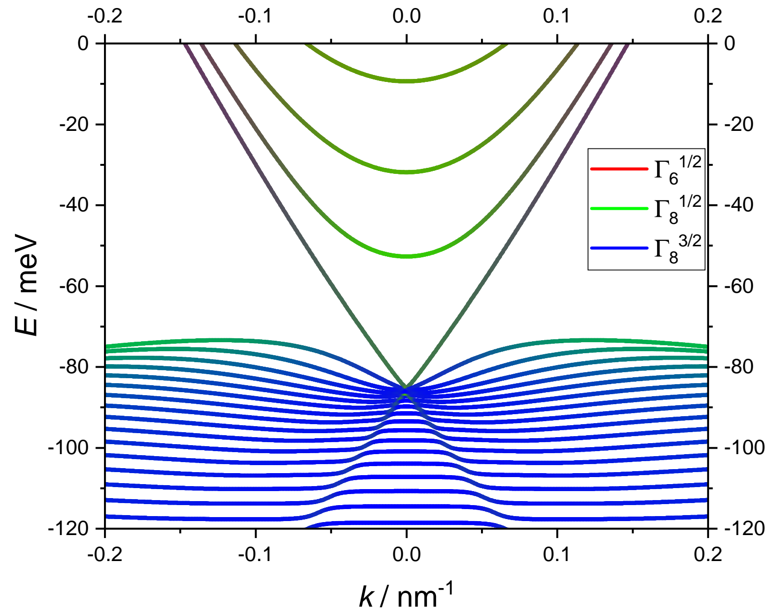

Figure 4.9: Band structure of a 90 nm thick $Hg_{0.86}Cd_{0.14}Te$ layer tensile-strained on a CdTe substrate calculated by $k \cdot p$ theory.

5 CdTe virtual substrate

The strain provided by a CdTe substrate is crucial for growing the topological insulator HgTe. However, commercial CdTe substrates are usually relatively expensive (roughly a factor 100 compared to GaAs) and exhibit a small sample size of 1 cm^2. A possible alternative is to grow a thick CdTe buffer on a different material. The buffer then acts as a virtual substrate (VS), because the crystallographic properties of any layer grown on top are only influenced by the buffer. This was developed by C. Ames [6] for CdTe on a 001 GaAs:Si substrate as a possible replacement for commercial CdTe substrates, which in addition has the advantage of using the conducting GaAs substrate as a backgate for the Hg-containing layer structures. This project was continued by P. Leubner [54] with the possibility of adjusting the lattice constant of the VS by introducing a CdTe/ZnTe superlattice (SL) growth, which added the possibility of engineering the amount of strain acting on the Hg-containing layer. However, the surface roughness on these substrates is significantly higher compared to commercial CdTe. Additionally, higher backgate leakage voltages are demanded for either replacing the topgate or exploit new applications. With this in mind, several changes and additions to the growth process described in [6] were done to eventually further improve CdTe VSs. After a short overview of the state-of-the-art growth process, the first section of this chapter discusses the results for changing growth parameters on GaAs:Si. In the second section the influence of changing the substrate material from GaAs:Si to InAs:S is discussed. Both VS types are then compared with respect to their behaviour in electromagnetic transport, with a focus in charge carrier density and mobility in the third section and their applicability as a backgate in the fourth section.

5.1 CdTe on GaAs

This chapter includes a description of the state-of-the-art process of growing a CdTe VS on GaAs:Si as well as several different approaches for improving the VS in terms of crystal quality and surface morphology.

5.1.1 State-of-the-art

The process for building a CdTe VS on top of GaAs:Si is done in a Hg-free II-VI MBE chamber, which is connected to the Hg-containing chambers by a UHV transfer system (cf. Figure 1.1). In contrast to the CMT-W chamber shown in Figure 1.2, the II-IV chamber has a horizontal and not a vertical build-up, but is very similar in other aspects. It is amongst other materials equipped with a cadmium (Cd), a tellurium (Te), a zinc (Zn) and a selenium (Se) cell.

The growth process of a CdTe VS starts with the thermal removal of a passivation oxide of the GaAs:Si substrate at roughly 650 °C. It is then cooled down in a Zn background pressure to 330 °C, where a small ZnTe layer is grown for 30 s, with a Zn to Te ratio of 1 : 1.2. The ZnTe layer is necessary to reduce the lattice mismatch of CdTe to GaAs, because the size of the mismatch would otherwise cause a change in the growth direction of the CdTe buffer. Migration enhanced epitaxy (MEE) is used to grow the CdTe buffer. This technique is a sequence of MBE steps with an annealing step in between. In this case sequences of 60 s CdTe MBE growth, with a Cd ot Te ratio of 2:1, are separated by a 10 s annealing step in Cd flux. The substrate temperature is sequentially lowered by 10 °C, separating the MEE growth into three parts starting at a growth temperature of 320 °C and ending at 300 °C. During the final cooldown the sample is kept in Cd flux for substrate temperatures above 250 °C. Below 200 °C it can be removed from the sample holder and transferred to another chamber for using it as a VS.

5.1.2 GaAs buffer

As one goal is to achieve a flatter VS surface, this step is introduced to rule out the GaAs substrate as a potential origin for surface roughness of the VSs. A simple thermal treatment of the GaAs:Si is reported to cause etch pit defects related to the evaporation of the most unstable As-oxides. Therefore, in addition to the

growth process discussed above, a GaAs buffer is grown on top of the GaAs:Si substrate after the thermal removal of the passivation oxide. Guillen-Cervantes et al. observed surface pits up to 12 nm in depth and roughly 60 nm in diameter [55]. In a second MBE chamber designated for the growth of III-V materials (Nr. 4 in Figure 1.1) single element Ga and As cells are used for a buffer growth time of usually 30 min at a substrate temperature of 580 °C with a Ga to As ratio of 1:10. In the AFM measurements in Figure 5.1 it can be seen that the resulting GaAs buffer is flat, only showing step sizes of GaAs monolayers, half the size of the GaAs zincblende lattice constant ($a_{\mathrm{GaAs}} = 0.56533$ nm). The RMS on one step is calculated to be 0.097 nm, which is below the resolution of the AFM.

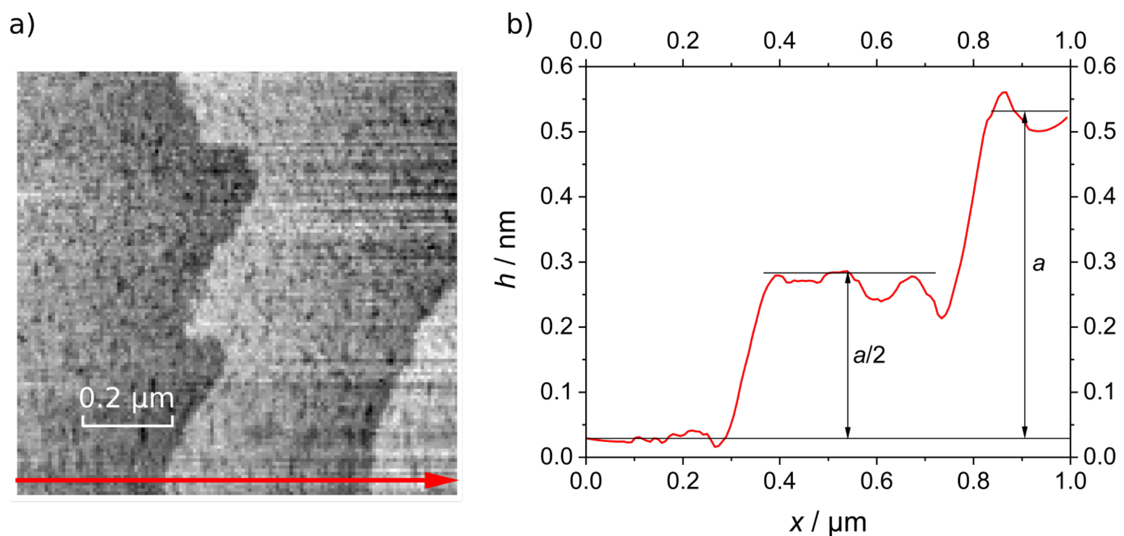

Figure 5.1: AFM measurements of a GaAs buffer on top of a GaAs:Si substrate indicate a flat surface without etch pits observable. a) shows an AFM scan of a GaAs buffer grown on a GaAs:Si substrate. The red arrow indicates the height trace shown in b). The height of the steps matches the monolayer thickness of zincblende GaAs

5.1.3 ZnSe buffer, ZnSe/ZnTe superlattice

The relaxation of the ZnTe layer in the common growth process takes place within the first monolayers of ZnTe due to the large lattice mismatch of $f = 7.38\%$ to GaAs. By adding ZnSe to the growth process one can decouple the relaxation of the grown layer from the III-V/II-VI interface, because the critical thickness for relaxation of ZnSe on GaAs lies at a 100 nm [56]. It can therefore be grown on GaAs without the introduction of additional roughness [57]. ZnSe layers are grown

up to a thickness of 80 nm. XRD measurements have shown no sign of relaxation, and a high quality FWHM of 34” (cf. Figure 5.2).

AFM measurements do not show an observable surface morphology, therefore a flat surface within the resolution of the AFM is assumed. Unfortunately, if this is followed by the state-of-the-art process for a CdTe VS, the decoupling of the relaxation from the III-V/II-VI interface has no significant influence on the surface roughness or the crystal quality. Figure 5.3 shows AFM and XRD measurements which exhibit a similar surface morphology structure as well as an RMS value of 1.7 nm and a FWHM of 180”, which is comparable to a CdTe VS without a ZnSe layer.

On different samples a ZnSe/ZnTe SL is grown, to see if there is an influence on surface morphology and crystal quality when the relaxation process is spread out over a larger thickness. First, a ZnSe/ZnTe SL with 12 growth cycles of 60 s ZnSe to 10 s ZnTe was grown. The resulting SL exhibits a slightly smaller lattice constant than one would initially expect from a 1:6 ratio of ZnSe:ZnTe, which can be explained by substitution of Te atoms by impinging Se atoms [58, 59]. The resulting layer thickness was determined by HRXRD to be 43 nm and it is still pseudomorphic on the substrate (cf. Figure 5.4). It shows a RMS of 0.2 nm with a FWHM of 21”. Second, the amount of growth cycles was increased to 56, aiming at a layer thickness of 200 nm. HRXRD shows that the SL is at least partially relaxed, which is expected at this thickness. The surface roughness measured by AFM, however, increased drastically compared to the fully pseudomorphic layer to 1.2 nm, which is already comparable to the RMS value of the final CdTe buffer (c.f Figure 5.5).

While the introduction of ZnSe did not lead to an immediate improvement concerning the surface morphology of the CdTe VS, there is also no negative effect observable. Considering its high band gap of 2.720 eV [60], this makes ZnSe layers a possible candidate for improving the insulating properties of the VS between the GaAs:Si substrate and the Hg-containing conducting layer on top, allowing for a back gating of the conducting layer. Measurements of the backgate stability are shown and discussed in chapter 5.4.

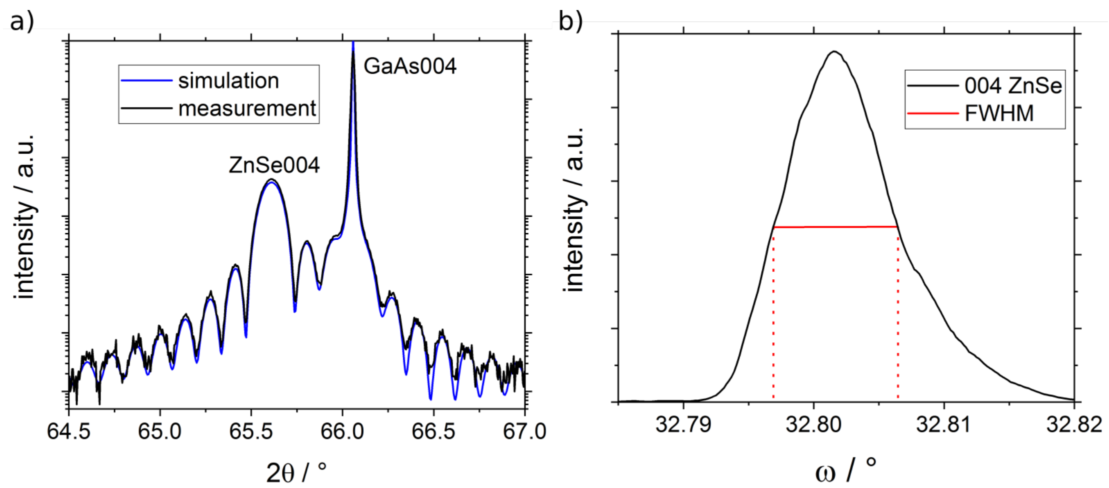

Figure 5.2: HRXRD 2θ and ω-scan of the 004 reflex of a ZnSe layer on top of GaAs. a) 2θω scan showing a layer thickness of 80 nm. Kiessig fringes verify a pseudomorphic grow of the ZnSe b) ω scan of the 004 reflex of the ZnSe layer exhibits a FWHM of 34".

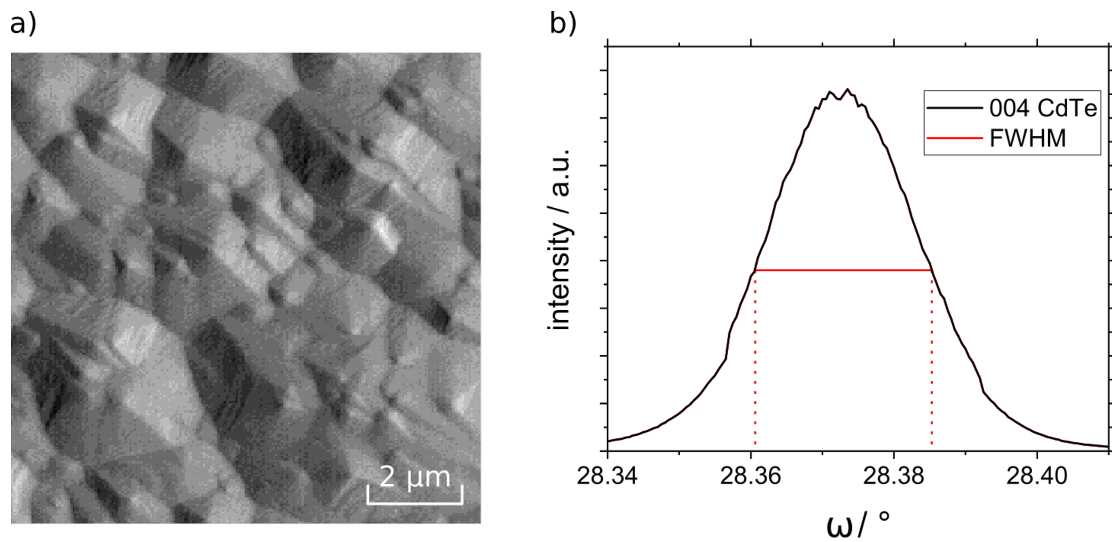

Figure 5.3: AFM and HRXRD measurements of a CdTe VS, with 100 nm of ZnSe on top of the GaAs substrate. a) AFM exhibits a surface roughness of 1.7 nm b) ω scan of the 004 reflex of CdTe layer exhibits a FWHM of 180".

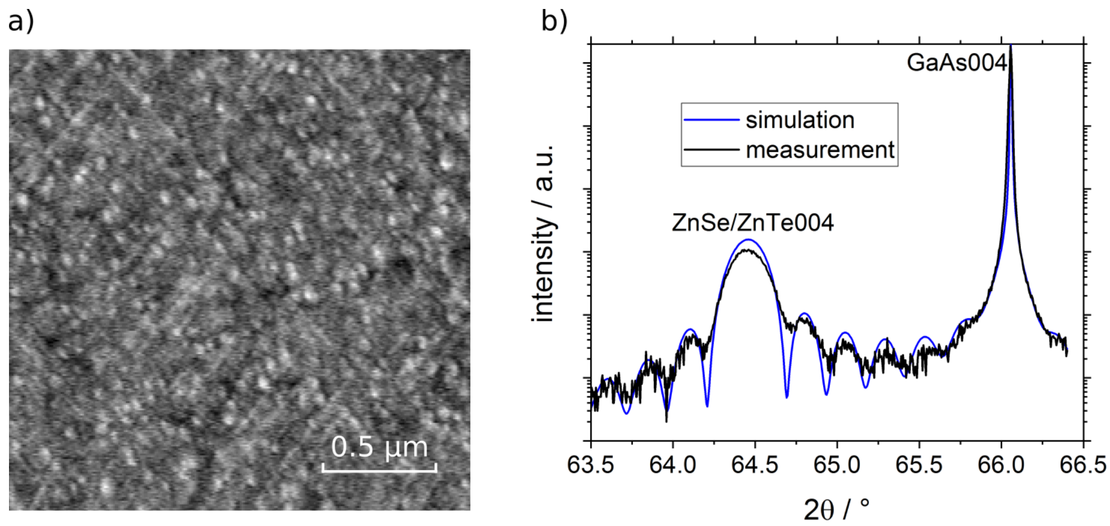

Figure 5.4: AFM and HRXRD measurements of a ZnSe/ZnTe SL on top of the GaAs substrate. a) AFM does not show an explicit surface morphology. RMS is calculated to 0.2 nm. b) $2\theta\omega$ scan of the 004 reflex shows a layer thickness of 43 nm. Kiessig fringes verify a pseudomorphic grow.

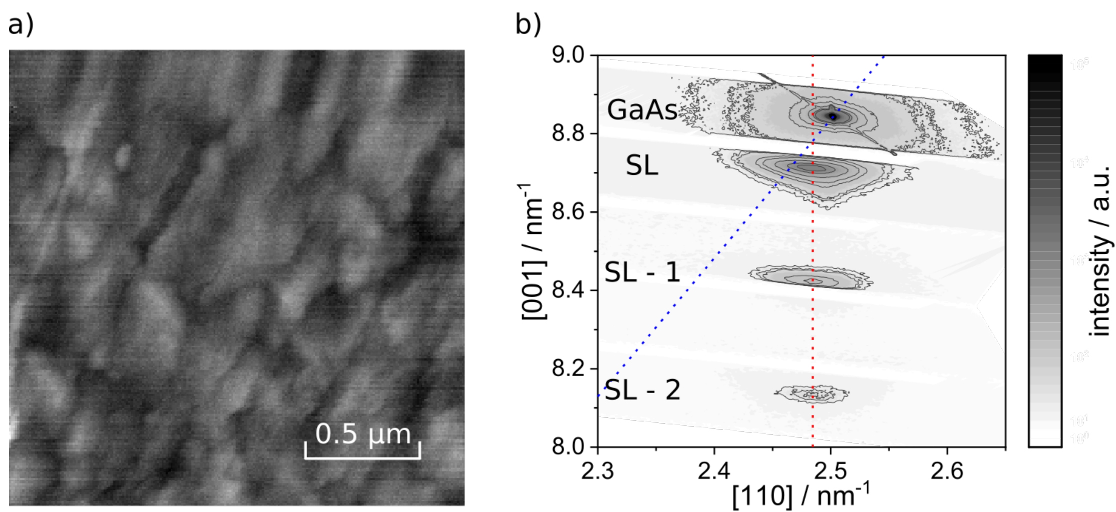

Figure 5.5: a) AFM scan of a partially relaxed ZnSe/ZnTe SL. RMS is calculated to 1.2 nm. b) Reciprocal space map of the main peak of the ZnSe/ZnTe SL and its first and second satellite peak with respect to the GaAs substrate peak, indicating a partial relaxation of the SL.

5.1.4 Annealing CdTe

The MEE growth technique introduced in [6] already utilizes the concept of annealing for CdTe VS. By increasing the temperature and offering only a single element the impinging atoms can migrate into the crystal lattice and possibly reduce the dislocation density, while no additional growth takes place because the growth temperature for single element crystals in these materials is usually much lower. With this in mind an annealing step was added at the end of the CdTe growth process, where the sample is heated up again in Cd flux. Three different CdTe VS, without additional annealing, with 10 min at 350 °C and for 120 min at 340 °C, were compared by RHEED, HRXRD and AFM. Concerning the surface reconstruction, RHEED observations did not show any deviation from the (2x1)-c(2x2) pattern, which is expected for a Cd rich surface in CdTe. Also HRXRD measurements showed no influence on the crystal quality of the CdTe buffer by the additional annealing step. Concerning the surface morphology, Figure 5.6 shows a comparison of the AFM measurements of the three samples. A broadening of the hills and valleys on the surface of annealed samples can be observed, while the horizontal hill-to-valley distance increases. This is also why the total RMS value did not change significantly. The annealed samples, however, show a smaller density of 0.1 nm sized defects. So an additional annealing step can be used as a smoothing tool for CdTe surfaces, especially for small structures, which size now could potentially be below the hill-to-valley distance.

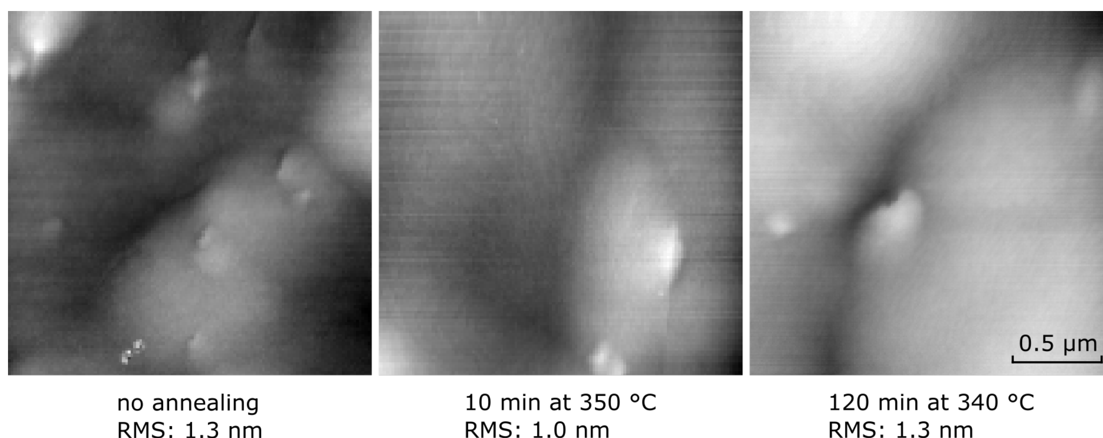

Figure 5.6: AFM scans to show the influence of an additional annealing step after growth on the surface morphology. No annealing shows a larger number of defects compared to the annealed samples. Furthermore, annealing increases hill-to-valley distances both vertically and horizontally. (same scale for all images)

5.1.5 CdTe ALE finish

Another method for a post growth surface treatment is the addition of a CdTe layer grown by Atomic layer epitaxy (ALE). This growth technique differs from MBE in the fact that the single element materials are not provided simultaneously, but only one material at a time, which is achieved by alternately closing and opening of the cell shutters. Specifically, the shutter sequence for the CdTe layers grown by ALE discussed here is 4 s / 0.5 s break / 4 s Te / 0.5 s break. The substrate temperature for ALE growth is lower compared to MBE growth to take care of the increased desorption rate by applying single elements, which exhibit a higher vapour pressure than compounds. Three different substrate temperatures for ALE growth of 230 °C, 240 °C and 250 °C were investigated. Again, there was no significant difference between the samples visible in the HRXRD and RHEED measurements, which leaves the AFM as analysis tool. The AFM pictures are shown in Figure 5.7 a) to c). The best result, both in terms of small sized surface defects as well as surface roughness, is achieved for a growth temperature of 240 °C (cf. Figure 5.7 b)). Hence, at this temperature the growth time was increased from 200 to 600 cycles, to investigate the influence of the thickness of the ALE layer on the surface morphology. AFM data is shown in Figure 5.7 d). The surface morphology decreased significantly in quality as both RMS value and defect density increased again.
So a thin ALE layer at the end of the VS growth provides a surface smoothing effect similar to the previously discussed Cd annealing. However, even the best results are still inferior to commercial substrates, therefore these processes are not investigated further.

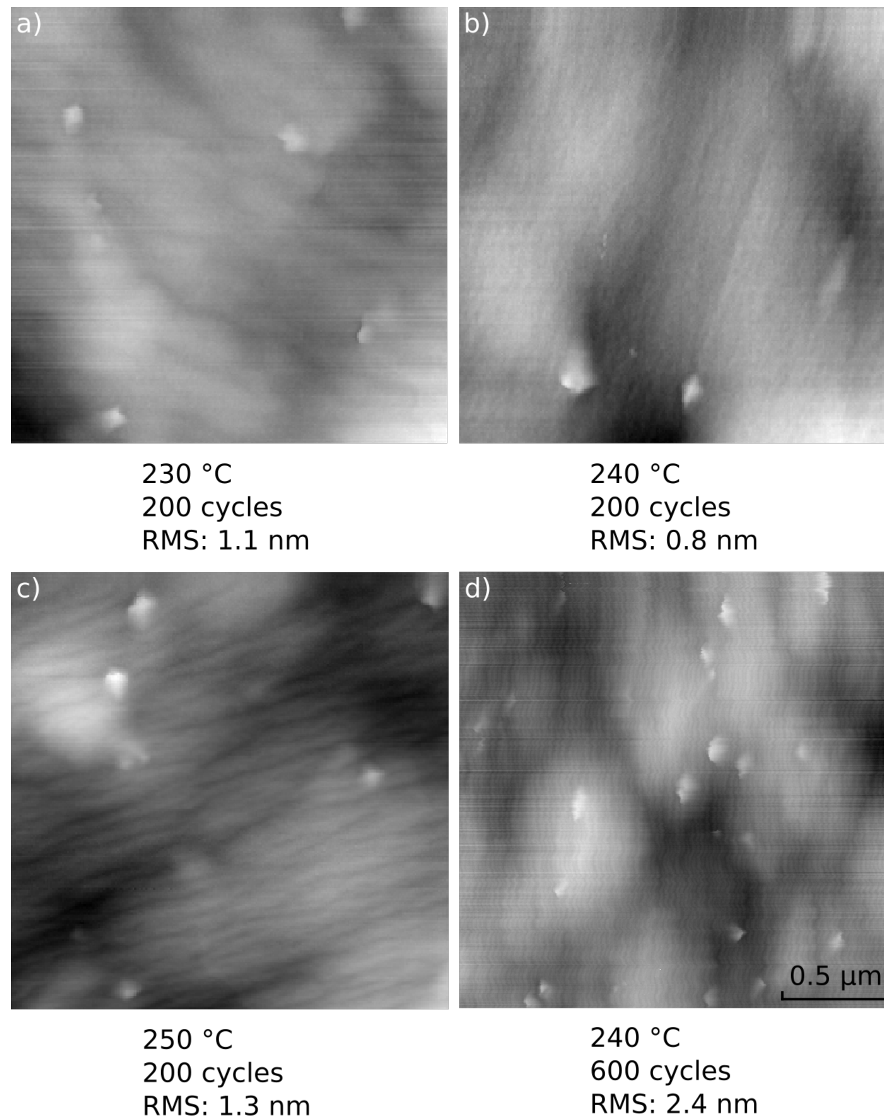

Figure 5.7: AFM scans for ALE-grown CdTe layers on top of MBE-grown CdTe VS for different growth temperatures and layer thickness. A minimum in growth defects and RMS value could be found for 200 ALE cycles at 240 °C. (same scale for all images)

5.1.6 Increased CdTe buffer thickness

The usual thickness of the CdTe buffer is 4 μm, which is a sweet spot between growing time, crystal quality and back gate efficiency. In the framework of the substrate development the CdTe buffer thickness is increased to 12 μm. The thickness value was chosen as a compromise between maximum layer thickness and MBE chamber occupation time. While thinner CdTe buffer layers offer a lower surface roughness, the increase in FWHM with decreasing buffer thickness also causes a decrease in the charge carrier mobility of HgTe QW grown on top as shown in [6]. Before the results are discussed it is worth mentioning that this kind of VS is rather impractical for every day use, because the growth time increases by a factor of 3 as well as the required cell material. This would result in only 10 to 15 substrates before the cells would have to be refilled. Nevertheless, the AFM measurements show a great improvement of the surface morphology compared to a 4 μm sample as shown in Figure 5.8. While the RMS value does not change significantly over a large area, the lateral hill-to-valley distance increased from $1-2$ μm to $3-6$ μm. This leads to a great reduction of the surface roughness for small structures (e.g. micro Hallbars) which fit entirely on a hill or in a valley. In an area size of 2x2 μm for example the RMS value goes down to 0.4 nm. So for the purpose of small structures this is a great improvement of the surface morphology. However, one has to ponder the larger wafer size of 2" diameter compared to the

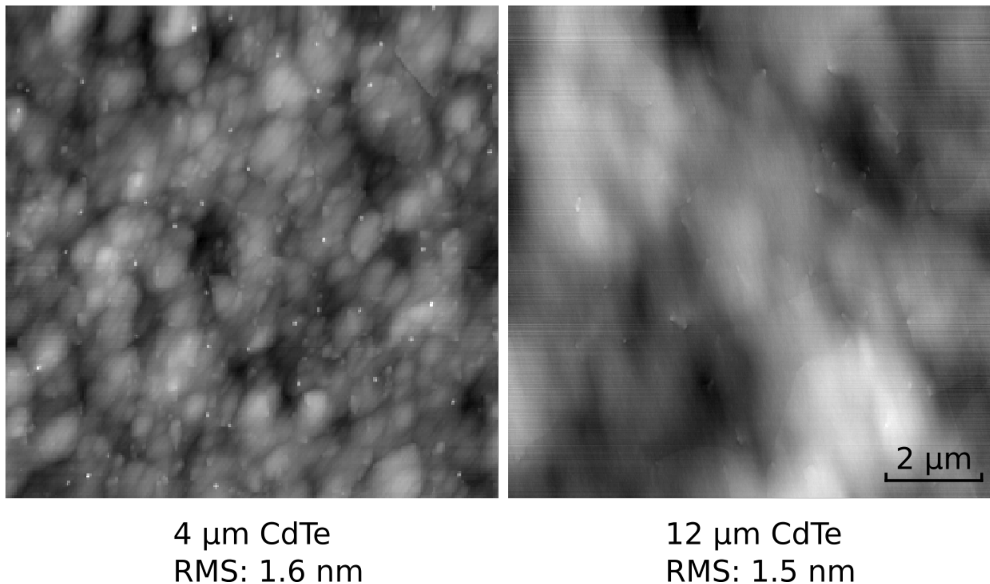

Figure 5.8: AFM scans for comparison of the surface morphology of a 4 μm (left picture) and a 12 μm (right picture) thick CdTe buffer. (same scale for all images)

1 cm^2 on a commercial CdTe substrate against the high cell material cost for one sample. The applicability of the GaAs:Si substrate as a backgate, precisely if the lower gate action of the thicker CdTe buffer is equalized by higher breakthrough voltages, still needs to be verified.

5.2 CdTe on InAs

While the project of building a CdTe VS initially used GaAs:Si as substrate, basically any material which allows for a 001 zincblende growth of CdTe can be used. Since the lattice mismatch of GaAs and CdTe is relatively large ($f = 15\%$), a nice candidate for replacing GaAs is InAs, which shares the zincblende crystal structure, but has a lattice constant closer to CdTe with a lattice mismatch of only 7%. Therefore, there is no additional relaxation step needed to overcome the lattice mismatch from substrate to CdTe buffer layer. When doped with sulphur (InAs:S) it can also be used as a backgate.

5.2.1 InAs substrate preparation

Before the 001 InAs:S substrates can be used for overgrowth with a different material, a passivation oxide has to be removed. This is done thermally in an arsenic atmosphere at around 530 °C for 3 min. After the oxide desorption the substrate is cooled down to 480 °C and an InAs buffer is grown to ensure a clean in situ surface and to reduce the amount of thermally induced defects. We use a flux ratio of 1:10 In:As for 12 min, which results in a buffer thickness of 100 nm to 200 nm. Figure 5.9 shows the different RHEED pattern during the oxide desorption and the buffer growth. Picture a) shows the untreated substrate. The passivation oxide is amorphous and therefore no RHEED pattern is observable. With the beginning of the desorption b) one observes a spotty reflection pattern which is typical for a rough, three dimensional surface. The reconstruction shown in c) marks the end of the desorption process, where the line shaping indicates a flat surface. While the expected twofold periodicity in (1-10) direction was barely visible, the fourfold periodicity matches the expected 4×2 reconstruction [61]. This shape is slightly vanishing during the cooling towards the buffer growth temperature d). Also the angular orientation changes from a 4×2 to a 2×4 reconstruction, which was already observed by Ye et al. [61]. The RHEED pattern of the finished InAs buffer

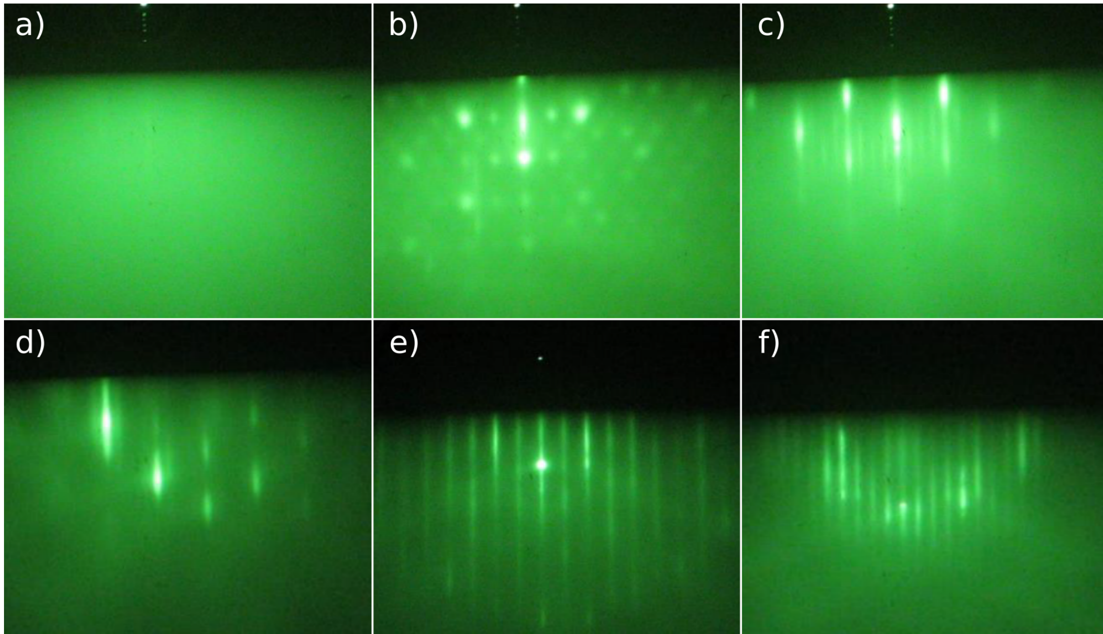

Figure 5.9: Pictures of the RHEED fluorescent screen showing a) the untreated substrate, b) the spotty pattern at the beginning and c) sharp lines at the end of the desorption process. d) shows the RHEED pattern after cooling down to the buffer growth temperature. e) and f) show the twofold and fourfold periodicity of the finished buffer respectively.

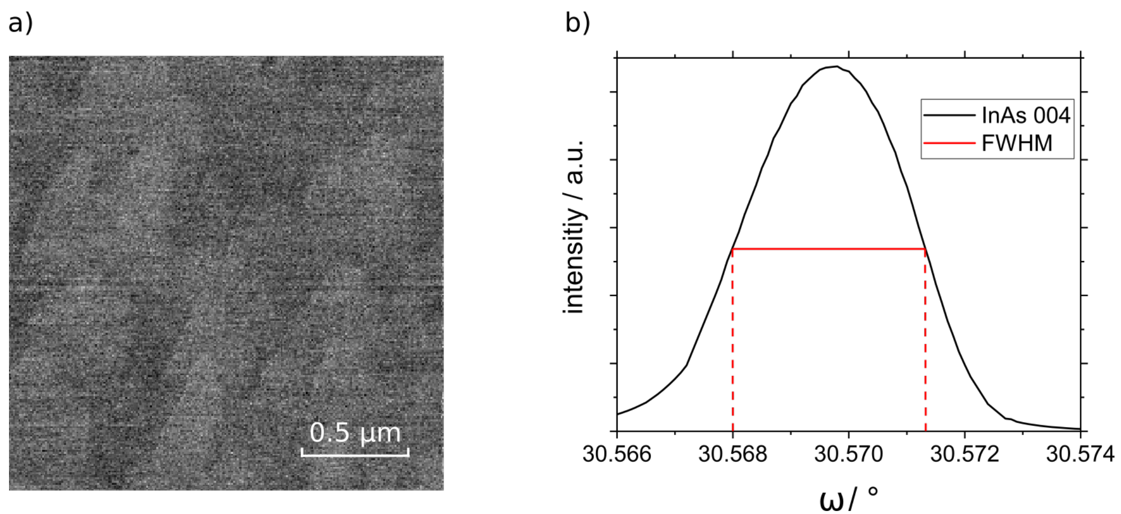

Figure 5.10: a) AFM scan of the InAs buffer layer on an InAs substrate exhibiting a flat surface. b) HRXRD ω scan shows a FWHM below the resolution of the instrument.

is shown in Figure 5.9 e) and f). Here, both the twofold e) and fourfold f) periodicity are visible and stay visible after cooling down the sample for transfer. AFM and HRXRD measurements show a RMS value of 0.2 nm and a FWHM of 12” (cf. Figure 5.10). Both values are determined by the resolution of the instruments, confirming a flat, high quality InAs surface.

5.2.2 ZnTe buffer on InAs

As already mentioned, in contrast to ZnTe grown on GaAs the lattice mismatch between InAs and ZnTe is small enough ($f = 0.75\%$) for growing a pseudomorphic ZnTe layer. Hence, the relaxation process of the succeeding CdTe can be separated from the change in electron configuration when growing from a II-VI buffer (ZnTe,CdTe) on a III-V material (InAs,GaAs). On the ZnTe buffer, oval growth defects are observed in the optical microscope shown in Figure 5.11 c). Their density could be reduced drastically by closing the As cell earlier during the final cooldown of the InAs buffer growth described in the previous chapter, shown in Figure 5.11 a) for the beginning and in Figure 5.11 b) for the end of the development. Based on that observation a possible explanation is a surplus of As accumulated during the cooldown. Final samples had a defect density of less then

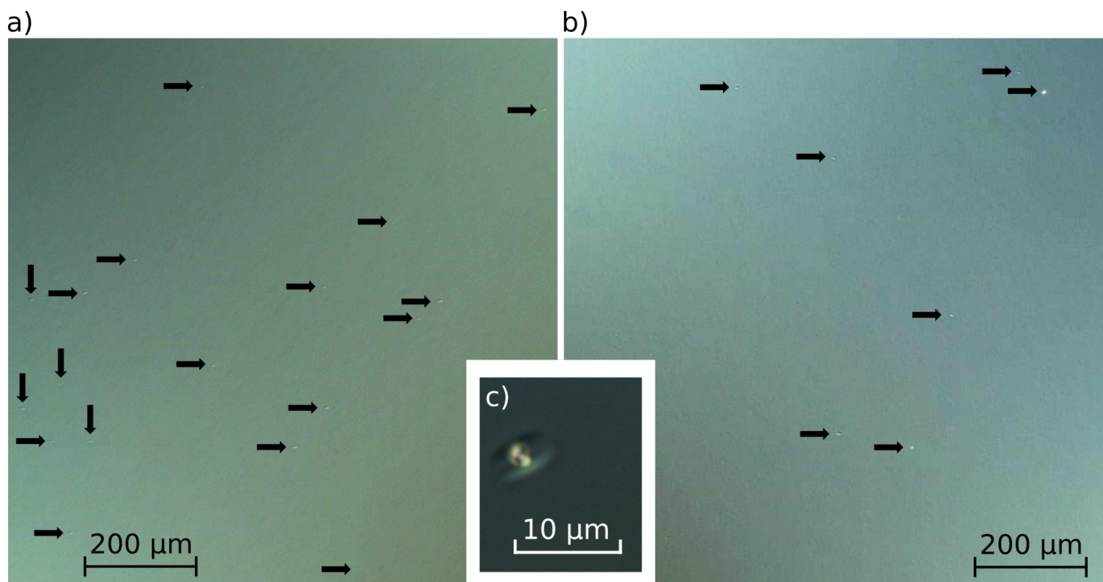

Figure 5.11: Pictures of oval growth defects originating from the ZnTe growth on InAs, taken with the Nomarski optical microscope. a) and b) show the defect density in a 1×1 mm^2 area at the beginning and the end of the development respectively. c) shows a close up image of one defect.

1 per 0.5 mm^2. AFM and XRD data are shown in Figure 5.12. The $2\theta\omega$-scan of the HRXRD measurements confirms a completely pseudomorphic, 32.5 nm thick ZnTe layer. The RMS value calculated from AFM does not show any increase in roughness compared to the bare InAs substrate. This guarantees a flat, high quality starting point for the upcoming CdTe VS growth, with a remaining lattice mismatch of only 7% compared to the 15% by using GaAs.

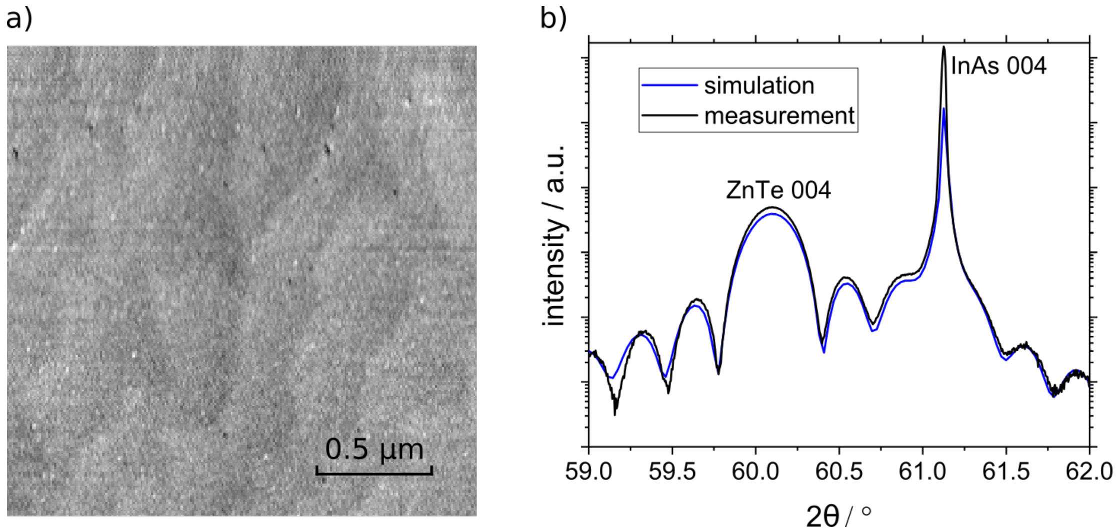

Figure 5.12: a) AFM scan of the ZnTe buffer layer on an InAs substrate exhibiting a flat surface. b) Comparison of the HRXRD $2\theta - \omega$ scan around the 004 reflex of ZnTe and InAs with the simulation confirming a pseudomorphic ZnTe layer.

5.2.3 CdTe buffer on InAs

After the ZnTe buffer the sample is ready to finally grow a CdTe buffer for obtaining a VS. Therefore, the same MEE process described in section 5.1.1 for the gowth of a 4 µm CdTe layer is applied. The CdTe is fully relaxed and exhibits a FWHM of 197", while AFM measurements show a RMS value of 1.4 nm (cf. Figure 5.13). Both numbers are comparable to other CdTe VS grown on GaAs. A rougher surface morphology compared to the non-relaxed layers is also visible in the Nomarski optical microscope (cf. Figure 5.14). Additionally, there are lines oriented along the (110) direction visible in Nomarski mode as shown in Figure 5.13 a), which suggest a preferred direction of the CdTe misfit dislocations. These results show that, at least from a crystallographic point of view, CdTe VS on InAs:S are of

comparable quality as on GaAs:Si. Unfortunately, the surface roughness is, similar to the ZnSe/ZnTe SL discussed in section 5.1.3, determined by the existence of a relaxation process and not by the amount of mismatch between the two participating layers.

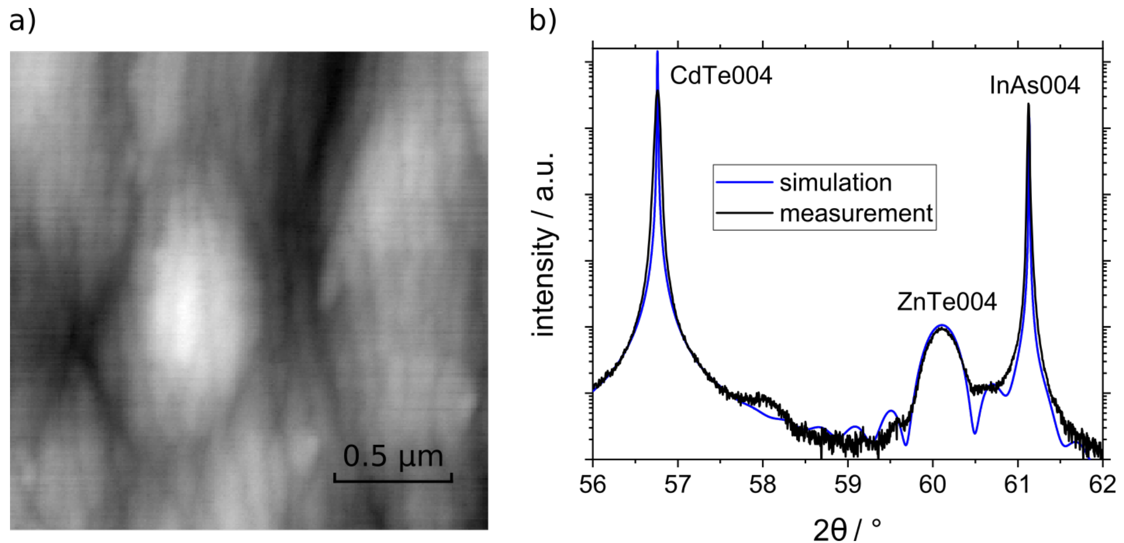

Figure 5.13: a) AFM scan of the CdTe buffer layer on an InAs substrate. b) HRXRD $2\theta-\omega$ scan of the 004 reflexes shows the relaxed CdTe buffer.

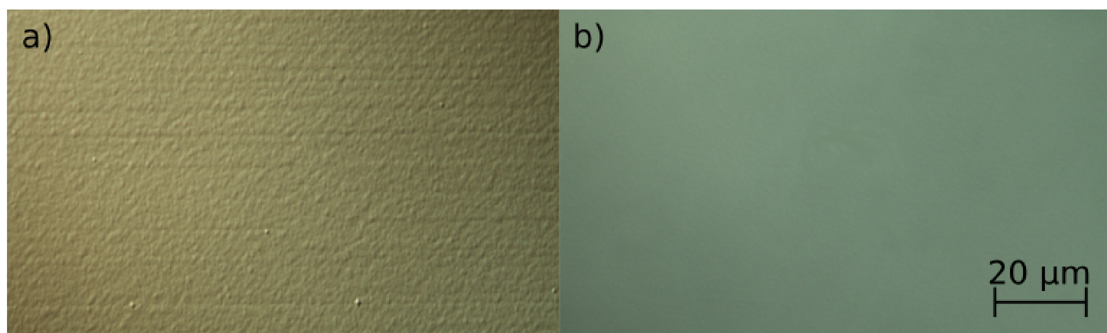

Figure 5.14: Optical microscopy in Nomarski mode of a CdTe VS on InAs (a), showing an increased surface roughness after relaxation with addition of horizontal lines along the 110 direction. b) shows the surface of an InAs buffer before overgrowth as comparison. (same scale in all images)

5.3 Virtual substrates: transport characterization

As shown in the previous section, both approaches for building a VS are possible candidates for using them as basis for the growth of $Hg_{1-x}Cd_xTe$ structures. Therefore, an important aspect to investigate, despite the crystallographic quality, is the substrate type related influence on the transport properties of Hg-containing layers. As the current interest lies on transport in $Hg_{1-x}Cd_xTe$, several HgTe quantum wells (QW) with $Hg_{0.3}Cd_{0.7}Te$ barriers have been grown and their charge carrier density n and mobility μ are used as characterization values. From all these samples Hallbar structures are built as described in chapter 3. An overview of the samples is given in Table 5.1. If not otherwise mentioned all measurements refer to the bHb structure of the respective sample. $Q2941_{\parallel}$ and $Q2941_{\perp}$ refer to a parallel or perpendicular orientation of the Hallbar's current path (from contacts 1 to 6) with respect to the lines along the 110 direction visible on the Nomarski pictures on InAs-based samples (cf. Figure 5.14). This is to investigate if there is any influence of the orientation on the basic transport properties. All samples feature a top gate and, with the exception of $Q2941_{\perp}$, an ohmic contact to the substrate, which allows to use it as a back gate. For characterization purposes the gate dependent sheet resistance R_{xx} was measured at zero and at a finite magnetic field (in this case $B = 0.3$ T). From these gatesweeps one can calculate the gate voltage dependence of n and μ, as shown in chapter 3.2. Exemplary graphs are shown in Figure 5.15 for sample the $Q2941_{\perp}$. An overview of gatesweeps and gate voltage dependence of n and μ for all samples is shown in Appendix A. The gatesweep in Figure 5.15 a) shows a sharp transition from electron to hole transport at around $V_{TG} = -0.7$ V. Additional sweeps in the opposite direction (not shown) do not

Sample nr.	substrate type	d_{LB} / nm	d_{QW} / nm	d_{UB} / nm
Q2940	CdTe on GaAs	56	10.4	57
$Q2941_{\parallel}$	CdTe on InAs	55	10.0	56
$Q2941_{\perp}$	CdTe on InAs	55	10.0	56
Q2944	CdTe on ZnSe/ZnTe on GaAs	55	9.9	50
Q2950	CdTe on InAs	110	11	110

Table 5.1: Overview of the manufactured and characterized Hallbar samples for comparison of the different VS on the electrical transport properties. d refers to the thickness of lower barrier (LB), quantum well (QW), and upper barrier (UB) respectively.

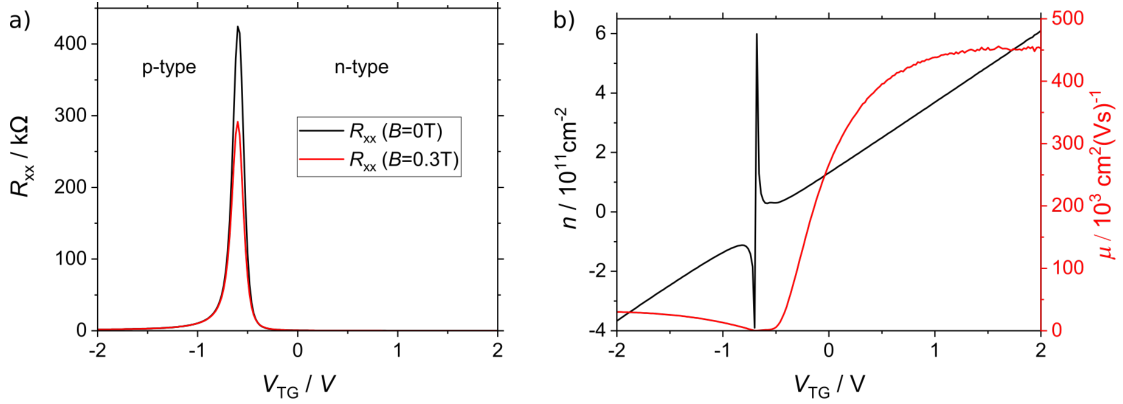

Figure 5.15: a) V_g dependence of R_xx for $B = 0$ T (black) and $B = 0$ T (red). b) V_g dependence of n and μ.

show any resistance hysteresis. The gate dependent mobility increases, the more V_TG differs from the charge neutrality point at $V_\mathrm{TG} = -0.7$ V, as more and more charge carriers are involved, which screen scattering causing impurities. Around $V_\mathrm{TG} = 1$ V and higher, μ saturates in the electron regime, which is caused by an increased backscattering possibility of Dirac fermions with increasing charge carrier density [62]. In the hole regime the mobility is significantly lower, due to the increased effective mass of the valence band in HgTe.

To compare the mobility behaviour of the different samples, Figure 5.16 shows μ in direct dependence on the charge carrier density of each sample, which is obtained from the correlation of n and μ shown in Figure 5.15 b) and is eliminating different gate influences on the individual sample. One can see that the general behaviour of μ with respect to n is similar for all samples, regardless if the VS is based on GaAs, with or without ZnTe/ZnSe SL, or on InAs. The highest possible mobility accessible was achieved on the sample $Q2941_\perp$ (QW on InAs with the Hallbar aligned perpendicular to the stripes discussed in Figure 5.14), which seems to stand out compared to the other samples. However, without more statistics these deviations could still be explained with the usual fluctuations from sample to sample for these kinds of QW. An overview of magnetic field dependent measurements around a charge carrier density of $2.5 \cdot 10^{11}$ cm^2 is shown in Figure 5.17 for the samples listed in Table 5.1.

All samples show a very similar behaviour matching the expectations for the QHE and SdH-oscillations. Only sample Q2944 (ZnSe/ZnTe SL; cf. Figure 5.17 e)) shows deviations in the form that the resistance plateaus deviate slightly from the expected value and the minima of SdH oscillations do not go to zero for higher

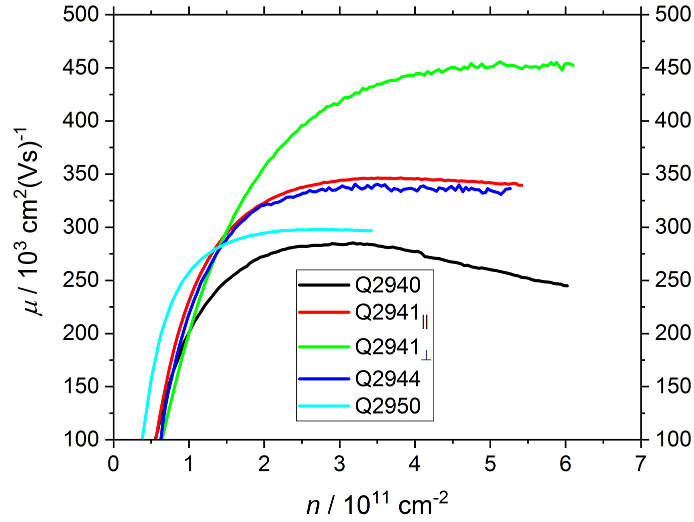

Figure 5.16: Relation between electron density n and mobility μ for HgTe quantum wells of comparable thickness grown on different types of CdTe VS.

magnetic fields. However, the measurements of a smaller sized Hallbar of the same material (cf. Figure 5.17 f)), which usually show a lower quality in transport as discussed in [63], match the expected behaviour, which suggests that the deviations in Figure 5.17 e) are caused by some damage during the lithography process. This supports the argument that the ZnSe/ZnTe SL does not influence the transport quality negatively.

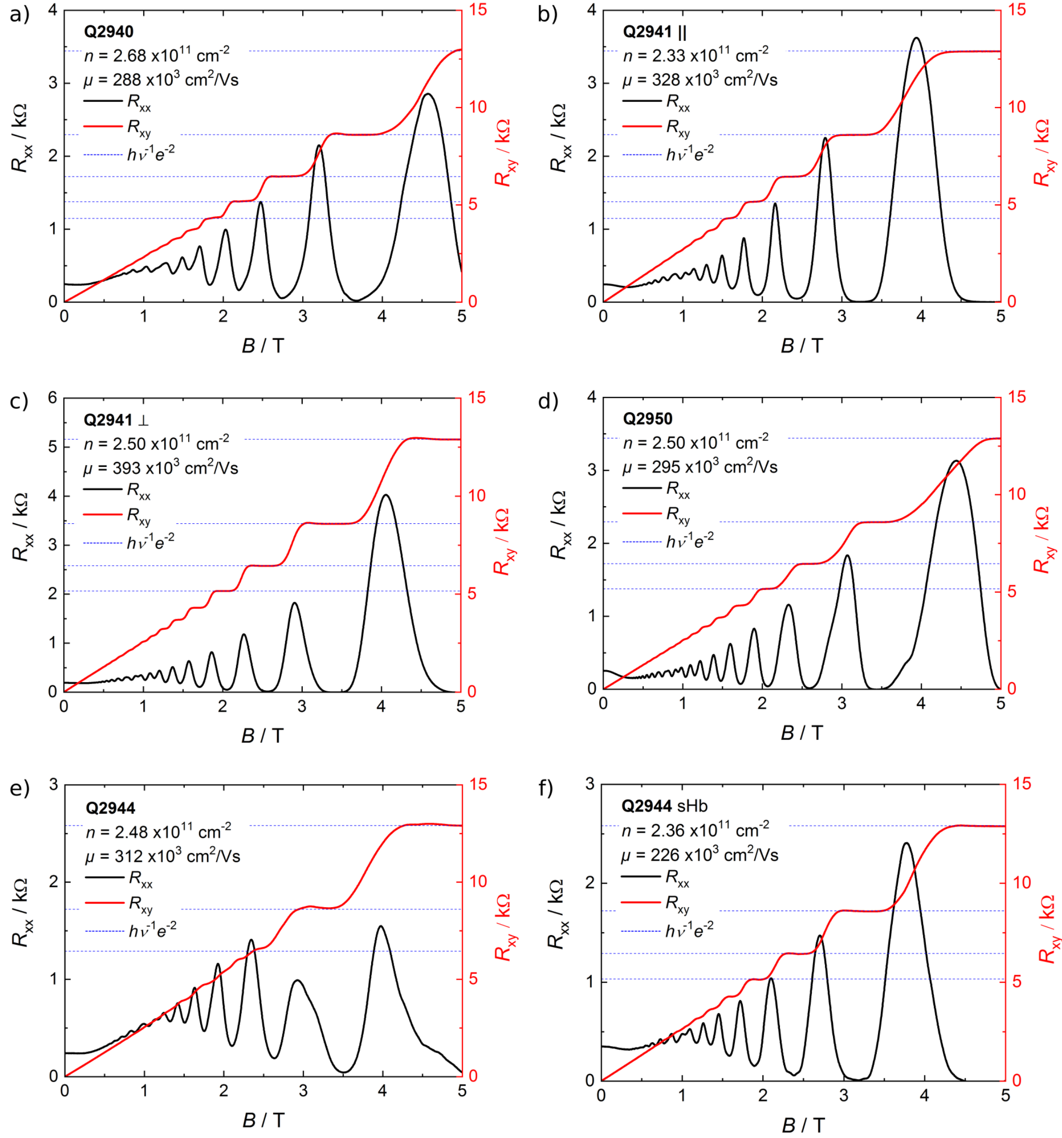

Figure 5.17: Measurements of R_{xx} and R_{xy} dependent on the size of a magnetic field perpendicular to the quantum well for the big Hallbars of the samples Q2940, Q2941$_{\parallel}$, Q2941$_{\perp}$, Q2944, Q2950 and a small Hallbar (sHb) on the sample Q2944.

5.4 Virtual substrates: back gates

As already mentioned above, one main advantage of these VS is the possibility to use the conducting substrate as a back gate. At first the gate action of the back gates is addressed, which describes the change of charge carrier density per gate voltage. From the linear change in n in the electron regime shown in Figure 5.18 a) the gate action of the TG arises to $2.13 \cdot 10^{11}$ cm^{-2}V^{-1}, while the BG gate action is $1.36 \cdot 10^{10}$ cm^{-2}V^{-1}. This is due to the increased distance between the BG and the conducting layer compared to the TG. So $V_{\mathrm{TG}} = 1$ V is equivalent to $V_{\mathrm{BG}} = 15.6$ V. The BG-axis in Figure 5.18 b) is adjusted with this factor in respect to the TG-axis, where the behaviour of the gate dependent R_{xx} of the HgTe layer does not show a significant difference, regardless if it is influenced by TG or BG.

However, using a BG often brings up the problem that the total range of n accessible compared to a TG is smaller, because the higher voltages required for the BG due to the decreased gate action are limited by gate leakages through the VS buffer layer. The following discusses the different voltages at which these breakthroughs occur for the three approaches of building a CdTe VS discussed earlier. For the state-of-the-art growth process of VS for HgTe QW on GaAs discussed at the beginning of this chapter there are several samples with gate leakages already characterized (cf. Table 5.2). These values show that, while negative gate voltages

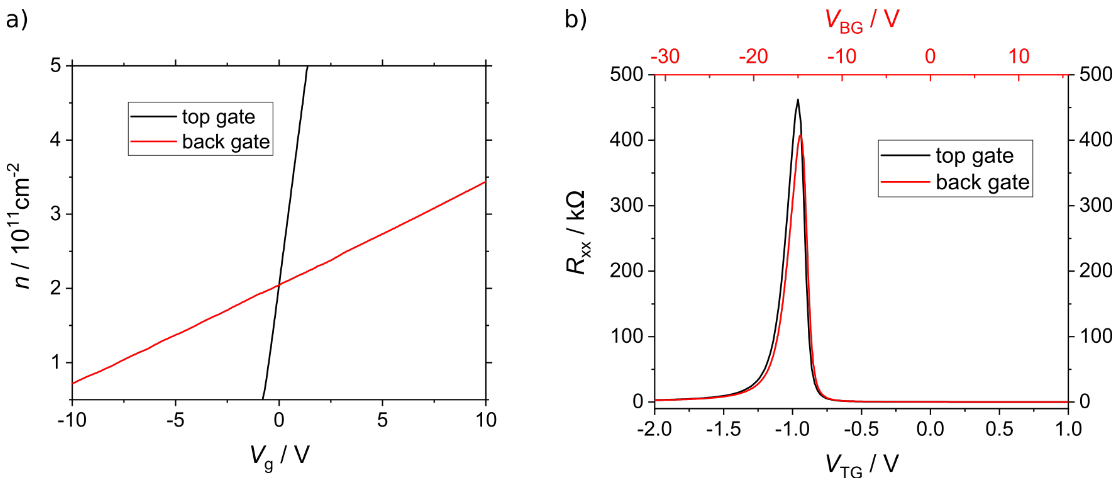

Figure 5.18: a) Comparison of the change in charge carrier density n between the applied gate voltage of top gate V_{TG} and back gate V_{BG}. b) Comparison of the change in the longitudinal sheet resistance R_{xx} between the applied gate voltage of top gate V_{TG} and back gate V_{BG}.

up to −30 V are possible, no sample grown with the state-of-the-art growth process exceed +8 V for positive gate voltages so far. Switching to a VS based on InAs/ZnTe (see chapter 5.2) shows similar minimal and maximal values for V_{BG}. The sample with the ZnSe/ZnTe superlattice on GaAs shows an applicable range for V_{BG} from −40.1 V to 28.8 V, which is a significant increase, especially in the region of positive gate voltages. A possible explanation for this is the increased band gap of a ZnSe/ZnTe superlattice compared to single ZnSe, ZnTe or CdTe layers as described in [64]. This leaves the stack of CdTe - ZnSe/ZnTe SL on a GaAs substrate as the most promising approach for back gating of a CdTe VS.

Sample nr.	substrate type	$V_{\mathrm{BG,min}}$ / V	$V_{\mathrm{BG,max}}$ / V
Q2745 a	CdTe on GaAs	-22	8
Q2745 b	CdTe on GaAs	-1	4
Q2746 a	CdTe on GaAs	-10	8
Q2746 b	CdTe on GaAs	-30	8
Q2746 c	CdTe on GaAs	-15	not tested
Q2940	CdTe on GaAs	-1.5	3
$Q2941_{\parallel}$	CdTe on InAs	not tested	not tested
$Q2941_{\perp}$	CdTe on InAs	-20	2.5
Q2944	CdTe on ZnSe/ZnTe on GaAs	-40.1	28.8
Q2950	CdTe on InAs	-30.9	3

Table 5.2: Overview of the minimum and maximum backgate voltages applicable before current leakage occurs for HgTe QW on different VS.

6 Zero gap $Hg_{1-x}Cd_xTe$

This chapter discusses physical process of tuning the band gap of $Hg_{1-x}Cd_xTe$ by changing the Cd concentration x. This gives access to three topological phases in $Hg_{1-x}Cd_xTe$. There is a non-inverted band structure in CdTe, representing a semiconductor and an inverted band structure in HgTe representing a topological insulator. In between these two there exists a zero gap state at a critical concentration x_c, where the touching of valence and conduction band forms a linear dispersion in the bulk band structure, representing a third topological state, a so called Dirac semimetal. After an overview of the sample fabrication process, the focus lies on magneto electrical transport measurements, which take advantage of the chiral anomaly present in $Hg_{1-x_c}Cd_{x_c}Te$ as a characterization tool for this specific topological phase. In addition, the existence of surface states is investigated based on the electrical transport properties in an out-of-plane magnetic field.

6.1 Sample fabrication

A full growth cycle for one of these samples proceeds as follows. The commercial CdTe substrates arrive covered with a protection oxide of around 1.5 nm, calculated from XPS measurements in [6], which has to be removed prior to the MBE growth process. Thermal desorption, the most simple in-situ method, is not applicable for CdTe substrates, because the required desorption temperatures already cause severe damage of the substrates surface due to evaporation of Cd. Instead the oxide is removed ex-situ with chemical etching in a solution of 1 : 3 HCl : H_20. Afterwards, the sample is glued on a molybdenum block with liquid gallium (Ga) and is transferred into the UHV system. This has to be done quickly to avoid reoxidization. Usually the samples are exposed to air after etching for less than 10 min. In the UHV system the sample is heated up to 200 °C for 15 min. The temperature at this step is low enough to avoid any desorption of CdTe and is mostly done to evaporate water before entering the MBE growth chamber.

The material provided by the four different effusion cells used during a full growth cycle is a CdTe compound and single elements of Cd, Te and Hg. During one growth cycle all cells are kept at constant temperature, therefore providing constant material flux. For growing $Hg_{1-x}Cd_xTe$ layers in various compositions only the flux of the single element Cd cell is changed from sample to sample. The structure of the layer stack is then controlled by opening the shutter of each cell accordingly.

A typical growth cycle has already been described in Figure 1.5. The only variation to this is during the Hg-containing layer growth. The $Hg_{1-x}Cd_xTe$ around $x = x_c$ are grown by additionally opening the single element cells of Te and Cd. Using the CdTe compound cell instead produces $Hg_{0.3}Cd_{0.7}Te$, which is a composition far away from the transition point in the semiconductor regime and can therefore be used as an insulating capping layer to protect the $Hg_{1-x}Cd_xTe$ of interest from oxidization. It can also be used as an additional buffer layer on the CdTe substrate. It was shown that such a buffer layer can strongly improve the transport properties of HgTe layers [6]. However, in the case of a stack of $Hg_{0.3}Cd_{0.7}Te/Hg_{1-x}Cd_xTe/Hg_{0.3}Cd_{0.7}Te$ the evaluation of x from the HRXRD scan becomes more complicated since the diffraction from buffer and cap layer influences the peak position of the main layer. As a compromise between layer protection and precise determination of x, the layer stack consists of no buffer and only a $Hg_{0.3}Cd_{0.7}Te$ cap layer of roughly 10 nm grown on top. At the end the sample is cooled down to 100 °C in Hg flux to prevent re-evaporation of Hg from the layers. After closing the Hg cell pumping of approximately 30 min is required to reduce the background pressure low enough to enable transfer out of the chamber without risking a contamination of the UHV transfer system with Hg. A schematic overview of the shutter sequence of an exemplary growth cycle can be seen in Table 6.1. A red background represents a closed and a green background an opened cell.

Several samples around the critical composition have been grown and device structures were fabricated for transport characterization. As shown in Figure 4.8, composition, layer thickness and strain due to the usage of a non-lattice matched substrate can have a significant influence on the band gap value. To ensure a good comparability of the different measurements, all samples were grown on CdTe (001) substrates. Additionally, the layer thickness was kept constant at 90 ± 3 nm.

step	cells			
	Hg	Te	Cd	CdTe
heating	closed	open	closed	closed
CdTe buffer				
cooling				
$Hg_{0.3}Cd_{0.7}Te$ buffer				
$Hg_{1-x}Cd_xTe$				
cap $Hg_{0.3}Cd_{0.7}Te$				
cooling				
final pumping				

Table 6.1: Schematic overview of a growth cycle for Hg-based layers on a commercial CdTe substrate.

This thickness was chosen to receive a layer that is

- thick enough to avoid big changes of the critical concentration required for a zero band gap by small thickness deviations (cf. Figure 4.8).
- thick enough to ensure a 3D transport character and to avoid additional transport features caused by size quantization respectively.
- thin enough to ensure a fully strained crystal, even with the addition of buffer and capping layer.

As a consequence the Cd concentration x remains the free parameter to tune the band gap in the $Hg_{1-x}Cd_xTe$ layers. The composition of each layer is measured by HRXRD and obtained from the peak position in the $2\theta\omega$-scans as described in chapter 2.3. Additionally, some samples were examined by scanning transmission electron microscopy (STEM) at the Wilhelm Conrad Röntgen-Center for Complex Material Systems (RCCM). These pictures show a very homogeneous distribution of the atoms in the crystal, which ensures that the measured transport phenomena arise from the conducting $Hg_{1-x}Cd_xTe$ layer and are not interfered by potential clustering in some parts of the layer stack. The brightness of the images is related to the atomic number. Hence, the higher the amount of Hg, the brighter the layer appears. An exemplary image is shown in Figure 6.1.

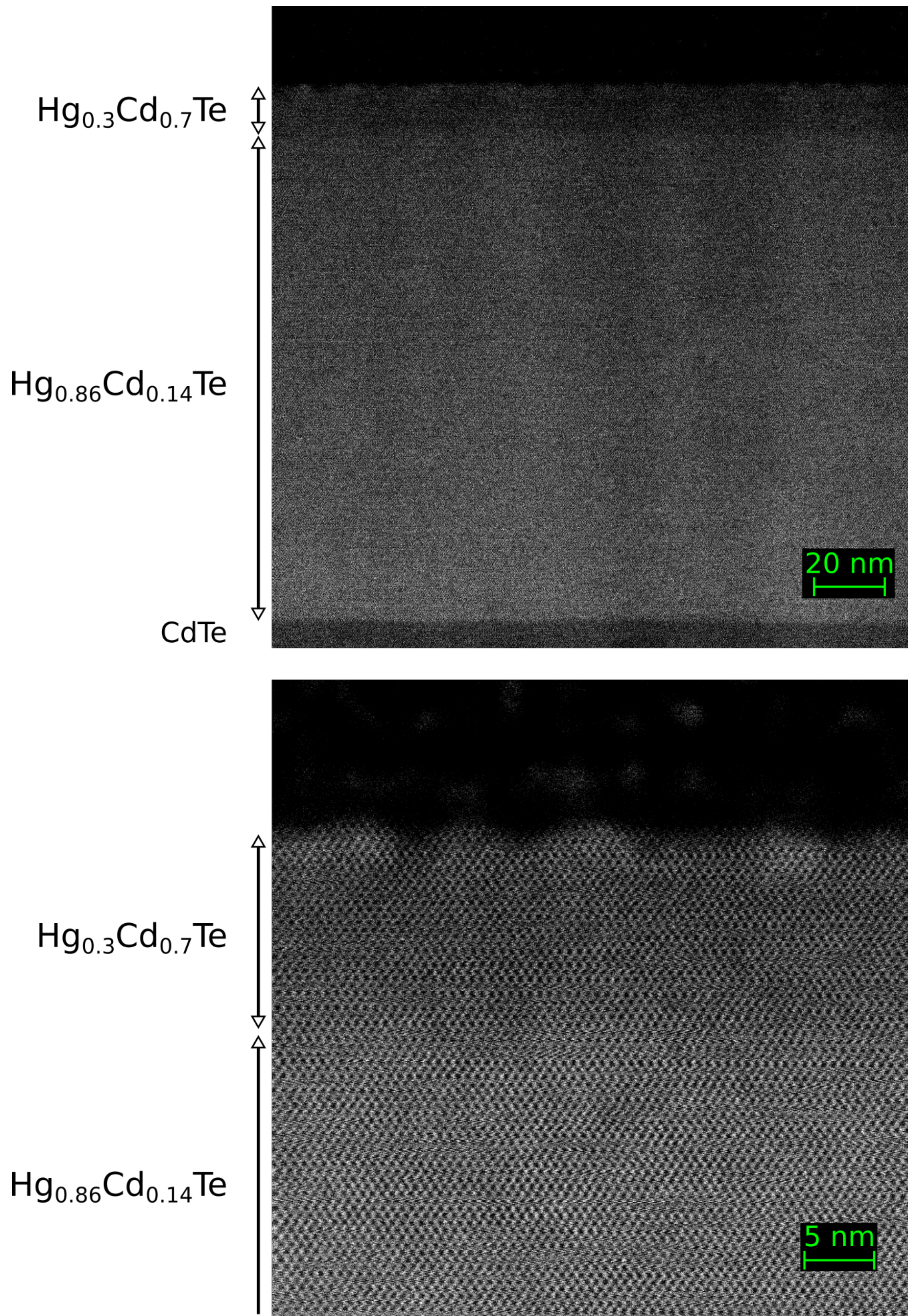

Figure 6.1: STEM images of the layer stack of a $Hg_{0.14}Cd_{0.86}Te$ Dirac-semimetal sample showing a homogeneous material distribution on the atomic scale.

6.2 Magneto electrical transport

In the following the electrical transport properties for various Cd concentrations in $Hg_{1-x}Cd_xTe$ are discussed. Table 6.2 gives an overview of the samples used for this work, with t being the thickness of each layer.

sample Nr.	x	t_{layer}	t_{cap}		sample Nr.	x	t_{layer}	t_{cap}
Q2761	0	90	10		Q2996	0.165	93	11
Q2832	0	70	40		Q2998	0.175	93	11
Q2833	0	70	80		Q2999	0.175	92	11
Q2991	0.12	91	12		Q2877	0.22	100	10
Q2992	0.13	91	12		Q3013	0.225	158	11
Q2993	0.14	90	12		Q3014	0.225	221	11
Q2994	0.15	90	12		Q3010	0.225	316	11
Q2995	0.155	93	11		Q2882	0.36	88	3
Q2997	0.16	91	11					

Table 6.2: Overview of the samples used for investigating the magneto electrical transport phenomena in $Hg_{1-x}Cd_xTe$ for different topological phases.

6.2.1 Negative magneto resistance

The occurrence of a negative magneto resistance for a parallel alignment of magnetic field B and current I is treated as the transport signature of the Dirac-semimetallic phase in $Hg_{1-x}Cd_xTe$. However, there are many observations of a decreasing MR with increasing magnetic field in materials without any Weyl- or Dirac semimetal character (c.f. [65, 66]). The angle dependence of the negative MR caused by the $\vec{E} \cdot \vec{B}$-term in equation 3.4, however, rules out a lot of other origins, as the negative MR in these cases does not show the expected angle dependency. Another reason for the observation of a negative MR can be the presence of an inhomogeneous current distribution resulting in a current-jetting effect, which also shows the typical angular dependence (discussed in detail in [67]). As this occurs in samples with point like contacts, the Hallbar sample design is expected to avoid a current-jetting effect in $Hg_{1-x}Cd_xTe$ as all ohmic contacts overlap the material layer (cf. chapter 3.2).

The Figures 6.2 and 6.3 treat the magneto resistance measured for the sample Q2993 (t_{layer} = 90 nm, x = 0.14), which is exactly at the critical concentration

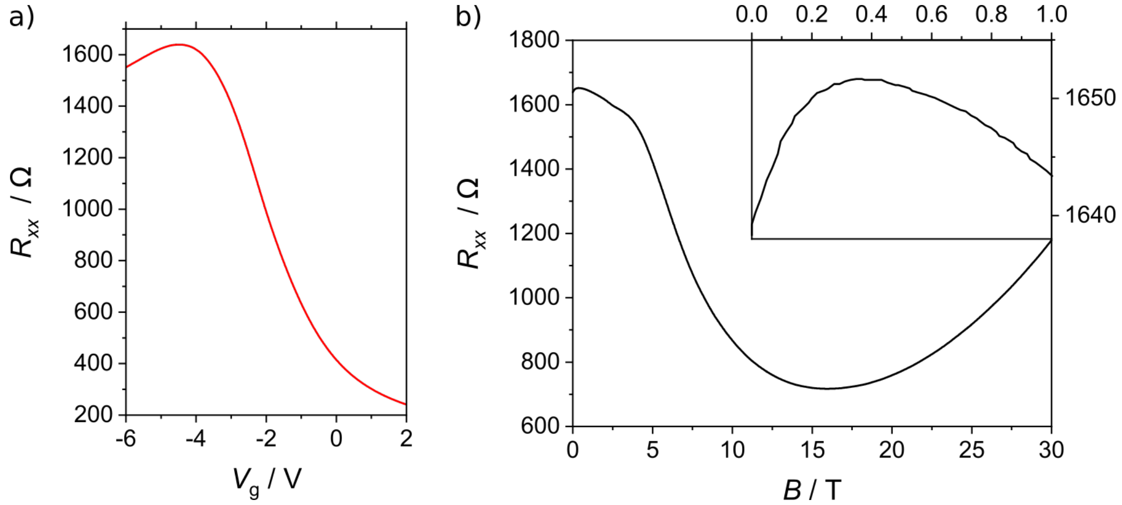

Figure 6.2: a) gate-dependent longitudinal resistance $R_{\mathrm{xx}}(B=0,V_{\mathrm{g}})$ in red and b) magnetic field-dependent longitudinal resistance $R_{\mathrm{xx}}(B,V_{\mathrm{g}}=-4.5\text{ V})$ in black for $B \parallel I$. The inset visualizes the initial increase of R_{xx}.

within the precision range of the HRXRD measurement. The magnetic field is aligned parallel to the current. Figure 6.2 a) shows the density dependent sheet resistance at $B=0$, which exhibits a maximum at $V_{\mathrm{g}}=-4.5$ V. This maximum is associated with the Fermi energy lying at the point of lowest charge carrier density, where according to Figure 4.9 only Dirac states carry the current.

The course of the magneto resistance $R_{\mathrm{xx}}(B,V_{\mathrm{g}}=-4.5\text{ V})$ at this value can be separated into three different parts. For small fields below 0.4 T the resistance increases. This is associated with the weak anti localization, overshadowing a potential negative MR [68]. For $B>0.4$ T the sheet resistance exhibits a strong negative MR at $V_{\mathrm{g}}=-4.5$ V up to 16 T where the resistance decreases to 44% of its initial value. Additionally, the magneto resistance measured for various carrier densities (cf. Figure 6.3) show that this negative part of the MR decreases significantly for V_{g} apart from $V_{\mathrm{g}}=-4.5$ V, when states with a quadratic dispersion are added to the Dirac states. Hence, this decrease is associated with the negative MR caused by the chiral anomaly in Dirac semi metals in the presence of a magnetic field, as discussed in chapter 3.4. At even higher magnetic fields R_{xx} increases again. This could be explained with classical mechanisms of magneto resistance caused by neutral impurity scattering [69].

To address the previously mentioned angle dependency, the measurement of the magneto resistance $R_{\mathrm{xx}}(B,V_{\mathrm{g}}=-4.5\text{ V})$ was repeated for rotations of the sample in the magnetic field from parallel to perpendicular alignment. Due to the sample geometry (cf. chapter 3.1) strong orbital magneto effects can occur for magnetic

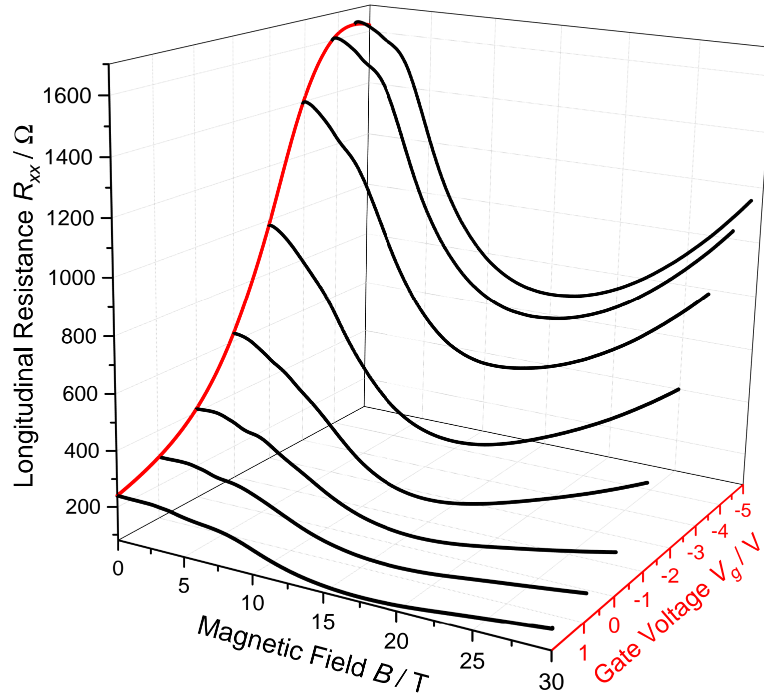

Figure 6.3: Longitudinal resistance $R_{\mathrm{xx}}(B = 0, V_{\mathrm{g}})$ in red and $R_{\mathrm{xx}}(B, V_{\mathrm{g}} = \mathrm{const.})$ in black for $B \parallel I$.

fields in out-of-plane direction. To avoid them it is important to note, that all rotations regarding the angular dependence of the chiral anomaly are done in the layer plane. The rotation angle α is defined $\alpha = 0°$ for B parallel I. Figure 6.4 shows the angle dependence of the sheet resistance for different angles α. For magnetic fields lower than 1.3 T the rotation does not seem to have an influence on the resistance behaviour at all. A possible explanation is that a finite magnetic field is required for the chiral anomaly to set on, as the Dirac point has to split up into two Weyl points before a negative MR is expected (as discussed in chapter 4 and [44]). For magnetic fields higher than 1.3 T there is a clear angle dependence observable with the negative MR being most dominant at a parallel orientation ($\alpha = 0°$). For increasing α the sheet resistance is continually increasing.

Beside the density and angle dependence the influence of the material composition is another relevant aspect which is investigated in the following. Therefore, the behaviour of two samples is investigated, which have a composition sufficiently apart from the critical concentration. So even with some possible concentration fluctuations, their bulk band structure does not exhibit a Dirac-like dispersion in theory. These are a standard HgTe bulk layer (Q2833) and a 90 nm $\mathrm{Hg_{0.78}Cd_{0.22}Te}$

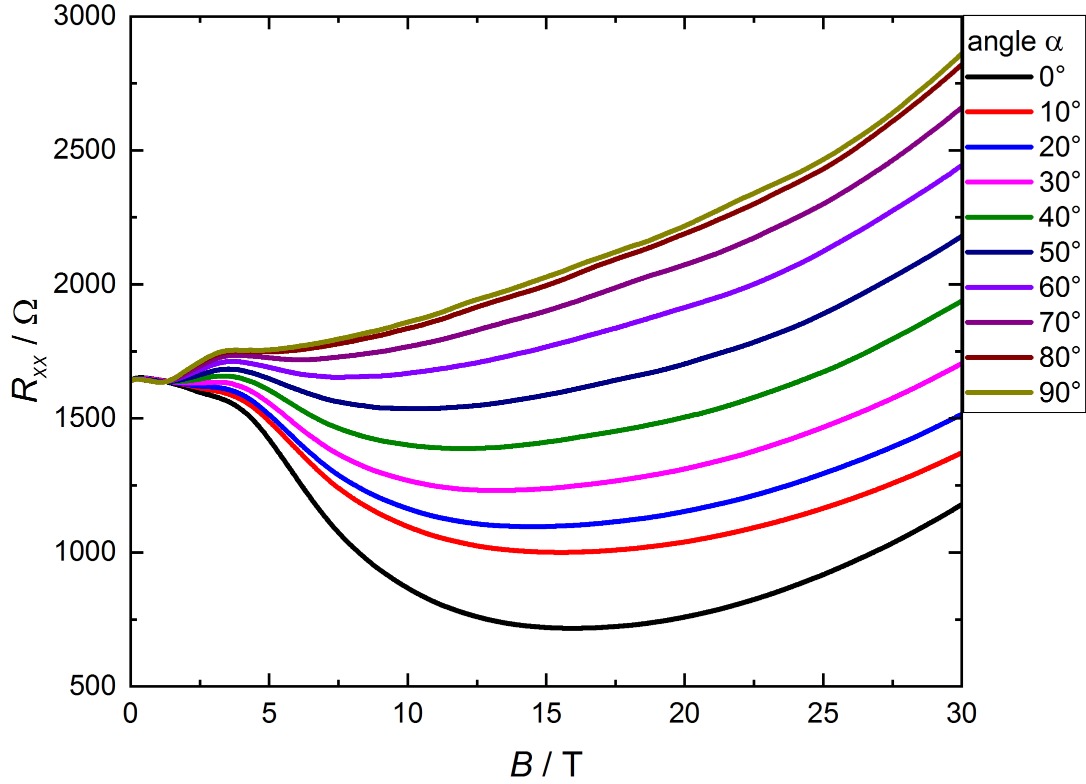

Figure 6.4: Magnetic field-dependent longitudinal resistance for different angles α between field and current in the sample plane.

layer (Q2877). Figure 6.5 shows the magnetic field dependence of the longitudinal resistance R_{xx} for different charge carrier densities, similar to the measurement depicted in Figure 6.3. Both graphs clearly do not show a negative behaviour of the magnetic field-dependent resistance at all, especially for $V_{\mathrm{g}}(R_{\mathrm{xx,max}})$ the trend is strongly positive. This strengthens the confidence that the observed negative MR for the sample Q2993 is due to the fine tuning of the concentration x in the material.

To investigate the composition dependency of the negative MR in more detail, a series of samples was grown, with x varying between 12% and 17.5% and otherwise identical specifications. Again both angle and gate dependency of the sheet resistance were measured in all these samples. Figure 6.6 and Figure 6.7 show the gate dependency of the magnetic field sweep, while the angle dependency is covered in Figure 6.8 and Figure 6.9.

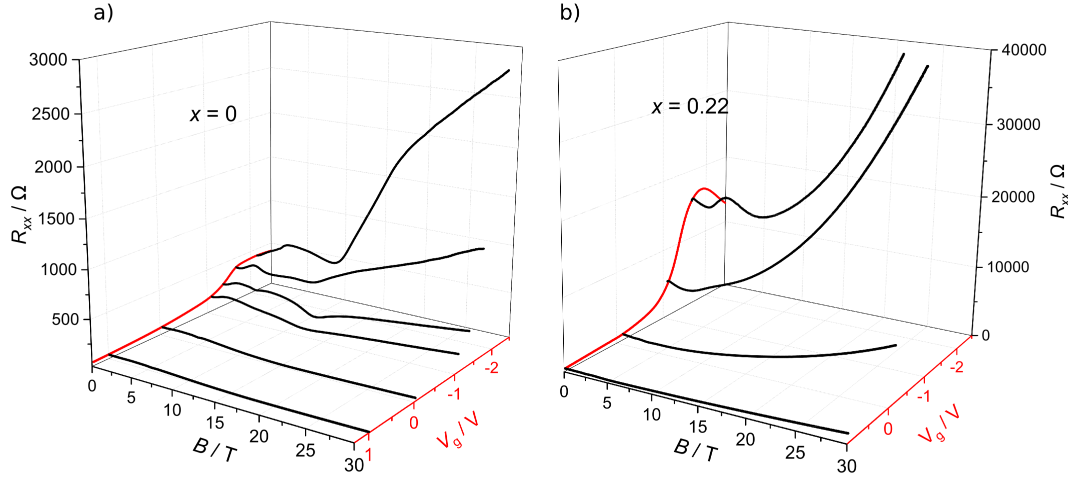

Figure 6.5: Magnetic field-dependent measurements for specific gate voltages for a) HgTe and b) $Hg_{0.78}Cd_{0.22}Te$. In red there is the gatesweep at zero magnetic field.

By comparing the gate-dependent measurements of all these samples one can see that they all show a negative MR in $R_{\mathrm{xx}}(B, V_{\mathrm{g}}(R_{\mathrm{xx,max}})$, which exhibits a similar behaviour, when moving V_{g} away from the point of lowest charge carrier density. Here, one can already see an indication of the composition dependency of the negative MR in these materials. While all of the samples show a negative MR, the sample with the concentration closest to x_c exhibits the strongest decrease in the $R_{\mathrm{xx}}(B, V_{\mathrm{g}}(R_{\mathrm{xx,max}})$, visualized in Figure 6.10. For better comparison $R_{\mathrm{xx}}(B, V_{\mathrm{g}}(R_{\mathrm{xx,max}})) - Rxx(B = 0, V_{\mathrm{g}}(R_{\mathrm{xx,max}}))$ was taken to account for the different longitudinal resistances at $B = 0$ of the different samples.

Comparing the angle dependencies for in-plane rotation of the different samples, the influence of composition changes becomes clearer (cf. Figure 6.8 and 6.9). The samples with $x = 0.13$ and $x = 0.15$ show a similar angular dependence, compared with $x = 0.14$. In contrast the angle dependence of the samples with $x = 0.12$, $x = 0.165$ and $x = 0.175$ is significantly different. While there is still an influence of the angle on the sheet resistance in these samples, the angle dependence does not follow the expected behaviour discussed in chapter 3.4 and observed in Figure 6.4. So the angle dependent negative MR clearly shows a concentration dependence, whose origin can be explained by the chiral anomaly in Dirac and Weyl semimetals, associated with a linear dispersion in the bulk band structure at a critical concentration x_c.

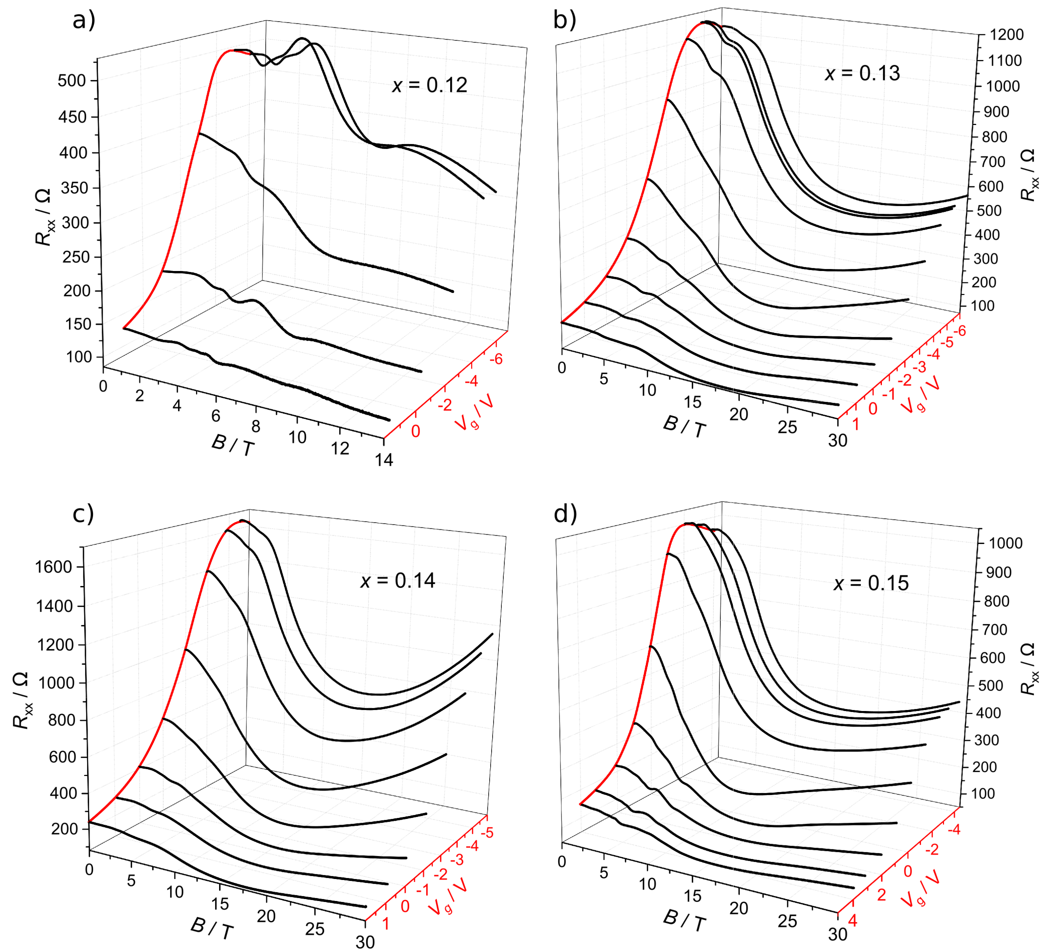

Figure 6.6: Longitudinal resistance $R_{\text{xx}}(B = 0, V_{\text{g}})$ in red and $R_{\text{xx}}(B, V_{\text{g}} = \text{const.})$ in black for different values of x.
a) $Hg_{0.88}Cd_{0.12}Te$
b) $Hg_{0.87}Cd_{0.13}Te$
c) $Hg_{0.86}Cd_{0.14}Te$
d) $Hg_{0.85}Cd_{0.15}Te$

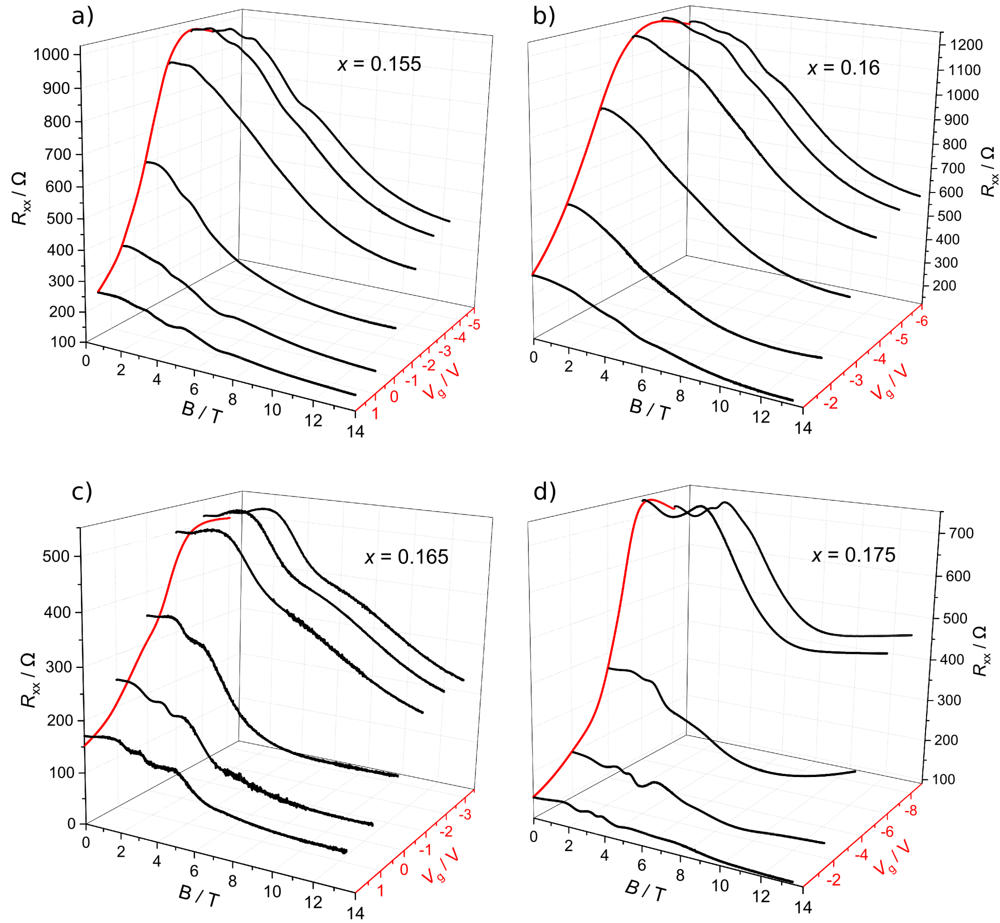

Figure 6.7: Longitudinal resistance $R_{\mathrm{xx}}(B=0,V_{\mathrm{g}})$ in red and $R_{\mathrm{xx}}(B,V_{\mathrm{g}}=\mathrm{const.})$ in black for different values of x.
a) $Hg_{0.845}Cd_{0.155}Te$
b) $Hg_{0.84}Cd_{0.16}Te$
c) $Hg_{0.835}Cd_{0.165}Te$
d) $Hg_{0.825}Cd_{0.175}Te$

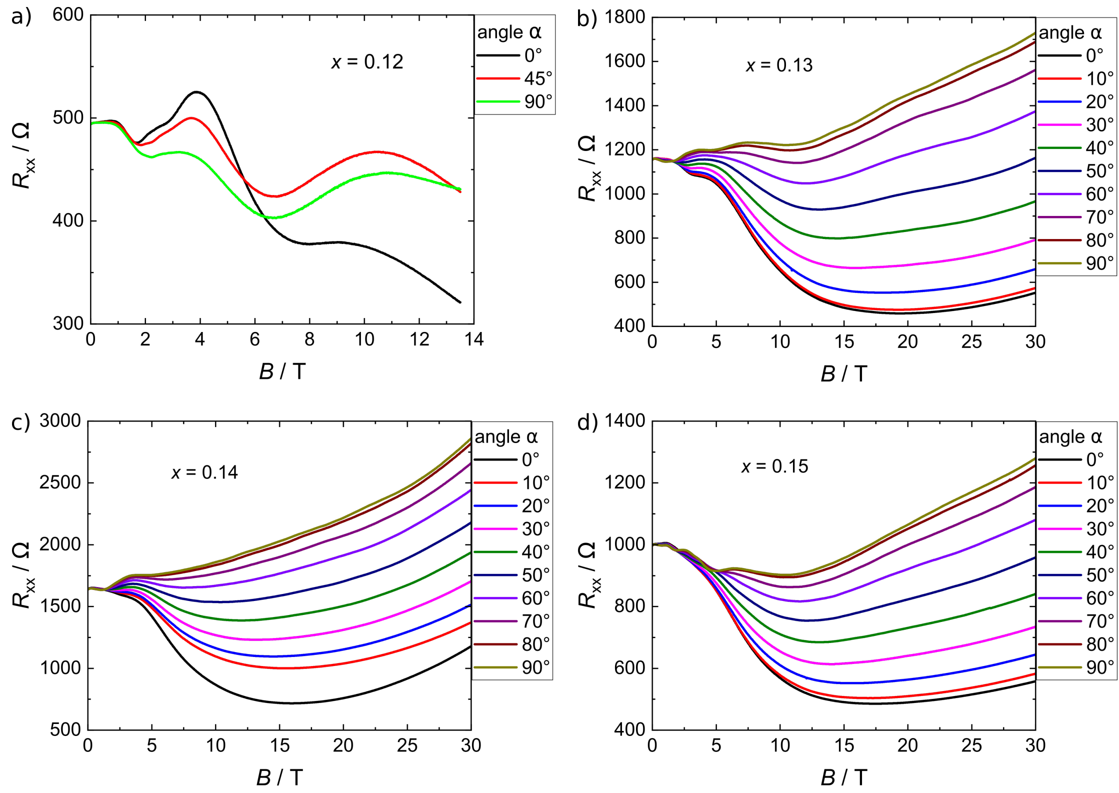

Figure 6.8: Angle dependency by rotation in the sample plane of the magneto resistance at the point of lowest charge carrier density for different values of x.
a) $Hg_{0.88}Cd_{0.12}Te$
b) $Hg_{0.87}Cd_{0.13}Te$
c) $Hg_{0.86}Cd_{0.14}Te$
d) $Hg_{0.85}Cd_{0.15}Te$

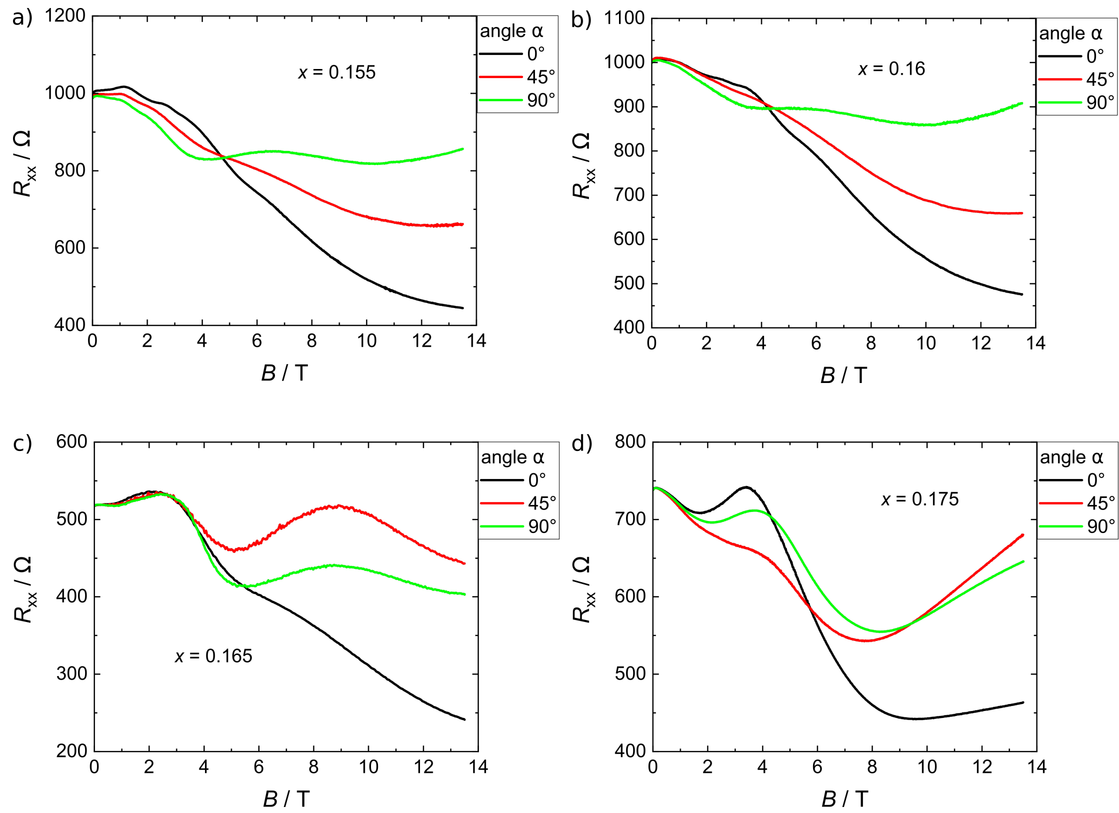

Figure 6.9: Angle dependency by rotation in the sample plane of the magneto resistance at the point of lowest charge carrier density for different values of x.
a) $Hg_{0.845}Cd_{0.155}Te$
b) $Hg_{0.84}Cd_{0.16}Te$
c) $Hg_{0.835}Cd_{0.165}Te$
d) $Hg_{0.825}Cd_{0.175}Te$

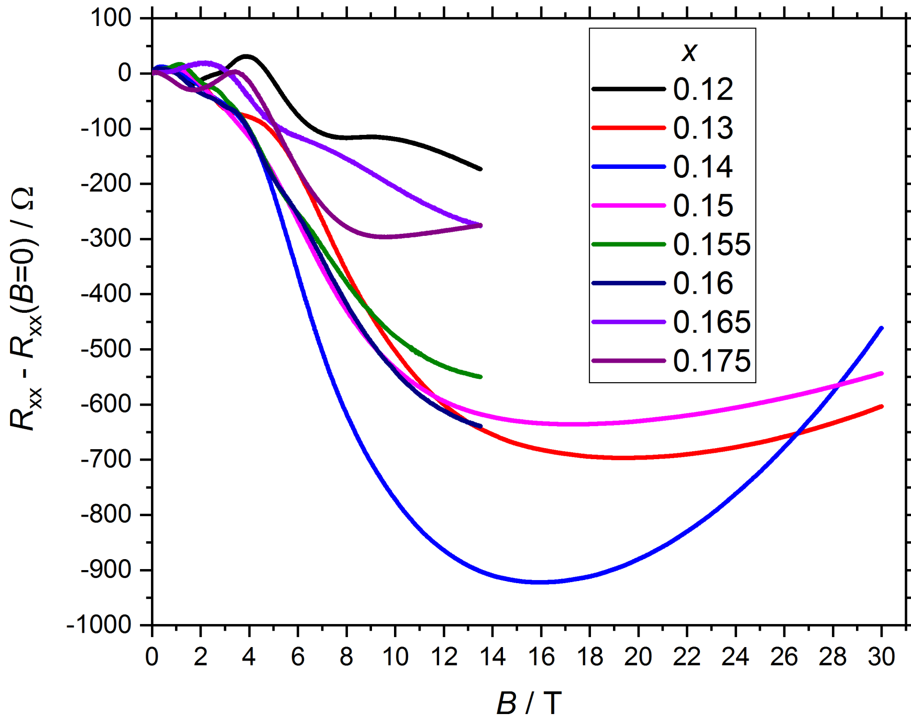

Figure 6.10: Comparison of $R_{\mathrm{xx}}(B, V_{\mathrm{g}}(R_{\mathrm{xx,max}})$ for samples with different concentrations x.

The fact that this negative MR behaviour appears over a wider concentration range and not only exactly for $x = x_c$ can have several reasons. The origin of the chiral anomaly is a linear dispersion in the band structure. As the transition from a quadratic dispersion in the TI and semiconductor state towards a linear dispersion in the semimetallic state continues gradually, the dispersion still holds a significant linear portion for deviations from $x = x_c$ of around 0.01. Additionally experimental uncertainties need to be considered. First of all the evaluation of x from the HRXRD measurements has an error of around 0.005 to 0.01, which is in the same order of magnitude as the concentration window observed. Furthermore, HRXRD only gives the mean value of x for a certain layer. While larger fluctuations of the concentration can be ruled out by the low FWHM of the $Hg_{1-x}Cd_xTe$ layers and by the homogeneity in the STEM pictures, small fluctuations of around 0.01 are still possible. Finally one has to consider that $\mathrm{k} \cdot \mathrm{p}$ calculations assume a perfectly homogeneous crystal for any value of x by interpolating concentration-dependent crystal values (e.g. lattice constant) for $Hg_{1-x}Cd_xTe$ from the values of the binary compounds CdTe and HgTe, which makes concentration fluctuations at this scales inevitable.

6.2.2 Hall measurements

Alongside the behaviour for a magnetic field aligned in the sample plane, measurements dependent on an out-of-plane magnetic field have also been carried out in $Hg_{1-x}Cd_xTe$ bulk for x close to x_c. These measurements allow the determination of n and μ as characteristic transport values for comparison with pure HgTe.

Therefore, the longitudinal resistance R_{xx} and the Hall resistance R_{xy} for the sample with $x = 0.14$ are addressed which hits the right composition for a Dirac semimetal and also shows the expected transport features according to the discussion in chapter 4. The resulting curves are highly dependent on the position of the Fermi energy in the material and need to be discussed with respect to the specific gate voltage. The gate-dependent sheet resistance is shown in Figure 6.11 a). Magnetic field dependencies of R_{xx} and R_{xy} of $V_{\mathrm{g}} = V(R_{\mathrm{xx,max}})$ (Figure 6.11 c), which

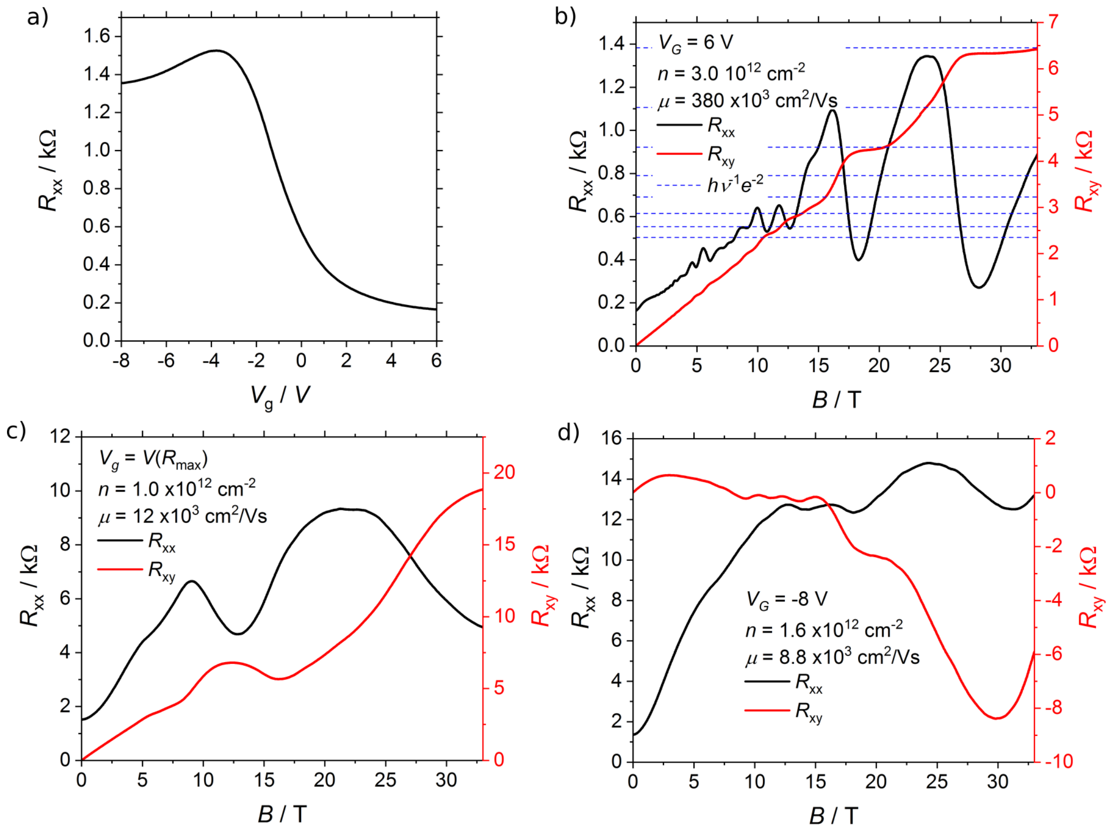

Figure 6.11: Magneto electrical transport measurements of a $Hg_{0.86}Cd_{0.14}Te$ Dirac-semimetal with B aligned parallel to the layers normal. a) shows the gate-dependent sheet resistance. b)-d) show the magnetic field dependence of R_{xx} and R_{xy} for three distinct gate voltages, with b) exhibiting a Fermi energy above, c) directly at, and d) below the charge neutrality point.

reflects the mobility edge in the band diagram where mostly Dirac states carry the current, and at a higher ($V_g = 6$ V, Figure 6.11 b) and lower ($V_g = -8$ V, Figure 6.11 d) voltage are shown respectively. The charge carrier density was determined by approximating a linear increase in resistance for small B-fields around $B = 0$. All measurements show charge carrier densities in the order of 10^{12} cm^{-2}, which is an order of magnitude higher compared to a HgTe 3D topological insulator [48]. However, if this can be lowered by introducing a bottom $Hg_{0.3}Cd_{0.7}Te$ barrier and increasing the cap thickness as it is the case for HgTe 3D topological insulator samples or if this is caused by the semimetallic character of $Hg_{0.14}Cd_{0.86}Te$, is a topic of further investigations. With the value of n one can furthermore calculate the Fermi wavelength of the charge carrying electrons to be in the range of 15 to 25 nm, which is well below the thickness of the $Hg_{1-x}Cd_xTe$ layer. This is important to exclude quantum size effects on the resistivity due to lateral confinement when the layer thickness becomes comparable to the Fermi wavelength [40]. Therefore, measurements of the magnetic field dependence of R_{xx} and R_{xy} provide information about the impact of surface states on the transport at compositions of $x \simeq x_c$, as surface states cause a 2DEG on the edges of the layer leading to the observation of the QHE as shown for HgTe [50]. As already discussed in chapter 4.2, surface states are still present in the band structure of $Hg_{1-x_c}Cd_{x_c}Te$ but are very weak due to their high localization length. The measurements for $V_g = V(R_{\mathrm{xx,max}})$ and $V_g = -8$ V do not show a clear sign of a QHE effect. The measurement at $V_g = 6$ V clearly shows a behaviour expected from the QHE. However, as already discussed in chapter 3.3, the QHE is a characteristic effect of a 2DEG, but the existence of a 2DEG in semiconductor heterostructures can have various origins. The fact that the QHE only occurs at high positive gate voltages and that simultaneously μ increases by a factor of 30, leans toward the interpretation that the origin of the QHE in these samples is a gate-induced 2DEG, similar to the occurrence of a 2DEG in a MOSFET. This shows that observations of transport effects caused by the Dirac semimetallic phase in $Hg_{1-x_c}Cd_{x_c}Te$ are possible without a superposition of surface states related effects.

Summary

The subject of this thesis is the growth of $Hg_{1-x}Cd_xTe$ layers via molecular beam epitaxy (MBE). This material system gives rise to a number of extraordinary physical phenomena related to its electronic band structure and therefore is of fundamental interest in research. The main results can be divided into three main areas, the implementation of a temperature measurement system based on band edge thermometry (BET), improvements of CdTe virtual substrate growth and the investigation of $Hg_{1-x}Cd_xTe$ for different compositions.

First, the implementation of a new tool for measuring the substrate temperature is addressed, based on the band edge thermometry (BET) technique as well as its comparison to the temperature measurement with a thermocouple (TC). This technique was introduced to investigate and solve some consistency issues with the growth of $Hg_{1-x}Cd_xTe$ on CdTe substrates, which were suspected to be related to inconsistencies during the measurement of the substrate temperature. Therefore, BET-controlled substrate temperature is compared to TC. Comparisons with the TC-controlled temperature measurement show that BET exhibits a much better representation of the temperature at the growth front and therefore increases the reliability of the temperature significantly. This further leads to a decrease in the overall time required for a full growth cycle. The maximum layer thickness for a sufficient BET signal was determined to be roughly of the order of 160 nm of HgTe, as the Hg-containing layers grown on top of the substrate are obscuring the BET signal. In addition, it was possible to determine the temperature window for the surface morphology with the lowest defect density to be $T = 157 \pm 1°C$.

Second, the growth conditions for building CdTe (001) virtual substrates (VS) based on GaAs:Si (001) were improved, a work which was started in 2010 by C. Ames [6]. Different layer stack compositions as well as the applicability of InAs:S (001) as the initial substrate were investigated in the context of surface morphology, electrical transport properties and back gate efficiency for HgTe quantum wells (QW) grown on top of the VS. Regarding the surface morphology both an

additional Cd-based annealing step as well as a final CdTe layer grown by atomic layer epitaxy (ALE) showed a decrease in the overall surface roughness. Both processes can simply be added at the end of the growth process. Increasing the CdTe buffer thickness to 12 µm did change the surface morphology significantly by increasing the hill-to-valley distance both vertically and horizontally. Because the horizontal hill-to-valley distance is now larger than the size of common microstructures (below 6 µm), if used for these structures, an increased CdTe buffer leads to smaller effective surface roughness.

Regarding the quality of electrical transport properties there is no significant difference in the characteristic transport features between the different VS types, which could also not be explained with previously observed fluctuations originating from the manufacturing processes. Therefore, more statistic is required to establish an advantage of one VS type over the other. However, this allows a change of the VS layer stack to increase backgate stability without trading this for a decreasing transport quality. Here a VS layer stack with a ZnSe/ZnTe superlattice (SL) between the GaAs:Si substrate and the 4 µm CdTe buffer stands out in terms of backgate stability, covering a range of −40.1 V to 28.8 V. Other VS could not exceed a range of −30 V to 8 V.

Third, the ternary material $Hg_{1-x}Cd_xTe$ is investigated for different Cd concentrations x. Hereby, a special interest lies on the transition point from topological insulator (HgTe) and common semiconductor (CdTe). Scanning transmission electron microscopy (STEM) measurements show a very homogeneous atom distribution over the layer. The occurrence of a negative magneto resistance (MR) for a parallel alignment of magnetic field and current is used as a characterization tool to distinguish the three topological phases accessible in $Hg_{1-x}Cd_xTe$. This identified a Dirac semimetallic phase in $Hg_{0.86}Cd_{0.14}Te$ at the transition point from the topological insulator phase present in HgTe and the common semiconductor phase present in CdTe. Additional measurements in a Hall configuration (magnetic field perpendicular to the samples surface) did not show surface state-related transport signals, strengthening the argument that there are no surface states rivalling the Dirac semimetal related transport phenomena in $Hg_{0.14}Cd_{0.86}Te$.

The implementation of a BET-based temperature measurement system did improve the reliability of growing $Hg_{1-x}Cd_xTe$ layers. This technique is currently transferred to the growth of CdTe nanowires with very promising results. The improvements on the growth of CdTe VS, especially the increased backgate range

offer new possibilities in electrical transport measurements. The possibility to flexibly change the composition in $Hg_{1-x}Cd_xTe$ leads to the verification of a Dirac semimetallic phase. Furthermore, this could be used to adjust the band gap value in $Hg_{1-x}Cd_xTe$ quantum wells to enable a switching of the intrinsic quantum hall effect with the bias electric field, which was theoretically predicted by W. Yang et al. [70].

Zusammenfassung

Gegenstand dieser Arbeit ist das Wachstum von $Hg_{1-x}Cd_xTe$-Schichten mittels Molekularstrahlepitaxie (MBE). Die elektronische Bandstruktur dieses Materials führt zu einer Reihe außergewöhnlicher physikalischer Phänomene. Es ist daher für die Forschung von grundlegendem Interesse. Die Ergebnisse lassen sich in drei Hauptbereiche unterteilen: die Implementierung eines Temperaturmessgeräts basierend auf dem Prinzip der Bandkantenthermometrie (BET), die Verbesserung des Wachstums von virtuellen CdTe-Substraten und die Untersuchung von $Hg_{1-x}Cd_xTe$-Schichten für verschiedene Materialkonzentrationen.

Zunächst wird die Implementierung eines neuen Messgerätes zur Messung der Substrattemperatur beschrieben, das auf dem Prinzip der Bandkantenthermometrie (BET) basiert. Ziel der Temperaturmessung mittels BET ist es einige Konsistenzprobleme mit dem Wachstum von $Hg_{1-x}Cd_xTe$ auf CdTe-Substraten zu untersuchen und zu lösen, von denen vermutet wurde, dass sie mit Inkonsistenzen während der Messung der Substrattemperatur zusammenhängen. Daher wird die BET-gesteuerte Substrattemperatur mit der des bereits vorhandenen Thermoelements (TC) verglichen. Vergleiche mit der TC-gesteuerten Temperaturmessung zeigen, dass BET die Temperatur an der Wachstumsfront wesentlich besser wiedergibt und damit die Zuverlässigkeit der Temperaturmessung deutlich erhöht. Dies führt ferner zu einer Verkürzung der Gesamtzeit, die für einen vollständigen Wachstumszyklus erforderlich ist. Es wurde festgestellt, dass die maximale Schichtdicke für ein ausreichendes BET-Signal ungefähr in der Größenordnung von 160 nm HgTe liegt, da die auf dem Substrat gewachsenen Hg-haltigen Schichten das BET-Signal verdecken. Zusätzlich konnte das Temperaturfenster für eine möglichst defektarme Oberflächenmorphologie zu $T = 157 \pm 1°C$ bestimmt werden.

Weiterhin wurden die Wachstumsbedingungen für virtuelle CdTe (001) Substrate (VS) auf der Basis von GaAs:Si (001) verbessert, was die 2010 von C. Ames [6] begonnene Arbeit fortführt. Verschiedene Stapelfolgen unterschiedlicher Schichten

sowie die Eignung von InAs:S (001) als Ausgangssubstrat wurden im Bezug auf die Oberflächenmorphologie, die elektrischen Transporteigenschaften und die Backgate-Effizienz für auf dem VS gewachsene HgTe-Quantentöpfe (QW) untersucht. Im Bezug auf die Oberflächenmorphologie zeigten sowohl ein zusätzlicher thermischer Ausheilschritt als auch eine abschließend durch Atomlagenepitaxie (ALE) gewachsene CdTe-Schicht eine Abnahme der Oberflächenrauheit. Beide Prozesse können ohne zusätzliche Änderungen am Ende des Wachstumsprozesses hinzugefügt werden. Ein Erhöhen der Dicke der CdTe-Pufferschicht auf 12 µm führte zu einer signifikanten Änderung die Oberflächenmorphologie. So erhöhte sich der Abstand zwischen Hügel und Tal sowohl vertikal als auch horizontal. Da der horizontale Abstand zwischen Hügeln und Tälern somit die Größe üblicher Mikrostrukturen (unter 6 µm) übersteigt, führt ein dickerer CdTe-Puffer zu einer geringeren effektiven Oberflächenrauheit für Strukturen dieser Größe.

In Bezug auf die Qualität der elektrischen Transporteigenschaften gibt es keinen signifikanten Unterschied in den charakteristischen Transportmerkmalen zwischen den verschiedenen VS-Typen, welche nicht auch mit bekannten Schwankungen erklärt werden könnten, die durch den Herstellungsprozess verursacht werden. Daher ist mehr Statistik erforderlich, um einen Vorteil eines VS-Typs gegenüber dem anderen festzustellen. Dies ermöglicht jedoch eine Änderung der Schichtabfolge, um die Backgate-Stabilität zu erhöhen, ohne im Gegenzug eine abnehmende Transportqualität zu erwarten. Das stabilste Backgate konnte hierbei an eine VS mit ZnSe/ZnTe-Übergitter zwischen dem GaAs:Si-Substrat und dem 4 µm dicken CdTe-Puffer gemessen werden, welches einen Bereich von −40.1 V bis 28.8 V abdeckt. Die Durchbruchsspannungen anderer VS konnten einen Bereich von −30 V bis 8 V nicht überschreiten.

Der dritte Teil widmet sich dem ternären Material $Hg_{1-x}Cd_xTe$ bei verschiedenen Cd-Konzentrationen x. Hierbei liegt ein besonderes Interesse auf dem Übergangspunkt vom topologischen Isolator (HgTe) zum trivialen Halbleiter (CdTe). Messungen mit einem Rastertransmissionselektronenmikroskop (STEM) zeigen eine homogene Verteilung der Atome in der Schicht. Das Auftreten eines negativen Magnetowiderstands (MR) für eine parallele Ausrichtung von Magnetfeld und Strom ist hierbei das charakteristische Merkmal, um die drei in $Hg_{1-x}Cd_xTe$ zugänglichen topologischen Phasen zu unterscheiden. Hiermit konnte zwischen der in HgTe vorhandenen topologischen Isolatorphase und der in CdTe vorhandenen Halbleiterphase eine Dirac-Halbmetallphase in $Hg_{0.86}Cd_{0.14}Te$ festgestellt werden. Zusätzliche Messungen in einer Hall-Konfiguration (Magnetfeld senkrecht zur

Probenoberfläche) zeigten keine Transportsignale, die auf potentiell vorhandene Oberflächenzustände zurückzuführen sind. Dies bekräftigt das Argument, dass es in $Hg_{0.86}Cd_{0.14}Te$ keine Oberflächenzustände gibt, die mit den Transportphänomenen der Dirac-Halbmetallphase konkurrieren.

Die Implementierung eines neuen Messgerätes zur Bestimmung der Substratetemperatur basierend auf BET verbessert die Reproduzierbarkeit von MBE-gewachsenen $Hg_{1-x}Cd_xTe$-Schichten. Diese Technik wird derzeit mit vielversprechenden Ergebnissen auf das Wachstum von CdTe-Nanodrähten übertragen. Die Verbesserungen beim Wachstum von CdTe VS, insbesondere die erhöhte Backgate-Stabilität, eröffnen neue Möglichkeiten bzgl. elektrischer Transportmessungen. Die flexibel Änderung der Zusammensetzung von $Hg_{1-x}Cd_xTe$, ermöglicht den Nachweis einer Dirac-Halbmetallphase in diesem Material. Darüber hinaus könnten die gewonnen Erkenntnisse über das Wachstum verwendet werden, um die theoretische Vorhersage von W. Yang et al. [70] experimentell nachzuweisen, wonach ein Schalten des intrinsischen Quanten-Hall-Effekts mit der Anregungsspannung in $Hg_{1-x}Cd_xTe$-Quantentrögen möglich ist, sofern die Bandlücke entsprechend angepasst wird.

A Virtual substrate: charge carrier density and mobility

Charge carrier mobility μ and density n are used as a characterization tool for 2DEG structures. To compare the influence of different virtual substrates on the transport properties of HgTe quantum wells, Figure A.1 shows the Gate voltage dependency of the longitudinal sheet resistance R_{xx} and of the charge carrier n and μ.

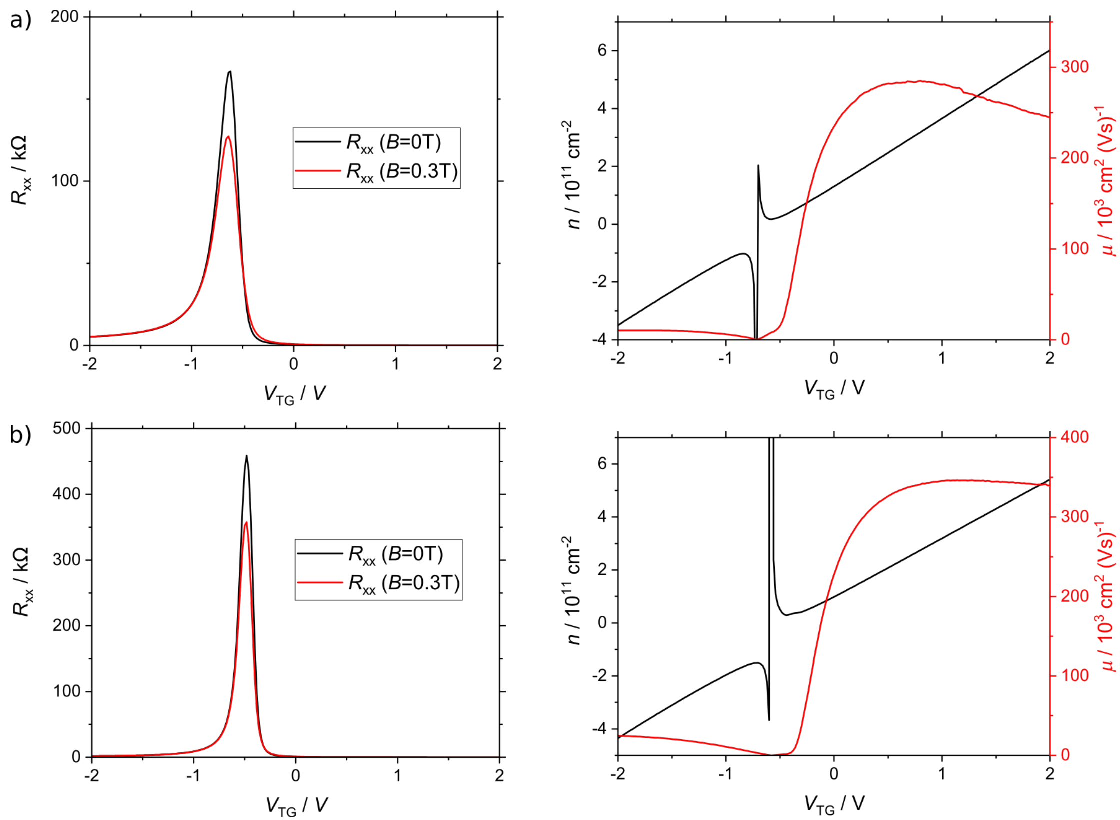

continues on next page

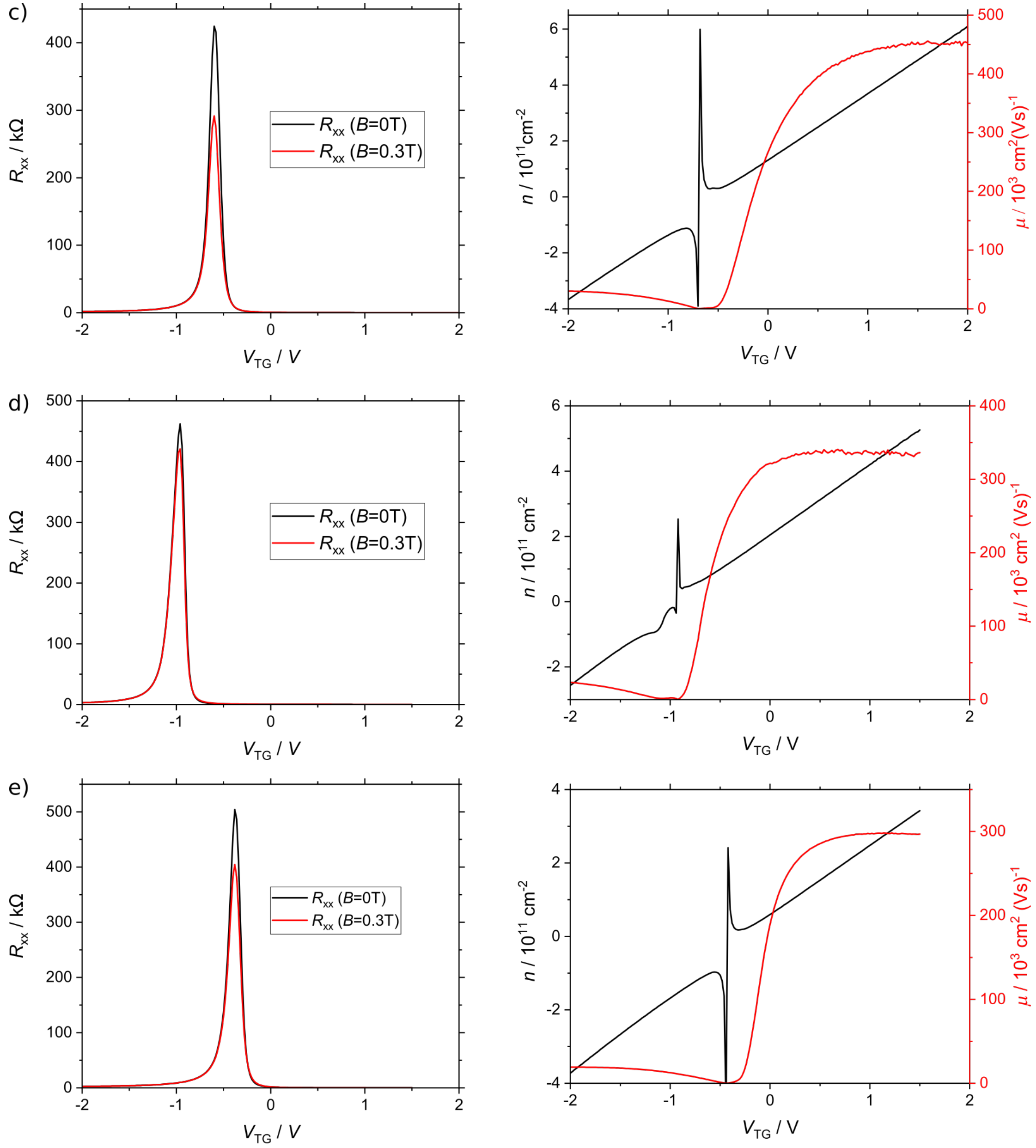

Figure A.1: Gate voltage dependency of the longitudinal sheet resistance R_{xx} (left pictures) at a magnetic field of 0 T and 0.3 T, and of charge carrier density n and mobility μ (right picture) for HgTe QW on the different VS types shown in table 5.1.
a) Q2940 - CdTe on GaAs
b) Q2941$_{\parallel}$ - CdTe on InAs
c) Q2941$_{\perp}$ - CdTe on InAs
d) Q2944 - CdTe on ZnSe/ZnTe
e) Q2950 - CdTe on InAs

Bibliography

[1] V. Mourik, K. Zuo, S. M. Frolov, S. R. Plissard, E. P. A. M. Bakkers, and L. P. Kouwenhoven. Signatures of Majorana Fermions in Hybrid Superconductor-Semiconductor Nanowire Devices. *Science*, 336(6084):1003–1007, May 2012.

[2] W. S. Boyle and G. E. Smith. Charge coupled semiconductor devices. Bell Syst. Tech. J. 49:587-93, 1970. *Bell Syst. Tech. J.*, 49(587-93), 1970.

[3] Klaus von Klitzing. The quantized Hall effect. *Reviews of Modern Physics*, 58(3):519–531, July 1986.

[4] M. König, S. Wiedmann, C. Brüne, A. Roth, H. Buhmann, L. W. Molenkamp, X.-L. Qi, and S.-C. Zhang. Quantum Spin Hall Insulator State in HgTe Quantum Wells. *Science*, 318(5851):766–770, November 2007.

[5] D. Hsieh, D. Qian, L. Wray, Y. Xia, Y. S. Hor, R. J. Cava, and M. Z. Hasan. A topological Dirac insulator in a quantum spin Hall phase. *Nature*, 452(7190):970–974, April 2008.

[6] Christopher Ames. *Molecular Beam Epitaxy of 2D and 3D HgTe, a Topolgical Insulator.* PhD thesis, Julius Maximilians Universität, Würzburg, 2015.

[7] Lena Fürst. Konzentrationsabhangiges Wachstum und Charakterisierung von HgCdTe. Master's thesis, Julius Maximilians Universität, Würzburg, 2018.

[8] Marian A. Herman and H. Sitter. *Molecular Beam Epitaxy.* Number 7 in Springer Series in Materials Science. Springer-Verlag, Berlin, 1989.

[9] J. A. Venables, M. Hanbucken, and G. D. T. Spiller. Nucleation and growth of thin films. *Reports on Progress in Physics*, 47:62, 1984.

[10] Medona B. Denton, Wayne L. Johnson, and Murray D. Sirkis. Method of wafer band-edge measurement using transmission spectroscopy and a process for controlling the temperature uniformity of a wafer. \textit{United States Patent} US 6,891,124 B2, 2001.

[11] E. Selvig, C. R. Tonheim, K. O. Kongshaug, T. Skauli, H. Hemmen, T. Lorentzen, and R. Haakenaasen. Defects in CdHgTe grown by molecular beam epitaxy on (211)B-oriented CdZnTe substrates. *Journal of Vacuum Science & Technology B: Microelectronics and Nanometer Structures*, 26(2):525, 2008.

[12] Sadao Adachi. *Handbook on physical properties of semiconductors vol.3 II-VI.pdf*, volume 3. Kluwer Academic Publishers, New York, 2004.

[13] W. E. Hoke, D. Barlett, T. D. Kennedy, B. Wissman, and J. J. Mosca. Short wavelength band edge thermometry during molecular beam epitaxial growth of GaN on SiC substrates and detected adatom self-heating effects. *Journal of Vacuum Science & Technology B, Nanotechnology and Microelectronics: Materials, Processing, Measurement, and Phenomena*, 28(3):C3F5–C3F9, May 2010.

[14] Ri-an Zhao, Michael J. Cich, Petra Specht, and Eicke R. Weber. In situ diffuse reflectance spectroscopy investigation of low-temperature-grown GaAs. *Applied Physics Letters*, 80(12):2060–2062, March 2002.

[15] Alexander Pfeuffer-Jeschke. *Bandstruktur und Landau-Niveaus quecksilberhaltiger II-VI-Heterostrukturen.* PhD thesis, Julius Maximilians Universität, Würzburg, 2000.

[16] J.F. Nye. *Physical properties of crystals. Their representation by tensors and matrices.* Oxford University Press, Oxford, 7 edition, 1976.

[17] Jan H. Van Der Merwe. The role of lattice misfit in epitaxy. *Critical Reviews in Solid State and Materials Sciences*, 7(3):209–231, October 1978.

[18] D J Dunstan. Strain and strain relaxation in semiconductors. *JOURNAL OF MATERIALS SCIENCE: MATERIALS IN ELECTRONICS*, 8:337–375, 1997.

[19] T. Skauli, T. Colin, R. Sjølie, and S. Løvold. Misfit relaxation behavior in CdHgTe layers grown by molecular beam epitaxy on CdZnTe substrates. *Journal of Electronic Materials*, 29(6):687–690, June 2000.

[20] P. Ballet, C. Thomas, X. Baudry, C. Bouvier, O. Crauste, T. Meunier, G. Badano, M. Veillerot, J. P. Barnes, P. H. Jouneau, and L. P. Levy. MBE Growth of Strained HgTe/CdTe Topological Insulator Structures. *Journal of Electronic Materials*, 43(8):2955–2962, August 2014.

[21] Otfried Madelung. *Semiconductors - Basic Data*. Springer-Verlag, Berlin, 2. edition, 1996.

[22] H. P. Singh and B. Dayal. X-Ray Determination of the Thermal Expansion of Zinc Selenide. *physica status solidi (b)*, 23(1):K93–K95, 1967.

[23] Peter Capper. *Narrow Gap Cadmium based Compounds*. INSPEC, the Institution for Electrical Engineers, London, 1994.

[24] L. Vegard. Die Konstitution Der Mischkristalle und die Raumfüllung der Atome. *Zeitschrift für Physik*, pages 17 – 26, 1921.

[25] W. Lang. Nomarski differential interference-contrast microscopy. *Zeiss Information*, 70:114–120, 1968.

[26] G. Binnig, C. F. Quate, and Ch. Gerber. Atomic Force Microscope. *Physical Review Letters*, 56(9):930–933, March 1986.

[27] G. Binnig. Atomic Force Microscope and Method for Imaging Surfaces with Atomic Resolution. \textit{United States Patent} US 4,724,318, February 1988.

[28] B. Cappella and G. Dietler. Force-distance curves by atomic force microscopy. *Surface Science Reports*, 34(1-3):1–104, January 1999.

[29] F. Golek, P. Mazur, Z. Ryszka, and S. Zuber. AFM image artifacts. *Applied Surface Science*, 304:11–19, June 2014.

[30] Miho Yasaka. X-ray thin-film techniques. *The Rigaku Journal*, 26(2), 2010.

[31] Heinz Kiessig. Interferenz von Röntgenstrahlen an dünnen Schichten. *Annalen der Physik*, 402(7):769–788, 1931.

[32] B. E. Warren. *X-Ray Diffraction*. Dover Publications, New York, 1990.

[33] W. H. Bragg and W. L. Bragg. The reflection of X-rays by crystals. *Proceedings of the Royal society A*, 88(605):428–438, 1913.

[34] Charles Kittel. *Introduction to Solid State Physics*. John Wiley & Sons, 8. edition edition, 2005.

[35] L. Lunczer. Bandlückenmaximierung in hochverspannten, invertierten HgTe-Quantentrögen. Master's thesis, Julius Maximilians Universität, Würzburg, 2016.

[36] Ayahiko Ichimiya and Philip I. Cohen. *Reflection High Energy Electron Diffraction*. Cambridge University Press, Cambridge, 2004.

[37] S. Hasegawa. REFLECTION HIGH-ENERGY ELECTRON DIFFRACTION. *Characterization of Materials*, pages 1925–1938, 2012.

[38] W. Braun. *Applied RHEED*. Springer, Berlin, 1999.

[39] S. Schreyeck. *Molecular Beam Epitaxy and Characterization of Bi-Based V_2 VI_3 Topological Insulators*. PhD thesis, Julius Maximilians Universität, Würzburg, 2016.

[40] C. W. J. Beenakker and H. van Houten. Quantum Transport in Semiconductor Nanostructures. *Solid State Physics*, 44:1–228, 1991. arXiv: cond-mat/0412664.

[41] H. Ibach and H. Lüth. *Festkörperphysik: Einführung in die Grundlagen*. Springer-Lehrbuch. Springer, Berlin, 7. edition, 2009. OCLC: 297561306.

[42] Ramesh G Mani, Venkatesh Narayanamurti, William B Johnson, and Vladimir Umansky. Zero-resistance states induced by electromagnetic-wave excitation in GaAs/AlGaAs heterostructures. *Nature*, 420:5, 2002.

[43] H.B. Nielsen and M. Ninomiya. The Adler-Bell-Jackiw anomaly and Weyl fermions in a crystal. *Physics Letters B*, 130(6):389–396, November 1983.

[44] E. V. Gorbar, V. A. Miransky, and I. A. Shovkovy. Engineering Weyl nodes in Dirac semimetals by a magnetic field. *Physical Review B*, 88(16), October 2013. arXiv: 1307.6230.

[45] Junhao Chu and Arden Sher. *Physics and properties of narrow gap semiconductors*. Microdevices. Springer, New York, 2008. OCLC: ocn173718715.

[46] M Regnet. *Hochauflösende Röntgenbeugung zur Charakterisierung gestörter Heterostrukturen auf der Basis von II-VI-Halbleitermaterialen.* Dissertation, Julius Maximilians Universität, Würzburg, 1993.

[47] Stanislav Chadov, Xiaoliang Qi, Jürgen Kübler, Gerhard H. Fecher, Claudia Felser, and Shou Cheng Zhang. Tunable multifunctional topological insulators in ternary Heusler compounds. *Nature Materials*, 9(7):541–545, July 2010.

[48] C. Brüne. *HgTe based topological insulators.* PhD thesis, Julius Maximilians Universität, Würzburg, 2014.

[49] Liang Fu and C. L. Kane. Topological insulators with inversion symmetry. *Physical Review B*, 76(4), July 2007.

[50] C. Brüne, C. X. Liu, E. G. Novik, E. M. Hankiewicz, H. Buhmann, Y. L. Chen, X. L. Qi, Z. X. Shen, S. C. Zhang, and L. W. Molenkamp. Quantum Hall Effect from the Topological Surface States of Strained Bulk HgTe. *Physical Review Letters*, 106(12), March 2011.

[51] L. Liu and W. Leung. Transport property of zero-gap semiconductors under tensile stress. *Physical Review B*, 12(6):2336–2345, September 1975.

[52] A. V. Germanenko and G. M. Minkov. Narrow-Gap and Gapless Semiconductors under Uniaxial Stress. Energy Spectrum and Galvanomagnetic Phenomena. *physica status solidi (b)*, 184(1):9–67, July 1994.

[53] A. B. Fowler, F. F. Fang, W. E. Howard, and P. J. Stiles. Magneto-Oscillatory Conductance in Silicon Surfaces. *Physical Review Letters*, 16(20):901–903, May 1966.

[54] Philipp Leubner. *Strain-engineering of the Topological Insulator HgTe.* PhD thesis, Julius Maximilians Universität, Würzburg, 2016.

[55] A. Guillen-Cervantes, Z. Rivera-Alvarez, M. Lopez-Lopez, E. Lopez-Luna, and I. Hernandez-Calderon. GaAs surface oxide desorption by annealing in ultra high vacuum. *Thin Solid Films*, 373(1-2):159–163, September 2000.

[56] G. Horsburgh, K. A. Prior, W. Meredith, I. Galbraith, B. C. Cavenett, C. R. Whitehouse, G. Lacey, A. G. Cullis, P. J. Parbrook, P. Möck, and K. Mizuno. Topography measurements of the critical thickness of ZnSe grown on GaAs. *Applied Physics Letters*, 72(24):3148–3150, June 1998.

[57] B. Buda, C. Wang, W. Wrede, O. Leifeld, D. J. As, D. Schikora, and K. Lischka. The influence of the early stage of ZnSe growth on GaAs(001) on the defect-related luminescence. *Semiconductor Science and Technology*, 13(8):921–926, August 1998.

[58] Y. Seki and O. Oda. Preparation of ZnSe/ZnTe heterostructures by the solid-state substitution method. *Journal of Crystal Growth*, 179(1-2):324–327, August 1997.

[59] H. Maaß, S. Schreyeck, S. Schatz, S. Fiedler, C. Seibel, P. Lutz, G. Karczewski, H. Bentmann, C. Gould, K. Brunner, L. W. Molenkamp, and F. Reinert. Electronic structure and morphology of epitaxial Bi_2Te_2Se topological insulator films. *Journal of Applied Physics*, 116(19):193708, November 2014.

[60] E. Tournié, C. Morhain, G. Neu, M. Laügt, C. Ongaretto, J.-P. Faurie, R. Triboulet, and J. O. Ndap. Structural and optical characterization of ZnSe single crystals grown by solid-phase recrystallization. *Journal of Applied Physics*, 80(5):2983–2989, September 1996.

[61] Hao Ye, Lu Li, Robert T. Hinkey, Rui Q. Yang, Tetsuya D. Mishima, Joel C. Keay, Michael B. Santos, and Matthew B. Johnson. MBE growth optimization of InAs (001) homoepitaxy. *Journal of Vacuum Science & Technology B, Nanotechnology and Microelectronics: Materials, Processing, Measurement, and Phenomena*, 31(3):03C135, May 2013.

[62] G. Tkachov, C. Thienel, V. Pinneker, B. Büttner, C. Brüne, H. Buhmann, L. W. Molenkamp, and E. M. Hankiewicz. Backscattering of Dirac Fermions in HgTe Quantum Wells with a Finite Gap. *Physical Review Letters*, 106(7), February 2011.

[63] Kalle Bendias. *Quantum Spin Hall Effect - A new generation of microstructures*. PhD thesis, Julius Maximilians Universität Würzburg, Würzburg, 2017.

[64] Y. Rajakarunanayake, R. H. Miles, G. Y. Wu, and T. C. McGill. Band structure of ZnSe-ZnTe superlattices. *Physical Review B*, 37(17):10212–10215, June 1988.

[65] I. Eisele and G. Dorda. Negative Magnetoresistance in n -Channel (100) Silicon Inversion Layers. *Physical Review Letters*, 32(24):1360–1363, June 1974.

[66] A. Stupakov, O. Pacherova, T. Kocourek, M. Jelinek, A. Dejneka, and M. Tyunina. Negative magnetoresistance in epitaxial films of neodymium nickelate. *Physical Review B*, 99(8), February 2019.

[67] R D dos Reis, M O Ajeesh, N Kumar, F Arnold, C Shekhar, M Naumann, M Schmidt, M Nicklas, and E Hassinger. On the search for the chiral anomaly in Weyl semimetals: the negative longitudinal magnetoresistance. *New Journal of Physics*, 18(8):085006, August 2016.

[68] G. M. Minkov, A. V. Germanenko, O. E. Rut, A. A. Sherstobitov, S. A. Dvoretski, and N. N. Mikhailov. Weak antilocalization in HgTe quantum wells with inverted energy spectra. *Physical Review B*, 85(23), June 2012.

[69] P. Goswami, J. H. Pixley, and S. Das Sarma. Axial anomaly and longitudinal magnetoresistance of a generic three-dimensional metal. *Physical Review B*, 92(7), August 2015.

[70] Wen Yang, Kai Chang, and Shou-Cheng Zhang. Intrinsic Spin Hall Effect Induced by Quantum Phase Transition in HgCdTe Quantum Wells. *Physical Review Letters*, 100(5), February 2008.

Publications

1. A. Inhofer, S. Tchoumakov, B. A. Assaf, G. Fève, J. M. Berroir, V. Jouffrey, D. Carpinter, M. O. Goerbig, B. Placais, K. Bendias, D. M. Mahler, E. Bocquillon, R. Schlereth, C. Brüne H. Buhmann and L. W. Molenkamp. Observation of Volkov-Pankratov states in topological HgTe heterojunctions using high-frequency compressibility. *Physical Review B* **96**, 195104 (2017).

2. H. Ren, F. Pientka, S. Hart, A. T. Pierce, M. Kosowsky, L. Lunczer, R. Schlereth, B. Scharf, E. M. Hankiewicz, L. W. Molenkamp, B. I. Halperin and A. Yacoby. Topological superconductivity in a phase-controlled Josephson junction. *Nature* **569**, 93-98 (2019).

3. M. C. Dartiailh, S. Hartinger, A. Gourmelon, K. Bendias, H. Bartolomei, H. Kamata, J. M. Berroir, G. Fève, B. Placais, L. Lunczer, R. Schlereth, H. Buhmann, L. W. Molenkamp and E. Bocquillon. *arXiv*:1903.12391v3, 8 Jul 2019.

4. A. Charnukha, A. Sternbach, H. T. Stinson, R. Schlereth, C. Brüne, L. W. Molenkamp and D. N. Basov. Ultrafast nonlocal collective dynamics of Kane plasmon-polaritons in a narrow-gap semiconductor. *Sci. Adv.* 2019; **5**.

5. R. Schlereth, L. Fürst, W. Beugeling, M. Greiter, R. Thomale, T. Khouri, S. Wiedmann, C. Brüne, H. Buhmann and L. W. Molenkamp. $Hg_{1-x}Cd_xTe$: A minimal Dirac semimetal. Manuscript in preparation.

6. R. Schlereth, J. Hajer, L. Fürst, S. Schreyeck, H. Buhmann, and L.W. Molenkamp. Band edge thermometry for the MBE growth of narrow gap (Hg,Cd)Te-based materials. Manuscript in preparation.

Danksagung

An dieser Stelle möchte ich mich bei allen bedanken, die mich während meiner Promotion unterstützt und maßgeblich zum Erfolg dieser Arbeit beigetragen haben.

Allen voran danke ich Prof. Laurens W. Molenkamp für die Möglichkeit diese Dissertation am Lehrstuhl Experimentelle Physik III durchzuführen.

Ich danke auch ganz besonders Prof. Hartmut Buhmann für die ausgezeichnete Betreuung und sein unermüdliches Interesse an meiner Arbeit.

Weiterer Dank gilt den technischen Angestellten Martin Zipf, Petra Wolf-Müller, Volkmar Hock und Carmen Bundschuh, die den reibungsfreien Ablauf dieser Arbeit ermöglicht haben.

Außerdem möchte ich Dr. Thomas Khouri und Dr. Steffen Wiedmann für die Betreuung der Messungen in Nijmegen danken.

Zudem danke ich meinen langjährigen Kollegen für die großartige Atmosphäre und die zahlreichen wissenschaftlichen Diskussionen, insbesondere Lena Fürst, Jan Hajer, David Mahler, Martin Baußenwein, Lukas Lunczer, Dr. Steffen Schreyeck, Dr. Christoph Brüne, Dr. Wouter Beugeling, Dr. Maximilian Kessel, Andreas Budewitz und Angelika Berger.

Ich möchte auch meiner Familie und insbesondere meiner Frau Katharina für die Unterstützung während meiner Promotion ganz herzlich danken.